

Winter 2017

# An improved imaging method for extended targets

Sui Zhang  
*Louisiana Tech University*

Follow this and additional works at: <https://digitalcommons.latech.edu/dissertations>



Part of the [Other Mathematics Commons](#)

---

## Recommended Citation

Zhang, Sui, "" (2017). *Dissertation*. 66.  
<https://digitalcommons.latech.edu/dissertations/66>

This Dissertation is brought to you for free and open access by the Graduate School at Louisiana Tech Digital Commons. It has been accepted for inclusion in Doctoral Dissertations by an authorized administrator of Louisiana Tech Digital Commons. For more information, please contact [digitalcommons@latech.edu](mailto:digitalcommons@latech.edu).

**AN IMPROVED IMAGING METHOD  
FOR EXTENDED TARGETS**

by

Sui Zhang, B.S.

A Dissertation Presented in Partial Fulfillment  
of the Requirements of the Degree  
Doctor of Philosophy

COLLEGE OF ENGINEERING AND SCIENCE  
LOUISIANA TECH UNIVERSITY

February 2017

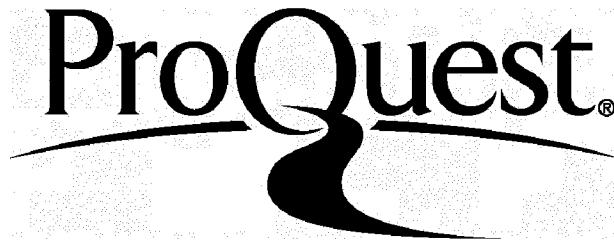
ProQuest Number: 10644151

All rights reserved

INFORMATION TO ALL USERS

The quality of this reproduction is dependent upon the quality of the copy submitted.

In the unlikely event that the author did not send a complete manuscript and there are missing pages, these will be noted. Also, if material had to be removed, a note will indicate the deletion.



ProQuest 10644151

Published by ProQuest LLC(2017). Copyright of the Dissertation is held by the Author.

All rights reserved.

This work is protected against unauthorized copying under Title 17, United States Code.  
Microform Edition © ProQuest LLC.

ProQuest LLC  
789 East Eisenhower Parkway  
P.O. Box 1346  
Ann Arbor, MI 48106-1346

LOUISIANA TECH UNIVERSITY

THE GRADUATE SCHOOL

JANUARY 6, 2017

Date

We hereby recommend that the thesis prepared under our supervision by

Sui Zhang, B.S.

entitled An Improved Imaging Method for Extended Targets

be accepted in partial fulfillment of the requirements for the Degree of

Doctor of Philosophy in Computational Analysis and Modeling

Hon Songjin

Supervisor of Thesis Research

Weighat Dai

Head of Department

Computational Analysis and Modeling

Department

Recommendation concurred in:

W. A. Rice

Junbo Kanno

Weighat Dai

Songjin

Advisory Committee

Approved:

Songjin

Director of Graduate Studies

Misham Hegde

Dean of the College

Approved:

Sheryl S. Shoumda

Dean of the Graduate School

## ABSTRACT

The dissertation presents an improved method for the inverse scattering problem to obtain better numerical results. There are two main methods for solving the inverse problem: the direct imaging method and the iterative method. For the direct imaging method, we introduce the MUSIC (Multiple Signal Classification) algorithm, the multi-tone method and the linear sampling method with different boundary conditions in different cases, which are the smooth case, the one corner case, and the multiple corners case. The dissertation introduces the relations between the far field data and the near field data.

When we use direct imaging methods for solving inverse scattering problems, we observe artificial lines which make it hard to determine the shape of targets. We try to eliminate those lines in different frequencies, but the artificial lines are still in the results and we are forced to get the shape of the targets. Hence, we try to apply multiple frequency data to obtain better results.

There are several reasons to cause the artificial lines. For example, the creation of the response matrix, the error of solving the forward problem and the error of the computation. We propose a signal space test to study the cause of the artificial lines and to use multiple frequency data to reduce the effect from them.

Finally, we use the active contour method to further improve the imaging results. This dissertation introduces the active contour method and the level-set algorithm. We

use the results of the multiple frequencies to obtain the level-set data by utilizing the active contour method and the level-set algorithm. By using the level-set data, we reconstruct the shape of the targets without artificial lines. In order to demonstrate the robustness of the MUSIC algorithm, we add noise to the response matrix.

## APPROVAL FOR SCHOLARLY DISSEMINATION

The author grants to the Prescott Memorial Library of Louisiana Tech University the right to reproduce, by appropriate methods, upon request, any or all portions of this Dissertation. It is understood that "proper request" consists of the agreement, on the part of the requesting party, that said reproduction is for his personal use and that subsequent reproduction will not occur without written approval of the author of this Dissertation. Further, any portions of the Dissertation used in books, papers, and other works must be appropriately referenced to this Dissertation.

Finally, the author of this Dissertation reserves the right to publish freely, in the literature, at any time, any or all portions of this Dissertation.

Author Sun Zhang

Date 2/3/2017

## **DEDICATION**

This is dedicated to my beloved parents Ti Zhang and Liping Zhu, who love me, believe in me, inspire me, and have supported me for years. I could never have walked this far without their encouragement.

## TABLE OF CONTENTS

ABSTRACT.....	iii
DEDICATION.....	vi
LIST OF TABLES.....	ix
LIST OF FIGURES.....	x
NOMENCLATURE.....	xiii
ACKNOWLEDGMENTS.....	xvi
CHAPTER 1 INTRODUCTION.....	1
1.1 Introduction of the Work.....	1
1.2 Research Objectives.....	5
1.3 Organization and Review of the Dissertation.....	6
CHAPTER 2 FORWARD PROBLEM.....	8
2.1 Forward Scattering Problem in the Dirichlet Boundary Condition.....	8
2.2 Forward Scattering Problem in the Neumann Boundary Condition.....	16
2.3 Numerical Experiments.....	22
2.4 The Near Field Data and the Relation to the Far Field Data.....	24
2.5 Summary for Forward Problem.....	28
CHAPTER 3 DIRECT METHOD FOR INVERSE PROBLEM.....	29
3.1 The MUSIC (Multiple Signal Classification) Algorithm.....	29
3.2 The Linear Sampling Method.....	33
3.3 Examples for the MUSIC Algorithm.....	38
3.4 Example for the Multi-tone Method Using Multiple Frequency Data.....	41

3.5	Summary for Inverse Problem .....	44
CHAPTER 4 THE SIGNAL SPACE METHOD .....		45
4.1	The Signal Space Test.....	45
4.2	Numerical Results.....	48
4.3	Summary for the Signal Space Method .....	50
CHAPTER 5 THE IMPROVED METHOD .....		51
5.1	Active Contour Method .....	51
5.2	Level-set Algorithm .....	56
5.3	Numerical Results.....	57
5.4	Dealing with the Noise .....	73
5.5	Numerical Analysis.....	77
5.6	Summary for the Active Contour Method .....	79
CHAPTER 6 CONCLUSIONS AND FUTURE WORK.....		80
6.1	Conclusions.....	80
6.2	Future Work.....	81
APPENDIX.....		85
BIBLIOGRAPHY.....		97

## LIST OF TABLES

<b>Table 2-1:</b> Numerical results for Nystrom method. ....	23
<b>Table 5-1:</b> Numerical analysis for the cases without noise.....	78
<b>Table 5-2:</b> Numerical analysis for the cases with 100% noise. ....	78

## LIST OF FIGURES

<b>Figure 1-1:</b> Applications of direct and inverse problems. ....	4
<b>Figure 1-2:</b> Flow chart for proposed method. ....	7
<b>Figure 2-1:</b> The original shape of the flower. ....	22
<b>Figure 2-2:</b> Kite shaped in four conditions with the Dirichlet boundary condition. ....	27
<b>Figure 2-3:</b> Singular values of four conditions. ....	28
<b>Figure 3-1:</b> Generate the response matrix. ....	29
<b>Figure 3-2:</b> Obtain the response matrix from lab. ....	30
<b>Figure 3-3:</b> MUSIC: kite shaped in four different frequencies. ....	39
<b>Figure 3-4:</b> MUSIC: flower shaped in four different frequencies. ....	40
<b>Figure 3-5:</b> MUSIC: teardrop shaped in four different frequencies. ....	40
<b>Figure 3-6:</b> MUSIC: two objects shaped in two different frequencies. ....	41
<b>Figure 3-7:</b> MUSIC and Multi-tone: kite shape of multiple frequencies. ....	42
<b>Figure 3-8:</b> MUSIC and Multi-tone: teardrop shape of multiple frequencies. ....	43
<b>Figure 3-9:</b> MUSIC and Multi-tone: flower shape of multiple frequencies. ....	43
<b>Figure 3-10:</b> MUSIC and Multi-tone: two-object-shape of multiple frequencies. ....	44
<b>Figure 4-1:</b> Three shapes of the targets by their parametric equations. ....	47
<b>Figure 4-2:</b> Two-object-shape of the targets by their parametric equations. ....	47
<b>Figure 4-3:</b> Signal space test: kite shape in four different frequencies. ....	48
<b>Figure 4-4:</b> Signal space test: teardrop shape in four different frequencies. ....	49
<b>Figure 4-5:</b> Signal space test: flower shape in four different frequencies. ....	49
<b>Figure 4-6:</b> Signal space test: two-object-shape in two different frequencies. ....	50

<b>Figure 5-1:</b> Contours of the kite shape.....	59
<b>Figure 5-2:</b> Contours of the teardrop shape. ....	59
<b>Figure 5-3:</b> Contours of the flower shape. ....	60
<b>Figure 5-4:</b> Contours of two-object-shape: the figure on top is the contours of the left object; figure on the bottom is the contours of the right object. ....	60
<b>Figure 5-5:</b> Contours of the plane shape. ....	61
<b>Figure 5-6:</b> The level set lines of the kite shape. ....	62
<b>Figure 5-7:</b> The level set lines of the teardrop shape. ....	62
<b>Figure 5-8:</b> The level set lines of the flower shape. ....	63
<b>Figure 5-9:</b> The level set lines of the two objects shape. ....	63
<b>Figure 5-10:</b> The level set lines of the plane shape. ....	64
<b>Figure 5-11:</b> Obtain points for star-like shape. ....	65
<b>Figure 5-12:</b> Obtain points for non-star-like shape. ....	66
<b>Figure 5-13:</b> Compare the active contour method to the original shape of the kite. ....	67
<b>Figure 5-14:</b> Compare the active contour method to the original shape of the teardrop. ....	67
<b>Figure 5-15:</b> Compare the active contour method to the original shape of the flower. ....	68
<b>Figure 5-16:</b> Compare the active contour method to the original shape of the two objects. ....	68
<b>Figure 5-17:</b> Compare the active contour method to the original shape of the plane. ....	69
<b>Figure 5-18:</b> Compare the averaged active contour method to the original shape of the kite. ....	70
<b>Figure 5-19:</b> Compare the averaged active contour method to the original shape of the teardrop. ....	70
<b>Figure 5-20:</b> Compare the averaged active contour method to the original shape of the flower. ....	71
<b>Figure 5-21:</b> Compare the averaged active contour method to the original shape of the plane. ....	71

<b>Figure 5-22:</b> Compare the averaged active contour method to the original shape of the two objects. ....	72
<b>Figure 5-23:</b> Compare the averaged active contour method to the original shape of the kite with 100% noise. ....	74
<b>Figure 5-24:</b> Compare the averaged active contour method to the original shape of the teardrop with 100% noise. ....	75
<b>Figure 5-25:</b> Compare the averaged active contour method to the original shape of the flower with 100% noise. ....	75
<b>Figure 5-26:</b> Compare the averaged active contour method to the original shape of the plane with 100% noise. ....	76
<b>Figure 5-27:</b> Compare the averaged active contour method to the original shape of the two-object with 100% noise. ....	76
<b>Figure 5-28:</b> Method for doing numerical analysis for non-star-like shape. ....	79
<b>Figure 6-1:</b> MUSIC: kite-shape in four different frequencies with the Neumann boundary condition. ....	82
<b>Figure 6-2:</b> MUSIC: teardrop-shape in four different frequencies with the Neumann boundary condition. ....	82
<b>Figure 6-3:</b> MUSIC: flower-shape in four different frequencies with the Neumann boundary condition. ....	83
<b>Figure 6-4:</b> MUSIC: two-object-shape in two different frequencies with the Neumann boundary condition. ....	83

## NOMENCLATURE

$u$	The total field
$u^i$	The incident field
$u^s$	The scattered field
$P$	The response matrix
$k$	The wave number
$r$	The distance
$\Omega$	The medium region
$\mathbb{R}$	The real space
$i$	The imaginary unit
$\nu$	The unit outward normal
$\rho$	The density
$\omega$	The wave frequency
$\Phi$	The fundamental solution of Helmholtz equation
$\varphi$	The density function
$\psi$	The discrete density function
$S$	The single-layer operator
$K$	The double-layer operator
$\eta$	The coupling parameter
$L$	The integral kernel $L$

$M$	The integral kernel $M$
$G(\cdot, \cdot)$	The Green's function
$I$	The identity operator
$\vec{g}_0$	The illumination vector
$V_s$	The signal space
$\delta(\cdot)$	The delta function
$\phi$	The level set function
$E$	The electric field
$H$	The magnetic field
$\Phi_0$	The fundamental solution to Laplace equation
$\Delta$	The Laplace operator
$\nabla$	The gradient operator
$v$	The velocity
$p$	The pressure
$d$	The incident direction
$n$	The unit normal
$\gamma$	Euler-Msacheroni constant
$\sigma$	The singular value
$E_\infty$	The electric far-pattern
$N$	The number of transducers
$C$	The curve
$\delta_0$	Dirac measure
$c_1, c_2$	Constants of active contour method

$\phi_0$  The initial contour

$P_{ij}$  The element of the response matrix

$d_i$  The *ith* distance of two points in one direction

$D$  The diameter of two points on boundary

## ACKNOWLEDGMENTS

On the completion of my dissertation, I would like to express my sincere thanks to my teachers, family and colleagues.

First of all, I wish to thank my advisor, Dr. Songming Hou, for leading me into this fantastic world of Applied Mathematics, continually guiding me and giving me knowledge, enthusiasm, and confidence on this road. Without his encouragement and support, I would not have fulfilled my Ph.D. study.

Special thanks to my committee: Dr. Weizhong Dai, Dr. Sumeet Dua, Dr. Katie A. Evans, and Dr. Jinko Kanno, as well as all others in COES (College of Engineering and Science) of Louisiana Tech University for their precious advice and kind help.

I am grateful to my beloved family for their sacrifice and their love. They have supported me throughout these years.

# CHAPTER 1

## INTRODUCTION

### 1.1 Introduction of the Work

Scattering theory has played more of an important role in 20th Century mathematical physics. By sending probing waves and collecting the scattered waves, we can identify the location and shape of the targets. For direct scattering problems, if we view the total field as the sum of an incident field  $u^i$  and a scattered field  $u^s$ , then the problem is to determine  $u^s$  from the  $u^i$  and the differential equation [1] [2] [3] [4] [5] [6] [7] [8], which is the Helmholtz Equation, with proper boundary conditions.

The Helmholtz Equation is obtained from the wave equation [9]. The wave motion is given by Euler's equation (see Eq. 1-1)

$$\frac{\partial v}{\partial t} + (v \cdot \nabla)v + \frac{1}{\rho} \nabla p = 0, \quad \text{Eq. 1-1}$$

with the equation of continuity (see Eq. 1-2)

$$\frac{\partial \rho}{\partial t} + \nabla \cdot (\rho v) = 0. \quad \text{Eq. 1-2}$$

We then have the state equation (see Eq. 1-3)

$$p = f(\rho, s), \quad \text{Eq. 1-3}$$

and the hypothesis of adiabatic (see Eq. 1-4)

$$\frac{\partial S}{\partial t} + v \cdot \nabla S = 0, \quad \text{Eq. 1-4}$$

where  $v = v(x, t)$  is the velocity field,  $p = p(x, t)$  is the pressure,  $\rho = \rho(x, t)$  is the density,  $S = S(x, t)$  is the entropy, and  $f$  is a function related to the property of the fluid.

We now consider the case, in which we assume that  $v_0 = 0$ ,  $p_0 = \text{constant}$ ,  $\rho_0 = \text{constant}$ , and  $S_0 = \text{constant}$ . Then we rewrite Eq. 1-1, Eq. 1-2 and Eq. 1-3 and obtain Eq. 1-5, Eq. 1-6 and Eq. 1-7

$$\frac{\partial v}{\partial t} + \frac{1}{\rho_0} \nabla p = 0, \quad \text{Eq. 1-5}$$

$$\frac{\partial \rho}{\partial t} + \rho_0 \nabla \cdot v = 0, \quad \text{Eq. 1-6}$$

$$\frac{\partial p}{\partial t} = \frac{\partial f}{\partial \rho}(\rho_0, S_0) \frac{\partial \rho}{\partial t}. \quad \text{Eq. 1-7}$$

By combining Eq. 1-5, Eq. 1-6 and Eq. 1-7, we have the wave equation (see Eq. 1-8 and Eq. 1-9)

$$\frac{1}{c^2} \frac{\partial^2 f}{\partial t^2} = \Delta p, \quad \text{Eq. 1-8}$$

where  $c$  is the speed of sound

$$c^2 = \frac{\partial f}{\partial \rho}(\rho_0, S_0), \quad \text{Eq. 1-9}$$

and also by combining Eq. 1-5, Eq. 1-6 and Eq. 1-7, we obtain the potential of velocity

$U = U(x, t)$  (see Eq. 1-10 and Eq. 1-11)

$$v = \frac{1}{\rho_0} \nabla u, \quad \text{Eq. 1-10}$$

$$p = -\frac{\partial U}{\partial t}, \quad \text{Eq. 1-11}$$

and Eq. 1-10, Eq. 1-11 satisfy the wave equation (see Eq. 1-12)

$$\frac{1}{c^2} \frac{\partial^2 U}{\partial t^2} = \Delta U. \quad \text{Eq. 1-12}$$

We have the form of the time-harmonic acoustic wave (see Eq. 1-13)

$$U(x, t) = \text{Re}\{u(x)e^{-i\omega t}\}, \quad \text{Eq. 1-13}$$

with frequency  $\omega > 0$ , and  $u$  satisfies the Helmholtz Equation (see Eq. 1-14)

$$\Delta u + k^2 u = 0, \quad \text{Eq. 1-14}$$

where  $k$  is the wave number given by  $k = \omega/c$ .

For the inverse scattering problem, there are two main ways to solve the problem: iterative methods and direct methods. The iterative methods [10] [11] [12] [13] [14] [15] [16] [17] are accurate but more expensive, and the direct methods [18] [19] [20] [21] [22] are efficient but less accurate. However, we are not focusing on the iterative methods, because for each iteration, it costs too much time to solve an adjoint forward problem.

Direct imaging methods are more popular nowadays. They are not based on nonlinear optimization and do not require forward iterations, for example, the Multiple Signal Classification (MUSIC) algorithm [23] [24] [25] [26] [27]. We first set up the response matrix; then we could obtain the singular values and singular vectors by taking the Singular Value Decomposition (SVD) of the response matrix. By using the imaging function involving Green's function, the inverse scattering problem can be solved.

There are many important applications based on direct and inverse scattering problems such as in radar, sonar, medical imaging, and nondestructive testing, showing in **Figure 1-1**.



**Figure 1-1:** Applications of direct and inverse problems.

The linear sampling method [28] [29] is also a direct imaging algorithm for the inverse scattering problem. It characterizes the domain of an unknown scatterer by the behavior of the solution to an integral equation of the first kind. The main idea is that the norm of a certain solution blows up on the target boundary. Kirsch [30] modified the linear sampling method by using a factorization for the scattering operator. It appears that the linear sampling method is an extension of the MUSIC algorithm [31] [32], so it can also produce the location and shape of the target by using all the eigenvalues and eigenfunctions.

We refer to [33] for the uniqueness in inverse acoustic and electromagnetic obstacle scattering problems.

When we use the MUSIC algorithm or other direct imaging methods to obtain the shape of the target, we observe many artificial lines. We wonder how the artificial lines form, and how we can avoid the artificial lines. Hence, we propose a signal space test to study the cause of the artificial lines. In order to decrease the effect of these lines, we combine multiple frequency results. We use both the multiple frequency MUSIC algorithm and the multi-tone method [20] [21].

Finally, we propose a novel method by using the active contour method [34] to improve the imaging results. Even though this method exists in the literature for decades, it has not been applied to improve the inverse problem solver. The idea is that the average location of the two sharp gradient lines is a reasonable estimate for the target shape. Numerical examples for smooth target, targets with one corner and multiple corners are presented with excellent results.

## 1.2 Research Objectives

The objective of this dissertation is to improve the imaging method, to obtain a better result of the unknown targets, and relations between far field data and the near field data.

In detail, we list the research objectives of this dissertation in detail:

1. Using forward and inverse problem to reconstruct shape of the unknown targets.
2. Using the signal space method to test what caused the artificial lines.
3. Using the multiple frequency data to try to decrease the artificial lines.
4. Using the active contour method to find the exact shape of the unknown targets.

### 1.3 Organization and Review of the Dissertation

In Chapter 1, we will briefly introduce the work, knowledge of the background, research objectives and the organization of the dissertation.

In Chapter 2, we will introduce the basic background of the forward scattering problem in both Dirichlet and Neumann boundary condition [35]. In particular, we will go through the work by Colton and Kress [9]. The Nystrom method is used to solve the forward scattering problem, and the numerical results will be shown. We also state the relations between far field data and the near field data [9] [19]. My original work is to show the relations of the near field data and the far field data with different distance for source and receiver. Also, we present the numerical results of the near field data and the far field data in different cases, and verify the relations of these cases.

In Chapter 3, we will introduce two main direct methods by [25] [29], the MUSIC method and the linear sampling method, for the inverse scattering problem. The multi-tone method [20] is introduced to get better experiment results. My original work is to present all the numerical results of the MUSIC method and the multi-tone.

In Chapter 4, we will express the signal space method, including the steps of this new method. This is my original work. We want to use this method to prove the cause of the artificial lines. Also, all the numerical results will be shown in this chapter.

In Chapter 5, we will develop a new method to improve the imaging method. We will introduce the active contour method and the level-set algorithm [34] [36], with which we can obtain better experiment results. My original work is to do the averaging for the shape gradient contour and to involve the idea of using ACWE to improve the direct

imaging method for inverse problem. The results are presented excellently compared to the old imaging method in different cases.

In Chapter 6, we will provide a conclusion and future work for this dissertation.

In the Appendix, we will list my codes for both forward and inverse scattering problems.

The flow chart for our proposed method is shown in **Figure 1-2**.

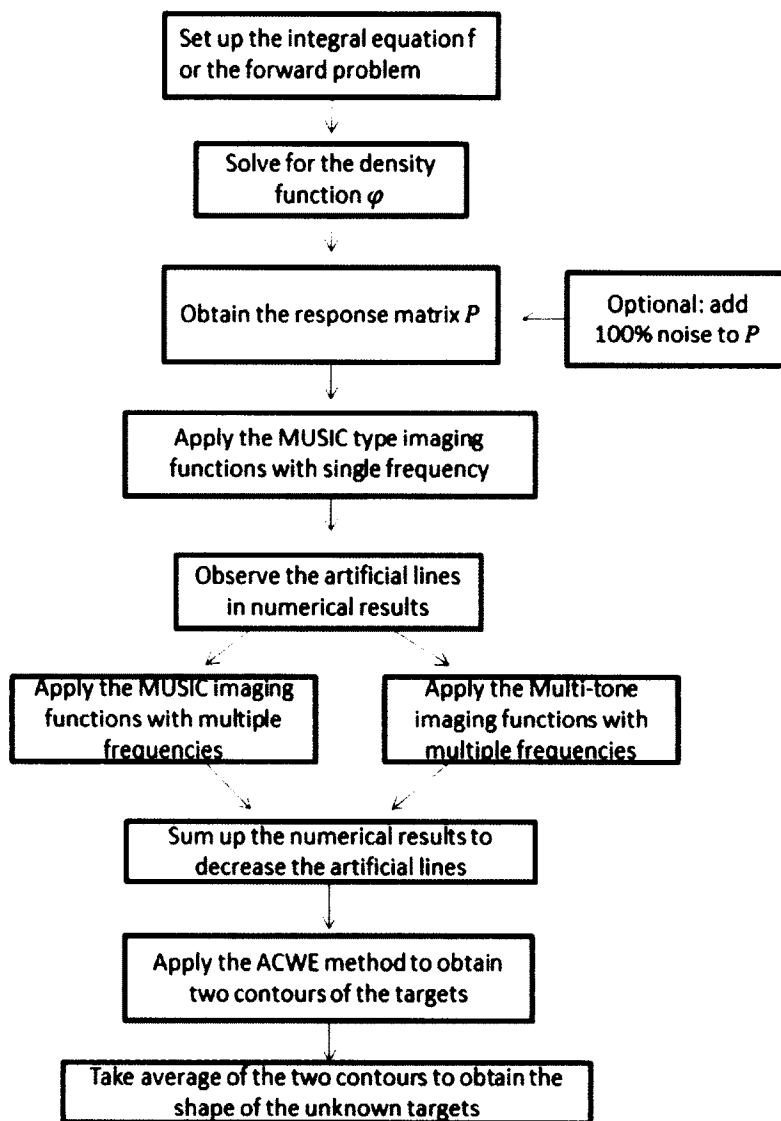


**Figure 1-2:** Flow chart for proposed method.

## CHAPTER 2

### FORWARD PROBLEM

In this chapter, we will discuss the forward scattering problem in two main boundary conditions, which are the Dirichlet boundary condition and the Neumann boundary condition. Also, the Nystrom discretization [9] will be introduced for 2D scattering problem.

#### 2.1 Forward Scattering Problem in the Dirichlet Boundary Condition

In this section, we introduce the Helmholtz Equation [9] with the Dirichlet boundary condition (see Eq. 2-1)

$$\begin{aligned}\Delta u + k^2 u &= 0, \quad \text{in } \mathbb{R}^2 \setminus \bar{D}, \\ u &= 0, \quad \text{on } \partial D,\end{aligned}\tag{Eq. 2-1}$$

where  $k$  is the wavenumber and  $d \in \mathbb{S}^1$  is the incident direction.

The incident field satisfies the homogeneous equation (see Eq. 2-2)

$$\Delta u^i + k^2 u^i = 0,\tag{Eq. 2-2}$$

where the time-harmonic wave is shown in Eq. 2-3

$$u^i = e^{ikx \cdot d}.\tag{Eq. 2-3}$$

The total field consists of the incident field  $u^i$  and the scattered field  $u^s$  (see Eq. 2-4)

$$u = u^i + u^s.\tag{Eq. 2-4}$$

From Eq. 2-1, Eq. 2-3 and Eq. 2-4, the scattered field satisfies Eq. 2-5 and Eq. 2-6

$$\Delta u^s + k^2 u^s = 0, \quad \text{in } \mathbb{R}^2 \setminus \bar{D}, \quad \text{Eq. 2-5}$$

$$u^s = -u^i, \quad \text{on } \partial D. \quad \text{Eq. 2-6}$$

For the scattered wave  $u^s$ , we have the radiation condition (see Eq. 2-7)

$$\lim_{r \rightarrow \infty} \sqrt{r} \left( \frac{\partial u^s}{\partial r} - i k u^s \right) = 0, \quad r = |\mathbf{x}|. \quad \text{Eq. 2-7}$$

**Equation 2-7** is called the Sommerfeld radiation condition, and the limit is assumed to hold uniformly in all directions  $\mathbf{x}/|\mathbf{x}|$ . **Equation 2-7** is imposed for  $u^s$  for the physical meaning and it also guarantees the uniqueness result for the forward scattering problem.

By introducing the fundamental solution which satisfies the Helmholtz Equation, we have **Eq. 2-8**

$$\Phi(x, y) = \frac{i}{4} H_0^1(k|x - y|), \quad x \neq y. \quad \text{Eq. 2-8}$$

We now go through the layer approach for finding a solution to the Dirichlet problem using boundary integral equations [9].

**Definition 2.1.1. Acoustic Single-layer Potential.** Given any integral function  $\varphi$ , define the integral  $u$  such that (see Eq. 2-9)

$$u(x) = \int_{\partial D} \varphi(y) \Phi(x, y) ds(y), \quad \text{Eq. 2-9}$$

where  $\Phi(x, y)$  is the fundamental solution in Eq. 2-8;  $u(x)$  is called the acoustic single-layer potential with density  $\varphi$ .

**Definition 2.1.2. Acoustic Double-layer Potential.** Given any integral function  $\varphi$ , define the integral  $v$  such that (see Eq. 2-10)

$$v(x) = \int_{\partial D} \varphi(y) \frac{\partial \Phi(x, y)}{\partial \nu(y)} ds(y), \quad \text{Eq. 2-10}$$

where  $\Phi(x, y)$  is the fundamental solution in Eq. 2-8;  $v(x)$  is called the acoustic double-layer potential with density  $\varphi$ .

We know that  $u$  and  $v$  are solutions to the Helmholtz Equation. We could express the combination of single-layer and double-layer potentials as the solution to the Helmholtz Equation.

Here, we explain why we use the combined single- and double-layer potential, rather than double-layer potential (see Eq. 2-11 – Eq. 2-15).

**Definition 2.1.3. Exterior Dirichlet Problem.** Given a continuous function  $f$  on  $\partial D$ , find a radiating solution  $u \in C^2(\mathbb{R}^2 \setminus \bar{D}) \cap C(\mathbb{R}^2 \setminus D)$  to the Helmholtz Equation

$$\Delta u + k^2 u = 0 \text{ in } \mathbb{R}^2 \setminus \bar{D}, \quad \text{Eq. 2-11}$$

which satisfies the boundary condition

$$u = f \text{ on } \partial D. \quad \text{Eq. 2-12}$$

By Definition 2.1.2, we know that  $v(x)$  satisfies Eq. 2-7 and Eq. 2-12. If  $v(x)$  is the solution to the Exterior Dirichlet Problem,  $v(x)$  only needs to satisfy Eq. 2-12.

By the jump relations [9],  $\varphi$  is the solution to the equation in Eq. 2-13

$$\frac{1}{2} \varphi(x) + \int_{\partial D} \frac{\partial \Phi(x, y)}{\partial n(y)} \varphi(y) ds(y) = f(x), \quad x \in \partial D. \quad \text{Eq. 2-13}$$

With using the operator  $K$ , Eq.2-13 can be written as

$$\varphi + K\varphi = 2f, \quad \text{Eq. 2-14}$$

which is

$$(I + K)\varphi = 2f. \quad \text{Eq. 2-15}$$

**Definition 2.1.4. Interior Neumann Problem.** Given a continuous function  $g$  on  $\partial D$ , find a radiating solution  $u \in C^2(D) \cap C(\bar{D})$  to the Helmholtz Equation (see Eq. 2-16)

$$\Delta u + k^2 u = 0 \text{ in } D, \quad \text{Eq. 2-16}$$

which satisfies the boundary condition (see Eq. 2-17)

$$\frac{\partial u}{\partial n} = g, \quad \text{on } \partial D, \quad \text{Eq. 2-17}$$

where (see Eq. 2-18)

$$\frac{\partial u}{\partial n}(x) = \lim_{h \rightarrow +0} n(x) \cdot \nabla u(x - h \cdot n(x)). \quad \text{Eq. 2-18}$$

When  $g = 0$ , if the interior Neumann Problem has nontrivial solution  $u$ , then  $k^2$  is the eigenvalue of  $-\Delta$  on  $D$ ,  $u$  is the eigenvector.

Then we define the linear space, which is (see Eq. 2-19)

$$U = \{u|_{\partial D} \mid u \in C^2(D) \cap C(\bar{D}), \Delta u + k^2 u = 0 \text{ in } D, \quad \frac{\partial u}{\partial n} = 0 \text{ on } \partial D\}, \quad \text{Eq. 2-19}$$

where (see Eq. 2-20)

$$\frac{\partial u}{\partial n}(x) = \lim_{h \rightarrow +0} n(x) \cdot \nabla u(x - h \cdot n(x)). \quad \text{Eq. 2-20}$$

From these two equations, we know that if  $k^2$  is not the eigenvalue on  $D$ , then we have  $U = \emptyset$  [37].

**Theorem 2.1.1.**  $\ker(I + K) = U$ . [37]

According to **Theorem 2.1.1**, when  $k^2$  is the eigenvalue, we have  $U \neq \emptyset$ , which means  $\ker(I + K) \neq \emptyset$ , operator  $I + K$  is not injection.

After we use the combined double- and single-layer potential, we have an equation of the smooth target case as **Eq. 2-21**

$$u(x) = \int_{\partial D} \left\{ \frac{\partial \Phi(x, y)}{\partial \nu(y)} - i\eta \Phi(x, y) \right\} \varphi(y) ds(y), \quad \text{Eq. 2-21}$$

$$x \in \mathbb{R}^2 \setminus \partial D,$$

with a density  $\varphi \in C(\partial D)$  and the parameter  $\eta \neq 0$ . Note that if  $\eta = 0$ , the problem is not uniquely solvable.

Then from the jump relations, we have the integral equation **Eq. 2-22**

$$\varphi + K\varphi - i\eta S\varphi = 2f, \quad \text{Eq. 2-22}$$

the operators  $K, S: C(\partial D) \rightarrow C(\partial D)$  are compact [9].

By **Theorem 2.1.1**, when  $\eta = 0$ , the operator  $I + K - i\eta S$  has no inverse, if  $k^2$  is the singular value of the interior Neumann problem. Hence, **Eq. 2-22** may not have a solution. In order to fix this problem, we apply the combined single- and double-layer potential to solve **Eq. 2-21**, where  $\eta \neq 0$ .

For the Dirichlet problem, we parametrize **Eq. 2-22** and obtain **Eq. 2-23**

$$\psi(t) - \int_0^{2\pi} [L(t, \tau) + i\eta M(t, \tau)] \psi(\tau) d\tau = g(t), \quad \text{Eq. 2-23}$$

$$0 \leq t \leq 2\pi,$$

where  $\psi(t) = \varphi(x(t))$ ,  $g(t) = 2f(x(t))$  and the kernels are given by (see **Eq. 2-24** - **Eq. 2-34**)

$$L(t, \tau) = \frac{ik}{2} \{x'_2(\tau)[x_1(\tau) - x_1(t)] - x'_1(\tau)[x_2(\tau) - x_2(t)]\} \cdot \frac{H_1^{(1)}(kr(t, \tau))}{r(t, \tau)}, \quad \text{Eq. 2-24}$$

$$M(t, \tau) = \frac{i}{2} H_0^{(1)}(kr(t, \tau)) \{[x'_1(\tau)]^2 + [x'_2(\tau)]^2\}^{1/2}. \quad \text{Eq. 2-25}$$

For  $t \neq \tau$ , let

$$r(t, \tau) = \{[x_1(t) - x_1(\tau)]^2 + [x_2(t) - x_2(\tau)]^2\}^{1/2}. \quad \text{Eq. 2-26}$$

By the numerical method introduced in [38], we need to split the kernels into

$$L(t, \tau) = L_1(t, \tau) \ln \left( 4 \sin^2 \frac{t - \tau}{2} \right) + L_2(t, \tau), \quad \text{Eq. 2-27}$$

$$M(t, \tau) = M_1(t, \tau) \ln \left( 4 \sin^2 \frac{t - \tau}{2} \right) + M_2(t, \tau), \quad \text{Eq. 2-28}$$

where

$$L_1(t, \tau) = \frac{k}{2\pi} \{x_2'(\tau)[x_1(t) - x_1(\tau)] \quad \text{Eq. 2-29}$$

$$- x_1'(\tau)[x_2(t) - x_2(\tau)]\} \cdot \frac{J_1(kr(t, \tau))}{r(t, \tau)},$$

$$L_2(t, \tau) = L(t, \tau) - L_1(t, \tau) \ln \left( 4 \sin^2 \frac{t - \tau}{2} \right), \quad \text{Eq. 2-30}$$

$$M_1(t, \tau) = -\frac{1}{2\pi} J_0(kr(t, \tau)) \{[x_1'(\tau)]^2 + [x_2'(\tau)]^2\}^{1/2}, \quad \text{Eq. 2-31}$$

$$M_2(t, \tau) = M(t, \tau) - M_1(t, \tau) \ln \left( 4 \sin^2 \frac{t - \tau}{2} \right). \quad \text{Eq. 2-32}$$

In particular, we have the diagonal terms for  $t = \tau$ , then we obtain

$$M_2(t, t) = \left\{ \frac{i}{2} - \frac{C}{\pi} - \frac{1}{2\pi} \ln \left( \frac{k^2}{4} \{[x_1'(t)]^2 + [x_2'(t)]^2\} \right) \right\} \quad \text{Eq. 2-33}$$

$$\cdot \{[x_1'(t)]^2 + [x_2'(t)]^2\}^{1/2},$$

$$L_2(t, t) = L(t, t) = \frac{1}{2\pi} \frac{x_1'(t)x_2''(t) - x_2'(t)x_1''(t)}{[x_1'(t)]^2 + [x_2'(t)]^2}, \quad \text{Eq. 2-34}$$

where we can write the kernel  $K$  as Eq. 2-35

$$K(t, \tau) = K_1(t, \tau) \ln \left( 4 \sin^2 \frac{t - \tau}{2} \right) + K_2(t, \tau), \quad \text{Eq. 2-35}$$

with analytic functions  $K_1 = L_1 + ikM_1$  and  $K_2 = L_2 + ikM_2$  in [9]. We now introduce the Nystrom method, which uses an approximation of the integrals by quadrature formulas. We need to choose the equidistant set  $t_j = \pi j/n$ , where  $j = 0, \dots, 2n - 1$  because the boundary of the target is a  $2\pi$ -periodic form. Then we have the quadrature rule (see Eq. 2-36 and Eq. 2-37)

$$\int_0^{2\pi} \ln \left( 4 \sin^2 \frac{t-\tau}{2} \right) f(\tau) d\tau \approx \sum_{j=1}^{2n-1} R_j^{(n)}(t) f(t_j), \quad \text{Eq. 2-36}$$

with

$$R_j^{(n)}(t) = -\frac{2\pi}{n} \sum_{m=1}^{n-1} \frac{1}{m} \cos m(t-t_j) - \frac{\pi}{n^2} \cos n(t-t_j), \quad \text{Eq. 2-37}$$

then we have the Trapezoidal rule (see Eq. 2-38)

$$\int_0^{2\pi} f(\tau) d\tau \approx \frac{\pi}{n} \sum_{j=0}^{2n-1} f(t_j), \quad \text{Eq. 2-38}$$

so we can represent the function  $f$  by any integration kernel.

In the Nystrom method, we can combine Eq. 2-35, Eq. 2-36 and Eq. 2-38 and replace them by the finite summation to obtain Eq. 2-39

$$\begin{aligned} \psi^{(n)}(t) - \sum_{j=0}^{2n-1} \left\{ R_j^{(n)}(t) K_1(t, t_j) + \frac{\pi}{n} K_2(t, t_j) \right\} \psi^{(n)}(t_j) \\ = g(t), \end{aligned} \quad \text{Eq. 2-39}$$

where  $0 \leq t \leq 2\pi$ .

Therefore, Eq. 2-39 has the value of the solution (see Eq. 2-40)

$$\psi_i^{(n)} = \psi^{(n)}(t_i), \quad i = 0, \dots, 2n - 1, \quad \text{Eq. 2-40}$$

which satisfies the linear system (see **Eq. 2-41**)

$$\psi_i^{(n)} - \sum_{j=0}^{2n-1} \left\{ R_{|i-j|}^{(n)}(t) K_1(t_i, t_j) + \frac{\pi}{n} K_2(t_i, t_j) \right\} \psi_j^{(n)} = g(t_i), \quad \text{Eq. 2-41}$$

so for  $i, j = 0, \dots, 2n - 1$ , we have **Eq. 2-42**

$$R_j^{(n)} = R_j^{(n)}(0) = -\frac{2\pi}{n} \sum_{m=1}^{n-1} \frac{1}{m} \cos \frac{mj\pi}{n} - \frac{(-1)^j \pi}{n^2}. \quad \text{Eq. 2-42}$$

The computational cost for solving the linear system is  $O(n^3)$ . When we are given a solution  $\psi_i^{(n)}$  for the linear system of **Eq. 2-41**, the function  $\psi^{(n)}$  can be defined as **Eq. 2-43**

$$\begin{aligned} \psi^{(n)}(t) = & \sum_{j=0}^{2n-1} \left\{ R_j^{(n)}(t) K_1(t, t_j) + \frac{\pi}{n} K_2(t, t_j) \right\} \psi^{(n)}(t_j) \\ & + g(t), \quad 0 \leq t \leq 2\pi. \end{aligned} \quad \text{Eq. 2-43}$$

We now briefly introduce the one corner case in the Dirichlet boundary condition.

Here, we meet a new challenge, which is more complicated.

With the fundamental solution, we rewrite **Eq. 2-8** for the case with one corner.

For  $x \in \mathbb{R}^2 \setminus \partial \bar{D}$ , we have **Eq. 2-44**

$$\begin{aligned} u(x) = & \int_{\partial D} \left[ \left\{ \frac{\partial \Phi(x, y)}{\partial \nu(y)} - i\eta \Phi(x, y) \right\} \varphi(y) \right. \\ & \left. - \frac{\partial \Phi_0(x, y)}{\partial \nu(y)} \varphi(x_0) \right] ds(y), \end{aligned} \quad \text{Eq. 2-44}$$

where  $x_0$  is the corner location.

The new challenge in the corner case is that, in addition to the logarithmic singularity shown in **Eq. 2-21**, there is a corner singularity. A change of variable using the graded mesh is proposed in [9].

Again, by using jump relation, we have Eq. 2-45

$$\begin{aligned} \varphi(x) - \varphi(x_0) + 2 \int_{\partial D} \left\{ \frac{\partial \Phi(x, y)}{\partial \nu(y)} - i\eta \Phi(x, y) \right\} \varphi(y) ds(y) \\ - 2 \int_{\partial D} \frac{\partial \Phi_0(x, y)}{\partial \nu(y)} \varphi(x_0) ds(y) = 2f(x), \end{aligned} \quad \text{Eq. 2-45}$$

for  $x \in \partial D$ , at corner  $x_0$ , where  $\Phi_0(x, y) = \frac{1}{2\pi} \ln \frac{1}{|x-y|}$ ,  $x \neq y$ .

The Nystrom method for the one corner case is similar to the smooth case. We will present some details handling the corner in the next section when dealing with the Neumann boundary condition.

## 2.2 Forward Scattering Problem in the Neumann Boundary Condition

In this section, we will introduce the Neumann boundary condition [35] as Eq. 2-46 and Eq. 2-47

$$\Delta u^s + k^2 u^s = 0, \quad \text{in } \mathbb{R}^2 \setminus \bar{D}, \quad \text{Eq. 2-46}$$

$$\frac{\partial u^s}{\partial n} = -\frac{\partial u^i}{\partial n}, \quad \text{on } \partial D, \quad \text{Eq. 2-47}$$

together with Eq. 2-7, which is introduced as the radiation condition.

Like the Dirichlet problem, the Neumann problem also has the single- and double-layer operators. We consider the case that the boundary has one corner [35].

We define the single-layer operator as Eq. 2-48

$$(K'_k \phi)(x) = PV \int_{\Gamma} \frac{\partial G_k(x-y)}{\partial n(x)} \phi(y) ds(y), \quad x \text{ on } \partial D, \quad \text{Eq. 2-48}$$

and the double-layer operator as Eq. 2-49

$$\frac{\partial^2 G_k(x-y)}{\partial n(x) \partial n(y)} = -\frac{\partial^2 G_k(x-y)}{\partial t(x) \partial t(y)} + k^2 G_k(x-y) n(x) \cdot n(y), \quad \text{Eq. 2-49}$$

where  $G_k$  is the Green's function. For  $n = (n_1, n_2)$ , we have  $t = (-n_2, n_1)$ ;  $\frac{\partial}{\partial t}$  is the tangential derivative on  $\partial D$ .

With Eq. 2-46 - Eq. 2-49, the integral equation with one corner parametrically can be expressed [39] [40] (see Eq. 2-50)

$$\begin{aligned}
g(t) = & \left(\frac{1}{2} + \frac{i\eta}{4}\right) \psi(t) + \left(\frac{1}{2} - \frac{i\eta}{4}\right) \psi(0) - \int_0^{2\pi} H(t, \tau) \psi(\tau) d\tau \\
& - \int_0^{2\pi} \left(1 + \frac{i\eta}{2}\right) H_0(t, \tau) (\psi(\tau) - \psi(0)) d\tau \\
& - i\eta \int_0^{2\pi} \frac{M_0(t, \tau)}{|x'(\tau)|} \left( \int_0^{2\pi} (L(\tau, z) + M(\tau, z)) \psi(z) dz \right) d\tau \quad \text{Eq. 2-50} \\
& - i\eta \int_0^{2\pi} H_0(t, \tau) \left( \int_0^{2\pi} (H_0(\tau, z) - H_0(0, z)) (\psi(z) \right. \\
& \quad \left. - \psi(0)) dz \right) d\tau,
\end{aligned}$$

where we define  $g$  as Eq. 2-51

$$g(t) = u^i(\mathbf{x}(t)) + i\eta \int_0^{2\pi} M_0(t, \tau) \frac{\partial u^i}{\partial v}(\mathbf{x}(\tau)) d\tau. \quad \text{Eq. 2-51}$$

From Eq. 2-51, a combination of a graded-mesh quadrature will be applied to the integrals. Therefore, we need to do the change-of-variables. We have  $t = \omega(s)$ , where (see Eq. 2-52 and Eq. 2-53)

$$\omega(s) = 2\pi \frac{[v(s)]^p}{[v(s)]^p + [v(2\pi - s)]^p}, \quad 0 \leq s \leq 2\pi, \quad \text{Eq. 2-52}$$

$$v(s) = \left(\frac{1}{p} - \frac{1}{2}\right) \left(\frac{\pi - s}{\pi}\right)^3 + \frac{1}{p} \frac{s - \pi}{\pi} + \frac{1}{2}, \quad p \geq 2. \quad \text{Eq. 2-53}$$

With Eq. 2-52 and Eq. 2-53, we could further obtain the kernel  $K$  and its diagonal term (see Eq. 2-54 - Eq. 2-60)

$$\begin{aligned}
K(t, \tau) &= K(\omega(s), \omega(\sigma)) \\
&= K_1(\omega(s), \omega(\sigma)) \log\left(4 \sin^2 \frac{s-\sigma}{2}\right) \\
&\quad + \tilde{K}_2(s, \sigma),
\end{aligned} \tag{Eq. 2-54}$$

$$\begin{aligned}
\tilde{K}_2(s, \sigma) &= K(\omega(s), \omega(\sigma)) \\
&\quad - K_1(\omega(s), \omega(\sigma)) \log\left(4 \sin^2 \frac{s-\sigma}{2}\right) \\
&= K_1(\omega(s), \omega(\sigma)) \log\left(\frac{r^2(\omega(s), \omega(\sigma))}{4 \sin^2 \frac{s-\sigma}{2}}\right) \\
&\quad + K_2(\omega(s), \omega(\sigma)),
\end{aligned} \tag{Eq. 2-55}$$

$$\tilde{K}_2(s, s) = 2K_1(t, t) \log(\omega'(s)|x'(t)|) + K_2(t, t). \tag{Eq. 2-56}$$

Then we could obtain the quadrature of the forms after further decomposition

$$\int_0^{2\pi} f(\sigma) d\sigma \approx \frac{\pi}{n} \sum_{j=0}^{2n-1} f(s_j), \tag{Eq. 2-57}$$

$$\int_0^{2\pi} f(\sigma) \log\left(4 \sin^2 \frac{s-\sigma}{2}\right) d\sigma \approx \sum_{j=0}^{2n-1} R_j^{(n)}(s) f(s_j), \tag{Eq. 2-58}$$

where  $0 \leq s \leq 2\pi$ , and  $s_j = \frac{j\pi}{n}$ .

We now define the weights

$$R_j(s) = -\frac{2\pi}{n} \sum_{m=1}^{n-1} \frac{1}{m} \cos m(s - s_j) - \frac{\pi}{n^2} \cos n(s - s_j). \tag{Eq. 2-59}$$

Also, we observe that when  $R_j(s_i) = R_{|i-j|}$ , we have

$$R_k = -\frac{2\pi}{n} \sum_{m=1}^{n-1} \frac{1}{m} \cos \frac{mk\pi}{n} - \frac{(-1)^k \pi}{n^2}. \tag{Eq. 2-60}$$

When the points  $t = t_i = \omega(s_i)$ , the quadrature for  $\int_0^{2\pi} K(t, \tau)\mu(\tau)d\tau$  is expressed in

**Eq. 2-61.**

$$\int_0^{2\pi} K(t_i, \tau)\mu(\tau)d\tau \approx \sum_{j=1}^{2n-1} [K_1(t_i, t_j)W_{ij} + K_2(t_i, t_j)\omega_j]\mu(t_j), \quad \text{Eq. 2-61}$$

where we have  $\omega_j = \frac{\pi}{n}\omega'(s_j)$ , and the weights  $W_{ij}$  is given as **Eq. 2-62** and **Eq. 2-63**

$$W_{ij} = \left( R_{|i-j|} + \frac{\pi}{n} \log \left( \frac{r^2(t_i, t_j)}{4 \sin^2 \frac{s_i - s_j}{2}} \right) \right) \omega'(s_j), \quad \text{Eq. 2-62}$$

$$W_{ii} = \left( R_0 + \frac{2\pi}{n} \log(\omega'(s_i)|\mathbf{x}'(t_i)|) \right) \omega'(s_i). \quad \text{Eq. 2-63}$$

Then we obtain the Nystrom discretization (see **Eq. 2-64** - **Eq. 2-69**)

$$\begin{aligned} G_m &= \left( \frac{1}{2} + \frac{i\eta}{4} \right) u_m^{(n)} + \left( \frac{1}{2} - \frac{i\eta}{4} \right) u_0^{(n)} \\ &- \sum_{j=1}^{2n-1} (H_1(t_m, t_j)W_{mj} + H_2(t_m, t_j)\omega_j)u_j^{(n)} \\ &- \sum_{j=1}^{2n-1} \left( H_0(t_m, t_j) - \frac{i\eta}{2} H_0(0, t_j) \right) \omega_j (u_j^{(n)} - u_0^{(n)}) \\ &- i\eta \sum_{j=1}^{2n-1} \left( \frac{M_{01}(t_m, t_j)}{|x'(t_j)|} W_{mj} + \frac{M_{02}(t_m, t_j)}{|x'(t_j)|} \omega_j \right) \\ &\cdot \sum_{k=1}^{2n-1} (L_1(t_j, t_k)W_{jk} + L_2(t_j, t_k)\omega_k)u_k^{(n)} \\ &- i\eta \sum_{j=1}^{2n-1} \left( \frac{M_{01}(t_m, t_j)}{|x'(t_j)|} W_{mj} + \frac{M_{02}(t_m, t_j)}{|x'(t_j)|} \omega_j \right) \end{aligned} \quad \text{Eq. 2-64}$$

$$\begin{aligned} & \cdot \sum_{k=1}^{2n-1} (M_1(t_j, t_k)W_{jk} + M_2(t_j, t_k)\omega_k)u_k^{(n)} \\ & - i\eta \sum_{j=1}^{2n-1} H_0(t_m, t_j)\omega_j \\ & \cdot \left( \sum_{k=1}^{2n-1} (H_0(t_j, t_k) - H_0(0, t_k))\omega_k (u_k^{(n)} - u_0^{(n)}) \right), \end{aligned}$$

where we have  $u_m^{(n)} \approx u(\mathbf{x}(t_m))$ , and we define the load vector  $G$  as

$$\begin{aligned} G_m &= u^i(\mathbf{x}(t_m)) + \\ & i\eta \sum_{j=0}^{2n-1} (M_{01}(t_m, t_j)W_{mj} + M_{02}(t_m, t_j)\omega_j) \frac{\partial u^i}{\partial v}(\mathbf{x}(t_j)). \end{aligned} \quad \text{Eq. 2-65}$$

Hence, we list the parameters, given by the  $2\pi$ -periodic, and we define  $\psi(t) = \phi(\mathbf{x}(t))$ .

Let  $\mathbf{x}(t) = (x_1(t), x_2(t))$ , so that we have  $|\mathbf{x}'(t)| \geq s_0 > 0$  and  $\mathbf{x}_0 = \mathbf{x}_{2\pi} = \mathbf{x}_0$ .

$$\mathbf{r} = \mathbf{r}(t, \tau) = \mathbf{x}(t) - \mathbf{x}(\tau), \quad r = r(t, \tau) = |\mathbf{r}(t, \tau)|, \quad \text{Eq. 2-66}$$

$$M_{01}(t, t) = -\frac{|\mathbf{x}'(t)|}{4\pi}, \quad M_{02}(t, t) = -\frac{|\mathbf{x}'(t)| \log d}{2\pi}, \quad \text{Eq. 2-67}$$

$$\mathbf{v}(\tau) = n(\mathbf{x}(\tau))|\mathbf{x}'(\tau)| = (-x_2'(\tau), x_1'(\tau)), \quad \text{Eq. 2-68}$$

$$H_0(t, t) = \frac{\mathbf{x}''(t) \cdot \mathbf{v}(t)}{4\pi|\mathbf{x}'(t)|^2}, \quad \text{for } t \neq 0, 2\pi, \quad \text{Eq. 2-69}$$

otherwise,  $H_0(t, \tau) \rightarrow 1/r$  as  $t \rightarrow 0$  and  $\tau \rightarrow 2\pi$ , or as  $t \rightarrow 2\pi$  and  $\tau \rightarrow 0$ . We have the relations among the kernel  $H$ ,  $M$  and  $L$ , which we will introduce as follows.

For  $H$ , we have  $H(t, \tau) = H_1(t, \tau) \log r^2 + H_2(t, \tau)$ , and the diagonal terms

$H_1(t, t) = H_2(t, t) = 0$ . From the non-diagonal terms, we obtain **Eq. 2-70 - Eq. 2-78**

$$H_1(t, \tau) = kJ_1(kr) \frac{\mathbf{r} \cdot \mathbf{v}(\tau)}{4\pi r^2}, \quad \text{Eq. 2-70}$$

$$H_2(t, \tau) = H(t, \tau) - H_1(t, \tau) \log r^2. \quad \text{Eq. 2-71}$$

For  $M$ , we have  $M(t, \tau) = k^2 \nu(t) \cdot \nu(\tau) F(r) = M_1(t, \tau) \log r^2 + M_2(t, \tau)$ , where

$$M_1(t, \tau) = \frac{k^2 \nu(t) \cdot \nu(\tau)}{4\pi} (1 - J_0(kr)), \quad \text{Eq. 2-72}$$

$$M_2(t, \tau) = M(t, \tau) - M_1(t, \tau) \log r^2, \quad \text{Eq. 2-73}$$

and the diagonal terms  $M_1$  and  $M_2$

$$M_1(t, t) = 0, \quad M_2(t, t) = \frac{k^2}{2} \left( \frac{i}{2} - \frac{\gamma + \log\left(\frac{k}{2}\right)}{\pi} \right) |\mathbf{x}'(t)|^2, \quad \text{Eq. 2-74}$$

for  $L$ , we have  $L(t, \tau) = (F'(r) - F''(r)) \frac{\mathbf{r} \cdot \mathbf{x}'(t)}{r} \cdot \frac{\mathbf{r} \cdot \mathbf{x}'(\tau)}{r} - F'(r) \frac{\mathbf{x}'(t) \cdot \mathbf{x}'(\tau)}{r}$ , and

$L(t, \tau) = L_1(t, \tau) \log r^2 + L_2(t, \tau)$ , where

$$L_1(t, \tau) = \frac{k}{4\pi} \left( J_1(kr) - kJ_0(kr) + \frac{J_1(kr)}{r} \right) \frac{\mathbf{r} \cdot \mathbf{x}'(t)}{r} \cdot \frac{\mathbf{r} \cdot \mathbf{x}'(\tau)}{r} - \frac{kJ_1(kr)}{4\pi r} \mathbf{x}'(t) \cdot \mathbf{x}'(\tau), \quad \text{Eq. 2-75}$$

$$L_2(t, \tau) = L(t, \tau) - L_1(t, \tau) \log r^2, \quad \text{Eq. 2-76}$$

and the diagonal terms  $L_1$  and  $L_2$

$$L_1(t, t) = \frac{k^2}{4\pi} |\mathbf{x}'(t)|^2, \quad \text{Eq. 2-77}$$

$$L_2(t, t) = \frac{k^2}{2} \left( \frac{i}{2} - \frac{\gamma + \log\left(\frac{k}{2}\right) + \frac{1}{2}}{\pi} \right) |\mathbf{x}'(t)|^2, \quad \text{Eq. 2-78}$$

where  $\gamma \approx 0.5772156649$  is called the Euler-Msacheroni constant.

Now, we define  $F(z)$ , so let  $F(z) = \frac{i}{4} H_0^{(1)}(kz) + \frac{\log z}{2\pi}$ , then we have **Eq. 2-79**

$$F(z) = \left( \frac{i}{4} - \frac{\gamma + \log\left(\frac{k}{2}\right)}{2\pi} \right) J_0(kz)$$

Eq. 2-79

$$+ \frac{1}{2\pi} \sum_{m=1}^{\infty} \frac{(-1)^m h_m}{(m!)^2} \left(\frac{kz}{2}\right)^{2m} + \frac{1 - J_0(kz)}{4\pi} \log(z^2),$$

where  $h_m = \sum_{j=1}^m j^{-1}$  is the  $m^{\text{th}}$  harmonic number. Hence, we could obtain the solutions in the Neumann boundary condition.

### 2.3 Numerical Experiments

For both the Dirichlet problem and the Neumann problem, we have the far field formula (see Eq. 2-80)

$$u_{\infty}(\hat{x}) = -\frac{e^{\frac{i\pi}{4}}}{\sqrt{8\pi k}} \int_{\partial\Omega} \{k\nu(\mathbf{y}) \cdot \hat{x} + \eta\} e^{-ik\hat{x}\cdot\mathbf{y}} \varphi(\mathbf{y}) ds(\mathbf{y}), \quad \text{Eq. 2-80}$$

where  $|\hat{x}| = 1$ . Normally, the far field means the distribution of the scatter field is at infinity. We can evaluate Eq. 2-80 by the trapezoidal rule after we obtain  $\varphi$ . The multiple corner case is more complicated and we refer to [41]. We take the flower-shaped case, in the Dirichlet boundary condition, as an example in Figure 2-1.

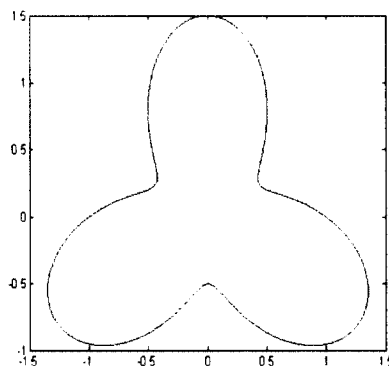


Figure 2-1: The original shape of the flower.

The analytic presentations of the flower shape (see Eq. 2-81 and Eq. 2-82)

$$x(t) = (1 + 0.5 \cos(3t)) \cdot \cos t, \quad \text{Eq. 2-81}$$

and

$$y(t) = (1 + 0.5 \cos(3t)) \cdot \sin t, \quad \text{Eq. 2-82}$$

where  $0 \leq t \leq 2\pi$ .

The approximate values for the far field pattern  $u_\infty(d)$  and  $u_\infty(-d)$  are given from Table 2-1. We define the direction  $d$  of the incident wave is  $d = (1, 0)$ , and the parameter is  $\eta = k$ .

**Table 2-1:** Numerical results for the Nystrom method.

	$n$	$\text{Re } u_\infty(d)$	$\text{Im } u_\infty(d)$	$\text{Re } u_\infty(-d)$	$\text{Im } u_\infty(-d)$
$k = 1$	8	-1.49426582	0.45292727	0.59613494	1.01158165
	16	-1.49468553	0.45141193	0.60125973	1.00591697
	32	-1.49468215	0.45140755	0.60126160	1.00591949
	64	-1.49468215	0.45140755	0.60126160	1.00591949
$k = 5$	8	-1.82503291	1.38164916	0.80398653	0.32856810
	16	-2.09749806	1.49174144	1.21112794	0.46321826
	32	-2.10891458	1.49489236	1.21660030	0.48036662
	64	-2.10891469	1.49489227	1.21660033	0.48036664

From the table above, we could observe that it is the exponential convergence.

Hence, the Nystrom method is accurate and can be applied on simple targets.

## 2.4 The Near Field Data and the Relation to the Far Field Data

In numerical experiments, we also need to compute the near field data. Normally, the near field means the scatter field is evaluated near the targets. By Eq. 2-80, we know how to compute the far field data. By introducing the near field data, we can now introduce the implementation for the near field [9] (see Eq. 2-83 - Eq. 2-85).

$$H_0^1(k\tilde{r}) = H_0^1\left(k\sqrt{(r\cos\theta - x_1)^2 + (r\sin\theta - x_2)^2}\right), \quad \text{Eq. 2-83}$$

$$\begin{aligned} \frac{\partial}{\partial x_1} H_0^1(k\tilde{r}) &= -H_1^1\left(k\sqrt{(r\cos\theta - x_1)^2 + (r\sin\theta - x_2)^2}\right) \\ &\quad \cdot k \frac{x_1 - r\cos\theta}{\sqrt{(r\cos\theta - x_1)^2 + (r\sin\theta - x_2)^2}} \end{aligned} \quad \text{Eq. 2-84}$$

$$\begin{aligned} \frac{\partial}{\partial r} H_0^1(k\tilde{r}) &= [r_1(x_1 - r\cos\theta) + r_2(x_2 - r\sin\theta)] \\ &\quad \cdot \frac{-kH_1^1\left(k\sqrt{(r\cos\theta - x_1)^2 + (r\sin\theta - x_2)^2}\right)}{\sqrt{(r\cos\theta - x_1)^2 + (r\sin\theta - x_2)^2}}. \end{aligned} \quad \text{Eq. 2-85}$$

The formula for the near field data [9] is as Eq. 2-86

$$\begin{aligned} u(x) &= \int_{\partial D} \left[ \frac{\partial \Phi(x, y)}{\partial \nu(y)} - i\eta \Phi(x, y) \right] \varphi(y) ds(y), \\ & \quad x \in \mathbb{R}^2 \setminus \partial D, \end{aligned} \quad \text{Eq. 2-86}$$

where  $\Phi(x, y) = \frac{i}{4} H_0^1(k|x - y|)$ .

Now we replace  $e^{ikx \cdot d}$  with  $\frac{i}{4} H_0^1(k|x - y|)$  for point source incident instead of plane wave. We need to know that the  $d$  in term  $e^{ikx \cdot d}$  is a direction, not dimensity in a later notation.

We define the term  $\tilde{r}$  as Eq. 2-87

$$\tilde{r} = \sqrt{(r \cos \theta - x_1)^2 + (r \sin \theta - x_2)^2}, \quad \text{Eq. 2-87}$$

and the four kinds of situation are

$P_1$ : Point source near field

$P_2$ : Point source far field

$P_3$ : Plane wave near field

$P_4$ : Plane wave far field

then we obtain Eq. 2-88 - Eq. 2-90

$$P_1 = \frac{e^{ik\|x\|}}{\|x\|^{\frac{d-1}{2}}} \left( P_2 + O\left(\frac{1}{\|x\|}\right) \right), \quad \text{Eq. 2-88}$$

$$P_2 = \beta P_3^T, \quad \text{Eq. 2-89}$$

$$P_3 = \frac{e^{ik\|x\|}}{\|x\|^{\frac{d-1}{2}}} \left( P_4 + O\left(\frac{1}{\|x\|}\right) \right). \quad \text{Eq. 2-90}$$

For 2-D:  $\beta = \frac{e^{i\frac{\pi}{4}}}{\sqrt{8\pi k}}$ . For 3-D:  $\beta = \frac{1}{4\pi}$ .

We have the relation between these corresponding singular values [9] as Eq. 2-91

- Eq. 2-93

$$\sigma_{i,1} \approx \frac{1}{\sqrt{r}} \sigma_{i,2}, \quad \text{Eq. 2-91}$$

$$\sigma_{i,2} = \frac{1}{\sqrt{8\pi k}} \sigma_{i,3}, \quad \text{Eq. 2-92}$$

$$\sigma_{i,3} \approx \frac{1}{\sqrt{r}} \sigma_{i,4}. \quad \text{Eq. 2-93}$$

From Eq. 2-91 to Eq. 2-93, we observe that the relations of the singular value in four cases are proportional, which means if we present the numerical results of these four

cases, the results should be similar. In other words, the results should have same shape but different scale.

Now let the source distance be  $R$ , and the receive distance be  $r$ , then We generalize the relations of these four cases and show four formulas as Eq. 2-94 - Eq. 2-97

$$P_1 = \frac{1+i}{4\sqrt{k\pi}} \cdot \frac{e^{ikR}}{\sqrt{R}} P_3 + O\left(R^{-\frac{3}{2}} \cdot r^{-\frac{1}{2}}\right), \quad \text{Eq. 2-94}$$

$$P_2 = \frac{1+i}{4\sqrt{k\pi}} \cdot \frac{e^{ikR}}{\sqrt{R}} P_4 + O\left(R^{-\frac{3}{2}}\right), \quad \text{Eq. 2-95}$$

$$P_3 = \frac{e^{ikr}}{\sqrt{r}} \cdot \left(P_4 + O\left(\frac{1}{r}\right)\right), \quad \text{Eq. 2-96}$$

$$P_4 = \frac{e^{ikr}}{\sqrt{r}} \cdot \left(P_2 + O\left(R^{-\frac{1}{2}} \cdot r^{-1}\right)\right). \quad \text{Eq. 2-97}$$

$P_1$  is the point source incident from distance  $R$ , and the near field receiver at distance  $r$ .

$P_2$  is the point source incident from distance  $R$ , and the far field receiver.

$P_3$  is the plane wave incident, and the near field receiver at distance  $r$ .

$P_4$  is the plane wave incident, and the far field receiver.

If  $R = r$ , we obtain Eq. 2-98 and Eq. 2-99

$$P_1 = \frac{1+i}{4\sqrt{k\pi}} \cdot \frac{e^{2ikr}}{r} P_4 + O(r^{-2}), \quad \text{Eq. 2-98}$$

$$P_2 = \frac{1+i}{4\sqrt{k\pi}} P_3^T. \quad \text{Eq. 2-99}$$

We want to verify the relations of the singular value among the four conditions as above. Now that we know the numerical relations between the far field data and the near field data, we will plot both the images and the singular value of these four experiments

in which we take the kite-shape as an example. The figures look identical with different scales, which verifies the relations of these four cases. In **Figure 2-2** and **Figure 2-3**, the left top is  $P_1$  case, the right top is  $P_2$  case, the left bottom is  $P_3$  and the right bottom is  $P_4$  case.

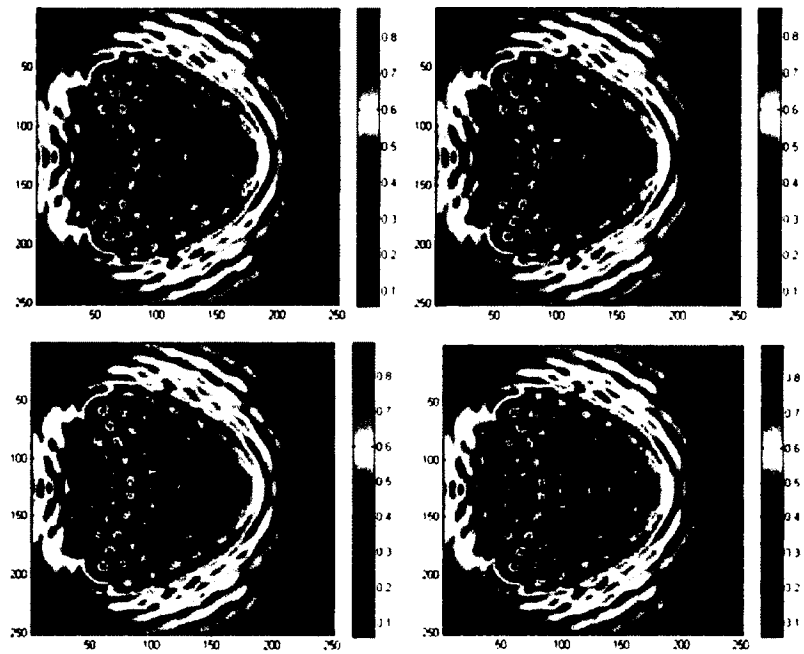


**Figure 2-2:** Kite shaped in four conditions with the Dirichlet boundary condition.

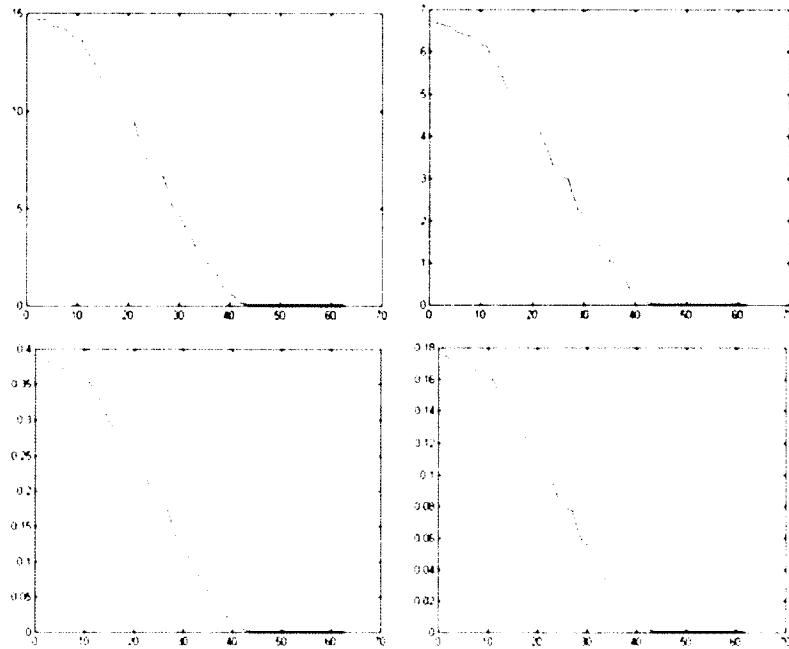


**Figure 2-3:** Singular values of four conditions.

## 2.5 Summary for Forward Problem

In this chapter, we introduce the Helmholtz Equation with two main boundary conditions. After a series of transforming and rewriting, we obtain certain integral equations with kernels. Therefore, we need to discretize the integral equations, which are applied to make discretization by the Nystrom method. Compared to the Galerkin method, the Nystrom method requires the least computational effort, because we only need to compute two integral equations. We clearly observe that the error converges exponentially between the numerical results and the real data.

## CHAPTER 3

### DIRECT METHOD FOR INVERSE PROBLEM

In this chapter, we will introduce two main direct imaging methods, the MUSIC method and the linear sampling method. Sometimes, when we need to obtain a better image of the targets, the multi-tone method is also applied.

#### 3.1 The MUSIC (Multiple Signal Classification) Algorithm

Now we illustrate the setup of the imaging experiment (see **Figure 3-1**).

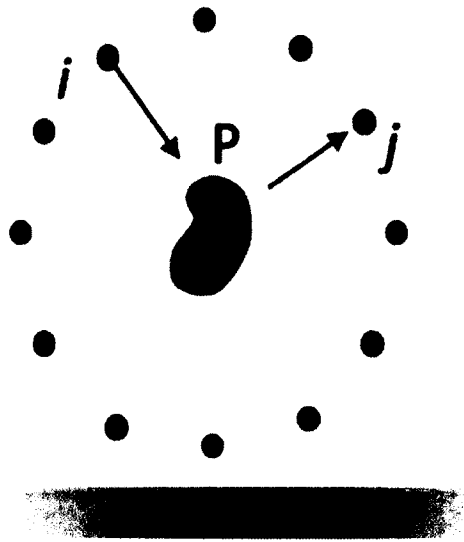


**Figure 3-1:** Generate the response matrix.

We set unknown targets in the middle of the region and transducers around the targets. The transducers can be considered as both receiver and transmitter. We consider

the background medium of the region being homogeneous. Suppose there are  $N$  transducers around the targets with equal spacing in terms of angles, and we label them as  $x_1, \dots, x_N$ . Then we have the Response Matrix  $P_{ij}$ , where the  $j$  stands for the receiving signal at the  $j^{\text{th}}$  transducer for a probing pulse sent out from transducer  $i$ .

**Definition 3.1.1.** The matrix  $P = (P_{ij})_{N \times N}$  is called a Response Matrix if and only if  $P_{ij}$  is the received signal at  $j^{\text{th}}$  transducer for an incident plane wave sent from the  $i^{\text{th}}$  direction or an incident wave sent by the  $i^{\text{th}}$  transducer and  $N$  is the number of transducers.

In some cases,  $P$  may not be a square matrix. There are two main ways to obtain  $P$ , one is to use the solved Helmholtz Equation, and the other one is to obtain it from the physical experiments and measurements. **Figure 3-2** shows how to obtain  $P$  by physical experiments.

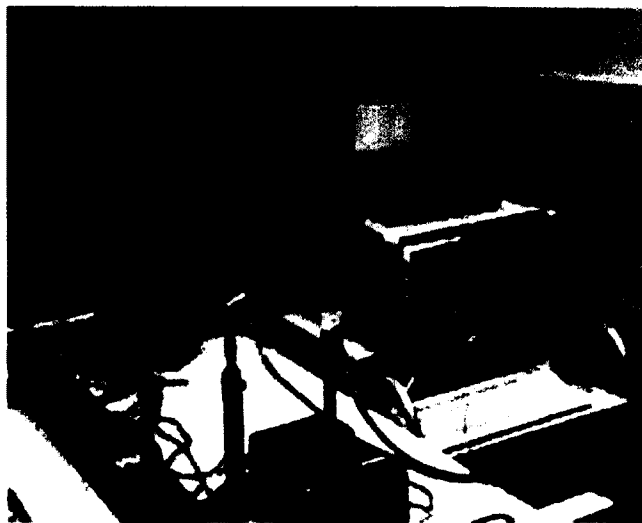


**Figure 3-2:** Obtain the response matrix from lab.

We could handle both near field and far field data. For far field data, the plane incident wave is used at different angles and the far field pattern of the scattered field is

recorded at different angles. For near field data, it just uses the sources and receivers mentioned above.

Due to the Dirichlet boundary condition [20], the scattered far field data (see Eq. 3-1)

$$u_{\infty}(\hat{x}) = -\frac{e^{\frac{i\pi}{4}}}{\sqrt{8\pi k}} \int_{\partial\Omega} \frac{\partial u}{\partial \nu}(\mathbf{y}) e^{-ik\hat{x}\cdot\mathbf{y}} ds(\mathbf{y}), \quad \text{Eq. 3-1}$$

where  $\hat{x}$  is the incident plane wave direction. Hence, the response matrix  $P_{ij}$  can be written as Eq. 3-2

$$P_{ij} = u_{\infty}(\hat{\theta}_j; \hat{\theta}_i) = -\frac{e^{\frac{i\pi}{4}}}{\sqrt{8\pi k}} \int_{\partial\Omega} \frac{\partial u}{\partial \nu}(\mathbf{y}; \hat{\theta}_i) e^{-ik\hat{\theta}_j\cdot\mathbf{y}} ds(\mathbf{y}). \quad \text{Eq. 3-2}$$

**Definition 3.1.2. Illumination Vector.** Let  $G_0(\cdot, \cdot)$  and  $G_D(\cdot, \cdot)$  be the homogeneous and inhomogeneous Green's function, respectively. Define Eq. 3-3 and Eq. 3-4

$$\vec{g}_0(\mathbf{x}) = [G_0(x_1, \mathbf{x}), G_0(x_2, \mathbf{x}), \dots, G_0(x_N, \mathbf{x})]^T, \quad \text{Eq. 3-3}$$

$$\vec{g}_D(\mathbf{x}) = [G_D(x_1, \mathbf{x}), G_D(x_2, \mathbf{x}), \dots, G_D(x_N, \mathbf{x})]^T, \quad \text{Eq. 3-4}$$

where  $x_1, x_2, \dots, x_N$  are the locations of  $N$  transducers. Then  $\vec{g}_0(\mathbf{x})$  and  $\vec{g}_D(\mathbf{x})$  are called the illumination vectors.

Now we have the illumination vector as Eq. 3-5

$$\hat{g}(\mathbf{y}) = [e^{-ik\hat{x}_1\cdot\mathbf{y}}, \dots, e^{-ik\hat{x}_N\cdot\mathbf{y}}]^T. \quad \text{Eq. 3-5}$$

Hence, we can write the matrix form as Eq. 3-6

$$P = -\frac{e^{\frac{i\pi}{4}}}{\sqrt{8\pi k}} \int_{\partial\Omega} \frac{\partial \mathbf{u}}{\partial \nu} \hat{g}^H(\mathbf{y}) ds(\mathbf{y}), \quad \text{Eq. 3-6}$$

where  $\mathbf{u}$  is the vector with components being  $u$  corresponding to different incident angles.

When we obtain the response matrix, the next step is to determine the signal space by SVD of the response matrix. We need to determine a threshold  $r$  and use the first  $r$  singular vectors to image the shape of the targets. We have a thresholding strategy in [19].

The computational cost of SVD is  $O(n^3)$  [42].

We define the MUSIC imaging function for far field data by using the illumination vectors [20] (see Eq. 3-7).

$$I(\mathbf{x}) = \frac{1}{1 - \sum_{j=1}^r |\hat{\mathbf{g}}_0(\mathbf{x})^H \mathbf{v}_j|^2}, \quad \text{Eq. 3-7}$$

where  $\hat{\mathbf{g}}_0$  is the normalized illumination vector, and  $\mathbf{v}_1, \dots, \mathbf{v}_r$  is the first  $r$  leading singular vectors of the response matrix. We need to use the results of multiple frequencies, and we combine the different frequencies of the MUSIC imaging functions, then we have [20] (see Eq. 3-8).

$$I(\mathbf{x}) = \frac{1}{m - \sum_{q=1}^m \sum_{j=1}^r |\hat{\mathbf{g}}_0^q(\mathbf{x})^H \mathbf{v}_j^q|^2}, \quad \text{Eq. 3-8}$$

where  $m$  is the number of frequencies that we use in the MUSIC imaging function.

We just use the denominator part in the above imaging functions in [20]. The nonlinear transform of  $1/x$  is not essential. If the denominator is close to zero, it could make the boundary of the target look disconnected, which would make it difficult for edge detection in Chapter 5. Using the denominator part helps to avoid this problem.

We refer to [21] for the multi-tone imaging function, which is similar to the MUSIC algorithm but used phase coherence.

### 3.2 The Linear Sampling Method

There is another direct imaging method called linear sampling method [29] [37] [43] [44] [45]. Cheney [32] gave a brief description on the linear sampling method. We summarize it as follows: Kirsch [30] considers a situation of the scattering problem, which is when one or more impenetrable objects are scattered off by the incident waves. He also considers the far field operator  $F$ , which satisfies a reciprocity condition but is not self-adjoint, as an integral operator, and the kernel of  $F$  is the far field scattering amplitude.

Kirsch forms the self-adjoint operator [30] (see Eq. 3-9)

$$A = F^*F = \bar{F}F, \quad \text{Eq. 3-9}$$

and considers the eigenvalues  $\lambda_1 \geq \lambda_2 \geq \dots$  and corresponding eigenfunctions  $\mathbf{v}_1, \mathbf{v}_2, \dots$

Based on the theorem [30], the linear sampling method is that the range of  $A^{1/4}$  coincides with the range of the operator  $H$ . We will define the operator  $H$  as follows.

Suppose  $u$  is equal to  $h$  on the boundary of the object. If  $u$  both satisfies the Helmholtz Equation in the region's exterior of the object and the outgoing radiation condition, then we have  $H$ , which maps the Dirichlet data  $h$  to the far field pattern of  $u$ .

In the linear sampling method, the boundary of the object is determined by testing points  $p$ . We denote the far field amplitude by  $g^p$ , which is corresponding to the Green's function  $G(x, p)$ . If  $p$  is inside one of the objects, it means in the region's exterior of the object, then  $G(x, p)$  satisfies the Helmholtz Equation and  $g^p$  is in the range of  $H$ . However, if  $p$  is the exterior of the object,  $G(x, p)$  cannot satisfy the Helmholtz Equation because it has a singularity at  $p$ , which means  $g^p$  cannot be in the range of  $H$ .

The eigenvalues and eigenfunctions of  $A$  can determine the range of  $H$ , which is identical to the range of  $A^{1/4}$  as Kirsch [30] showed. Particularly, we have the range of  $A^{1/4}$  as Eq. 3-10

$$\text{Ran}A^{1/4} = \left\{ f: \sum_j \frac{|\langle v_j, f \rangle|^2}{|\lambda_j|^{1/2}} < \infty \right\}. \quad \text{Eq. 3-10}$$

To plot the quantity  $1/(\sum_j |\lambda_j|^{-1/2} |\langle v_j, g^p \rangle|^2)$  at each point,  $p$  is the algorithm of the linear sampling method. By Kirsch [30], we know that the plot will be nonzero if  $p$  is inside one of the scatterers, and identically zero if  $p$  is outside all the scattering objects.

The linear sampling method can also be applied to electromagnetic waves and in three dimensions by finding an electric field. We briefly summarize the work in [43] as follows:

Let  $D \subset \mathbb{R}^3$  be a bounded domain. We can formulate the direct scattering problem as finding an electric field  $E$  and a magnetic field  $H$  (see Eq. 3-11 - Eq. 3-13)

$$\text{curl}R - ikH = 0, \quad \text{Eq. 3-11}$$

$$\text{curl}H + ikE = 0, \quad \text{in } \mathbb{R}^3 \setminus \bar{D}, \quad \text{Eq. 3-12}$$

where  $E, H \in C_1(\mathbb{R}^3 \setminus \bar{D}) \cap C(\mathbb{R}^3 \setminus \bar{D})$ , then we could obtain

$$\nu \times \text{curl}E - i\lambda(\nu \times E) \times \nu = 0, \quad \text{Eq. 3-13}$$

where  $\nu$  is the unit outward normal to  $\partial D$ , and constant  $\lambda > 0$  which is assumed.

The total fields  $E, H$  are defined as Eq. 3-14 - Eq. 3-18

$$E = E^i + E^s, \quad \text{Eq. 3-14}$$

$$H = H^i + H^s, \quad \text{Eq. 3-15}$$

where  $E^s, H^s$  are scattered field, and  $E^i, H^i$  are the incident field.

$$E^i(x) = \frac{i}{k} \text{curl curl } p e^{ikx \cdot d} = ik(d \times p) \times d e^{ikx \cdot d}, \quad \text{Eq. 3-16}$$

$$H^i(x) = \text{curl } p e^{ikx \cdot d} = ikd \times p e^{ikx \cdot d}, \quad \text{Eq. 3-17}$$

$$\lim_{r \rightarrow \infty} (H^s \times x - rE^s) = 0, \quad \text{Eq. 3-18}$$

where  $k$  is the positive wave number,  $d$  is a unit vector and  $p$  is the polarization vector.

We refer to [9] [45] for the existence and uniqueness of a solution to **Eq. 3-11- Eq. 3-17**.

**Equation 3-16** is called the Silver Muller radiation condition, where  $\hat{x} = \frac{x}{|x|}$  and  $r = |x|$ .

Hence,  $E^s$  has the asymptotic behavior [9] following the Stratton-Chu formula, we have

**Eq. 3-19**

$$E^s(x) = \frac{e^{ik|x|}}{|x|} \left\{ E_\infty(\hat{x}, d, p) + O\left(\frac{1}{|x|}\right) \right\}, \quad \text{Eq. 3-19}$$

where  $E_\infty$  is the electric far-pattern. When  $k$  is fixed, we can simply observed that  $E_\infty$  is infinitely differentiable.

Before we introduce the far-field operator and the corresponding to the Herglotz pairs, we first need to state the Hilbert space  $T^2(\Omega)$  (see **Eq. 3-20**)

$$T^2(\Omega) = \{a: \Omega \rightarrow \mathbb{C}^3 \mid a \in L^2(\Omega), a \cdot \hat{x} = 0 \text{ for } \hat{x} \in \Omega\}, \quad \text{Eq. 3-20}$$

then we define the far-field operator  $F$  (see **Eq. 3-21**)

$$(Fg)(\hat{x}) = \int_{\Omega} E_\infty(\hat{x}, d, g(d)) ds(d), \quad \hat{x} \in \Omega, \quad \text{Eq. 3-21}$$

where  $g \in T^2(\Omega)$ . Hence, the operator  $F$  is a compact linear operator on  $T^2(\Omega)$  after we define **Eq. 3-18** and **Eq. 3-19**. We now define a pair of vector fields, which we mentioned as the Herglotz pair before (see **Eq. 3-22** and **Eq. 3-23**)

$$E(x) = \int_{\Omega} e^{ikx \cdot d} a(d) ds(d), \quad \text{Eq. 3-22}$$

$$H(x) = \frac{1}{ik} \text{curl} E(x), \quad \text{Eq. 3-23}$$

where  $\in \mathbb{R}^3$ , and  $a \in T^2(\Omega)$  is the kernel of  $E, H$ .

We now define a parameter  $q$ , which is considered as the electric dipole with polarization (see Eq. 3-24 - Eq. 3-27)

$$E_e(x, z, q) = \frac{i}{k} \text{curl}_x \text{curl}_x q\Phi(x, z), \quad \text{Eq. 3-24}$$

$$H_e(x, z, q) = \text{curl}_x q\Phi(x, z), \quad \text{Eq. 3-25}$$

where  $z \in D$ , and

$$\Phi(x, z) = \frac{1}{4\pi} \frac{e^{ik|x-z|}}{|x-z|}, \quad x \neq z. \quad \text{Eq. 3-26}$$

For further research, we need to find fixed  $q \in \mathbb{R}^3$  in  $g \in T^2(\Omega)$

$$Fg(\hat{x}) = E_{e,\infty}(\hat{x}, z, q) = \frac{ik}{4\pi} (\hat{x} \times q) \times \hat{x} e^{-ik\hat{x} \cdot z}, \quad \text{Eq. 3-27}$$

where  $E_{e,\infty}$  is the far-field pattern of  $E_e$ .

Now we illustrate the numerical algorithm. We first set an orthonormal basis of  $\mathbb{R}^3$ , where the basis is  $(\hat{x}, e_1(\hat{x}), e_2(\hat{x}))$ , associated with  $\hat{x} \in \Omega$ . Then for all  $\hat{x}, d \in \Omega$  and all  $p \in \mathbb{C}^3$ , we have  $E_\infty(\hat{x}, d, p) \cdot \hat{x} = 0$ . We could rewrite Eq. 3-27 as Eq. 3-28 and

Eq. 3-29

$$\int_{\Omega} e_1(\hat{x}) \cdot E_\infty(\hat{x}, d, g(d, z, q)) ds(d) = e_1(\hat{x}) \cdot E_{e,\infty}(\hat{x}, z, q), \quad \text{Eq. 3-28}$$

$$\int_{\Omega} e_2(\hat{x}) \cdot E_\infty(\hat{x}, d, g(d, z, q)) ds(d) = e_2(\hat{x}) \cdot E_{e,\infty}(\hat{x}, z, q), \quad \text{Eq. 3-29}$$

with the reciprocity relation, we have Eq. 3-30

$$p \cdot E_\infty(\hat{x}, d, q) = q \cdot E_\infty(-d, -\hat{x}, p). \quad \text{Eq. 3-30}$$

Hence, Eq. 3-28 and Eq. 3-29 can be written as Eq. 3-31 and Eq. 3-32

$$\begin{aligned} \int_{\Omega} E_{\infty}(-d, -\hat{x}, e_1(\hat{x})) \cdot g(d, z, q) ds(d) \\ = e_1(\hat{x}) \cdot E_{e, \infty}(\hat{x}, z, q), \end{aligned} \quad \text{Eq. 3-31}$$

$$\begin{aligned} \int_{\Omega} E_{\infty}(-d, -\hat{x}, e_2(\hat{x})) \cdot g(d, z, q) ds(d) \\ = e_2(\hat{x}) \cdot E_{e, \infty}(\hat{x}, z, q), \end{aligned} \quad \text{Eq. 3-32}$$

where for all  $\hat{x}, d \in \Omega$  and all  $p, q \in \mathbb{C}^3$ .

We then use the numerical approximation of the integral to get the discrete form of Eq. 3-31 and Eq. 3-32 (see Eq. 3-33 and Eq. 3-34)

$$\begin{aligned} \sum_N^{j=1} \omega_j E_{\infty}(-d_j, -\hat{x}, e_1(\hat{x})) \cdot g(d_j, z, q) ds(d) \\ = e_1(\hat{x}) \cdot E_{e, \infty}(\hat{x}, z, q), \end{aligned} \quad \text{Eq. 3-33}$$

$$\begin{aligned} \sum_N^{j=1} \omega_j E_{\infty}(-d_j, -\hat{x}, e_2(\hat{x})) \cdot g(d_j, z, q) ds(d) \\ = e_2(\hat{x}) \cdot E_{e, \infty}(\hat{x}, z, q). \end{aligned} \quad \text{Eq. 3-34}$$

Let  $T_h$  be a triangulation of  $\Omega$ , where  $h = \max_{K \in T_h} \text{diam}(K)$ , and  $\omega_j = \sum_{K \in T_h; d_j \in T_h} \frac{|K|}{3}$ . We also define  $|K|$  is the area of  $K$ .

We define  $(\alpha, \beta) \in 1, 2^2$ , and  $(i, j) \in \{1, \dots, N\}^2$ , then we obtain Eq. 3-35

$$A_{\alpha, \beta}(d_j, \hat{x}_i) = \omega_j E_{\infty}(-d_j, -\hat{x}_i, e_{\alpha}(\hat{x}_i)) \cdot e_{\beta}(d_j), \quad \text{Eq. 3-35}$$

and after we combine Eq. 3-33, Eq. 3-34 and Eq. 3-35, we have Eq. 3-36

$$\sum_{j=1}^N \sum_{\beta=1}^2 A_{\alpha,\beta}(d_j, \hat{x}_i) g_{\beta}(d_j, z, q) = e_{\alpha}(\hat{x}_i) E_{e,\infty}(\hat{x}_i, z, q) \quad \text{Eq. 3-36}$$

$$= f_{\alpha}(\hat{x}_i, z, q),$$

where for all  $\alpha \in 1,2$  and all  $i \in \{1, \dots, N\}$ .

Therefore, we simplify Eq. 3-36 and obtain Eq. 3-37 - Eq. 3-40

$$A_{\infty} G(z, q) = F(z, q), \quad \text{Eq. 3-37}$$

$$A_{\infty} = (A_{\alpha,\beta})_{1 \leq \alpha, \beta \leq 2}, \quad \text{Eq. 3-38}$$

$$G(z, q) = (g_{\beta}(z, q))_{1 \leq \beta \leq 2}, \quad \text{Eq. 3-39}$$

$$F(z, q) = (f_{\alpha}(z, q))_{1 \leq \alpha \leq 2}, \quad \text{Eq. 3-40}$$

where  $A_{\infty}$  is a  $2N \times 2N$  matrix, which represent the far field data.  $G(z, q)$  is the vector that we need to compute, and  $F(z, q)$  is the right hand side that we need to choose.

### 3.3 Examples for the MUSIC Algorithm

The analytic presentations of the kite shape are Eq. 3-41 and Eq. 3-42

$$x(t) = \cos t + 0.65 \cos 2t - 0.65, \quad \text{Eq. 3-41}$$

$$y(t) = 1.5 \sin t. \quad \text{Eq. 3-42}$$

The analytic presentations of the teardrop shape are Eq. 3-43 and Eq. 3-44

$$x(t) = 2 \sin \frac{t}{2}, \quad \text{Eq. 3-43}$$

$$y(t) = -\sin t. \quad \text{Eq. 3-44}$$

In **Figure 3-2**, **Figure 3-3**, **Figure 3-4**, and **Figure 3-5**, the frequency of the left top is 4, the right top is 7, the left bottom is 10, and the right bottom is 12. We present four shapes by using the MUSIC imaging function with the Dirichlet boundary condition. We let the frequency  $k = 4, 7, 10, 12$  in the kite-shape, teardrop-shape and flower-shape

experiments. In **Figure 3-6**, we let the frequency of the top figure be 6 and the bottom figure be 7 in the two-object-shape experiment [25]. Also, we let  $N = 64$  for all these four experiments. We observe that there are a lot of artificial lines in these numerical results with single frequency.

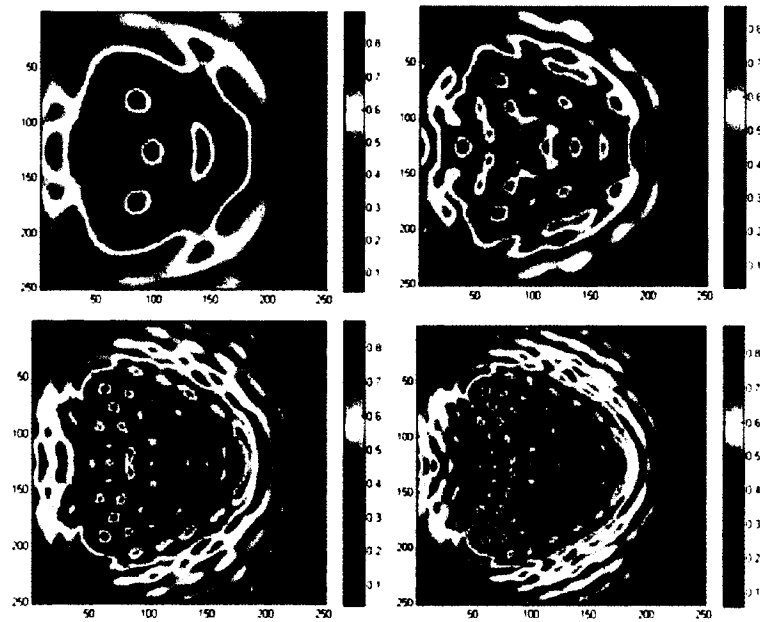


**Figure 3-3:** MUSIC: kite shaped in four different frequencies.

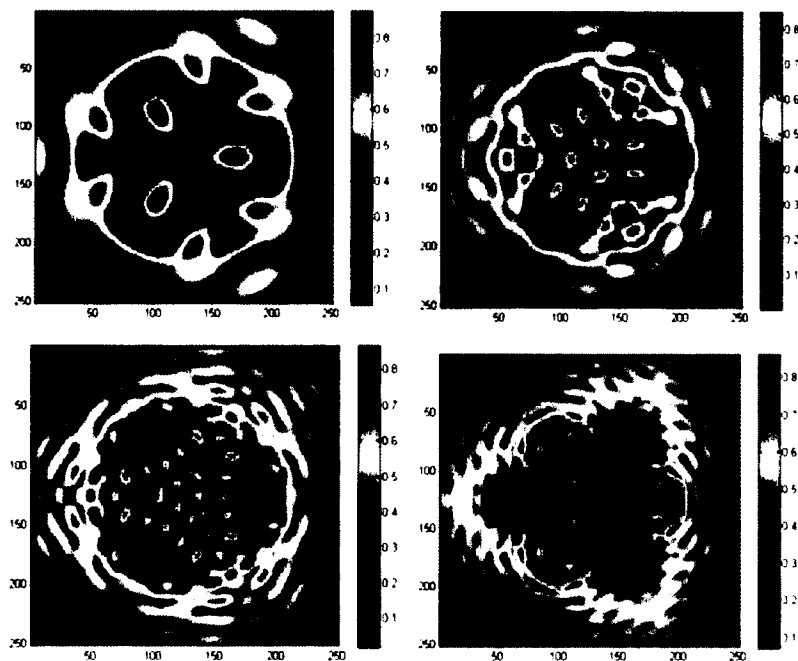


**Figure 3-4:** MUSIC: flower shaped in four different frequencies.

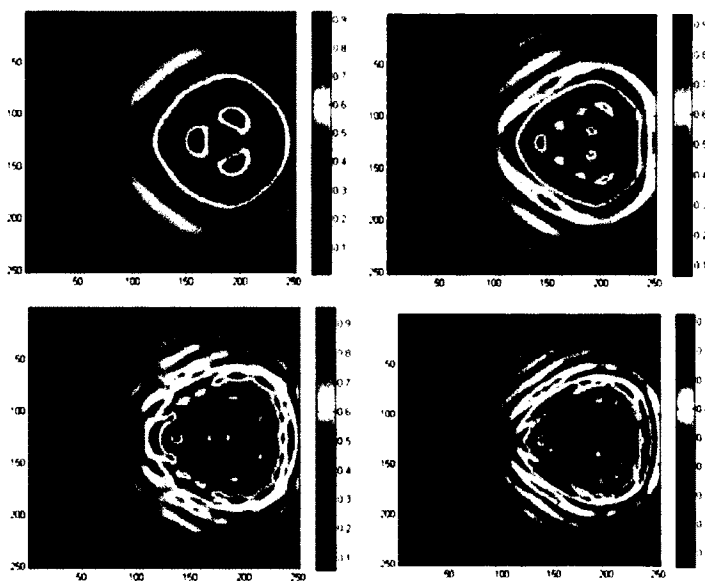


**Figure 3-5:** MUSIC: teardrop shaped in four different frequencies.

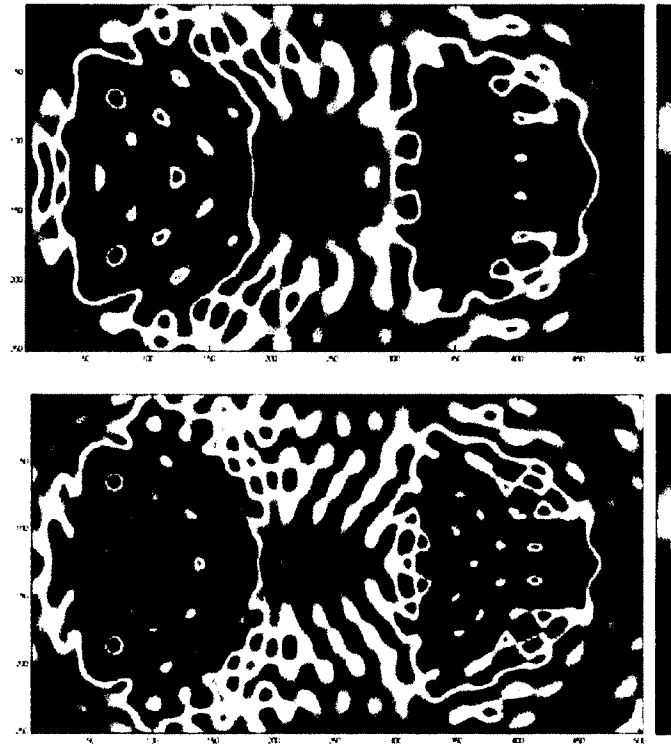


**Figure 3-6:** MUSIC: two objects shaped in two different frequencies.

### 3.4 Example for the Multi-tone Method Using Multiple Frequency Data

In the last section, we observe the artificial lines when we use the MUSIC method. There are three possibilities that form the artificial lines, for example, by solving the forward problem, computational error and the error of forming the response matrix. However, we do need to decrease the effect of the artificial lines. We sum up different multiple frequencies [20] [21] to try to eliminate the lines. The location of the real shape does not change in the different single frequency. However, the artificial lines are affected by the wavelength and if we sum up different numerical results in different frequency, the artificial lines should be decreased.

We present some numerical experiments after we sum up multiple frequencies, including the MUSIC algorithm and the multi-tone method. The multi-tone method is shown in Eq. 3-45

$$I(\mathbf{x}) = \sum_{j=1}^m |\hat{g}_s(\mathbf{x})^H \mathbf{u}_j| |\hat{g}_r(\mathbf{x})^H \bar{\mathbf{v}}_j|. \quad \text{Eq. 3-45}$$

For all these four numerical experiments, we let the number of transducers  $N = 64$ . The frequency  $k$  is set to be 4, 5, 6, 7, 8, ..., 12 in the kite-shape, teardrop-shape and flower-shape experiments, and  $k$  is set to be 4, 4.5, 5, 5.5, ..., 7 in the two-object-shape experiment. **Figure 3-7- Figure 3-10** show the summation of multiple frequencies by using the MUSIC algorithm and the multi-tone method, and the results of summing both the MUSIC algorithm and the multi-tone method [20] [21]. Compared **Figure 3-7- Figure 3-10** to **Figure 3-3- Figure 3-6**, after summation, the artificial lines obviously decrease.

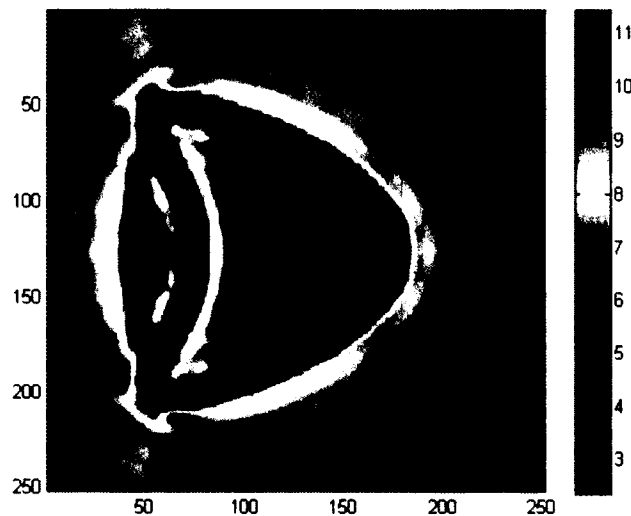


**Figure 3-7:** MUSIC and Multi-tone: kite shape of multiple frequencies.

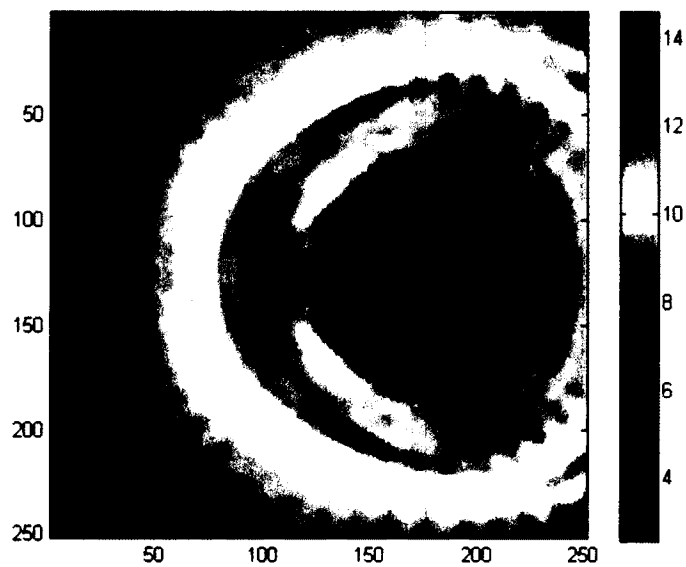


**Figure 3-8:** MUSIC and Multi-tone: teardrop shape of multiple frequencies.

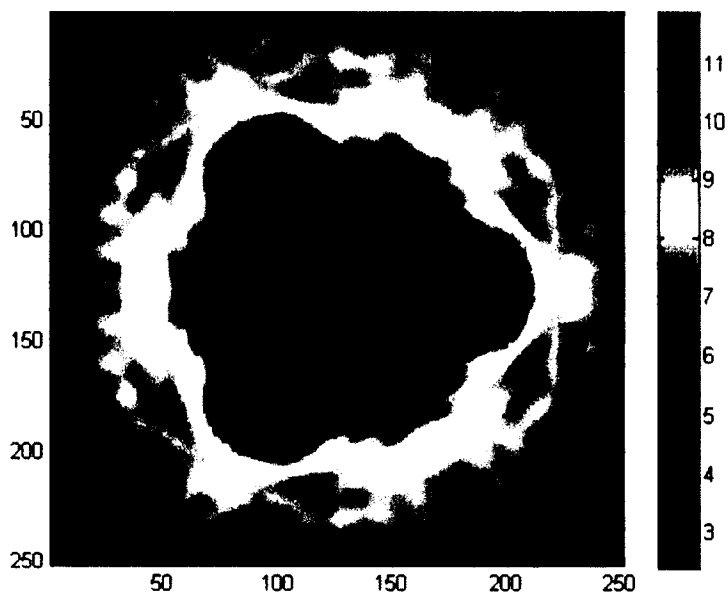


**Figure 3-9:** MUSIC and Multi-tone: flower shape of multiple frequencies.

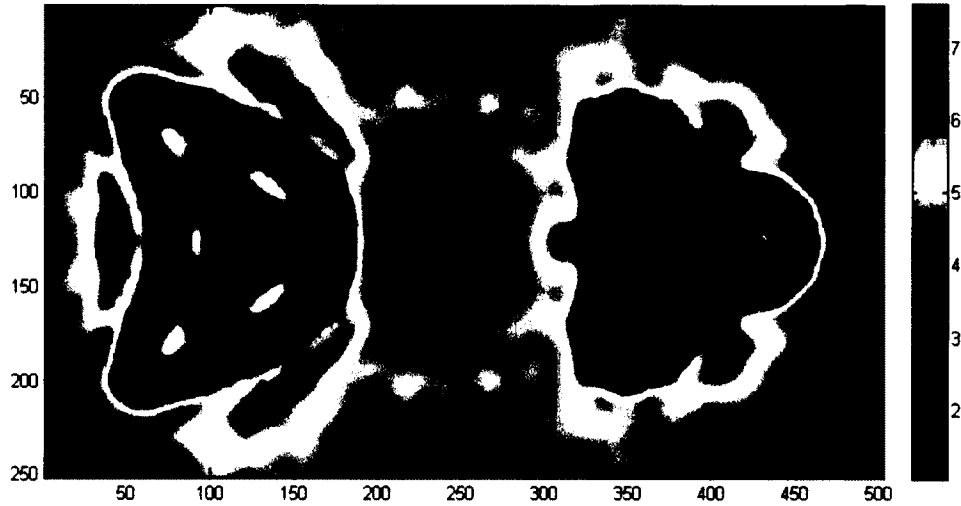


**Figure 3-10:** MUSIC and Multi-tone: two-objects-shape of multiple frequencies.

### 3.5 Summary for Inverse Problem

There are two main methods for solving the inverse problem, the iterative method and the direct method. Compared to the iterative method, the direct method is more efficient. We do not need to compute the forward iteration when we use the direct method. The MUSIC method and the linear method are direct methods. It appears that the linear method is an extension of the MUSIC method.

## CHAPTER 4

### THE SIGNAL SPACE METHOD

In this chapter, we introduce the signal space method. We need to propose a new method to verify if the artificial lines are caused by the error of forward problem. Also, the numerical results are shown in this chapter.

#### 4.1 The Signal Space Test

When we use the MUSIC imaging functions to show the location and the shape of the targets, the artificial lines always come out. However, we want to decrease the effect of the artificial lines and find out if we could eliminate these lines by using the signal space method.

**Definition 4.1.1. Signal Space.** Let  $\vec{u}_i$  be the singular vectors with singular values  $\sigma_i$  of the response matrix  $P$ . Define the signal space (see Eq. 4-1)

$$V_s = \text{span}\{\vec{u}_i | i \leq n\}, \quad \text{Eq. 4-1}$$

where  $n$  is a threshold depending on the resolution of the array and the noise level.

By numerical experiments, we can determine the threshold parameter  $n$  using the resolution analysis.

Steps of the signal space test are shown below:

1. Create the shape of the targets by using their parametric equations.

2. For each sample point on the target boundary, generate a far field illumination vector corresponding to it. Collect these illumination vectors to create a matrix.
3. Take SVD of the matrix [19] [20].
4. Determine threshold  $r$  and use from the  $r + 1$  singular vector to the last. These vectors span the noise space orthogonal to the signal space. Now compute the project to the noise space for the illumination vectors corresponding to each point. Those in the signal space would show a low projection value.

Note that this procedure uses the target shape information. The purpose is to check if the artificial lines are due to the error in the forward solver. The key idea of the MUSIC algorithm uses the concept of signal space. Ideally, those points on the boundary have their illumination vectors falling in the signal space and therefore the projection to the noise space is zero. In reality, some other points not on the boundary also have their illumination vectors with nearly zero projection to the noise space. The above signal space test would show whether we still observe artificial lines with the knowledge of the exact shape of the targets. **Figure 4-1** and **Figure 4-2** show the original shape of the targets.

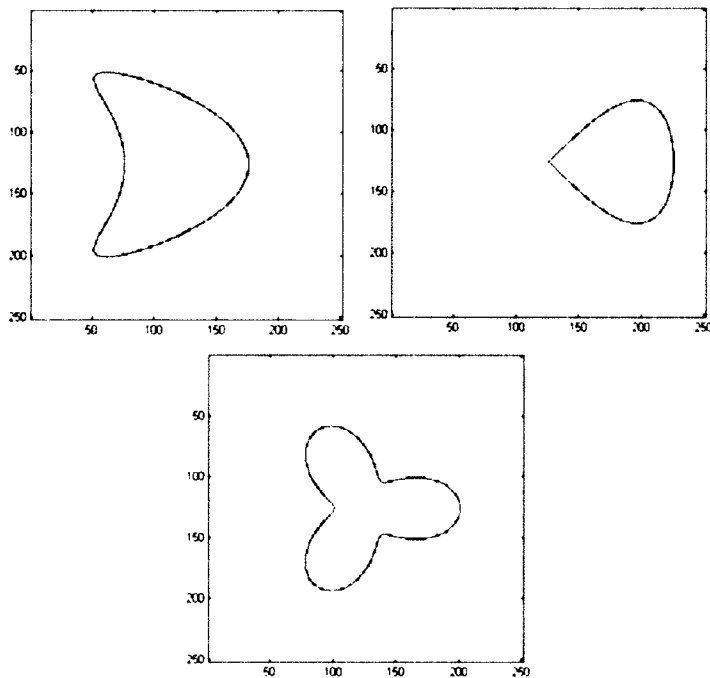


**Figure 4-1:** Three shapes of the targets by their parametric equations.

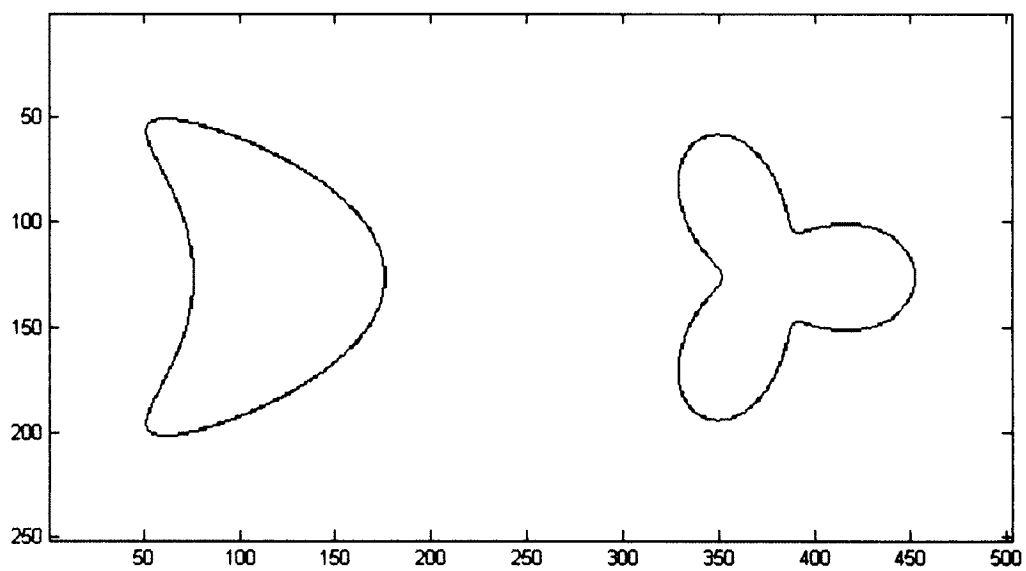


**Figure 4-2:** Two-objects-shape of the targets by their parametric equations.

## 4.2 Numerical Results

In **Figure 4-3-Figure 4-6**, by using the signal space method, we let frequency  $k = 4, 7, 10, 12$  in the kite-shape, teardrop-shape and flower-shape experiments, and  $k = 6, 7$  in the two-object experiment. Let  $N = 64$  for all these four experiments. Even though we do not apply imaging functions and the response matrix here, the artificial lines still appear. Thus, we know that the artificial lines are not caused by the error of the forward problems.

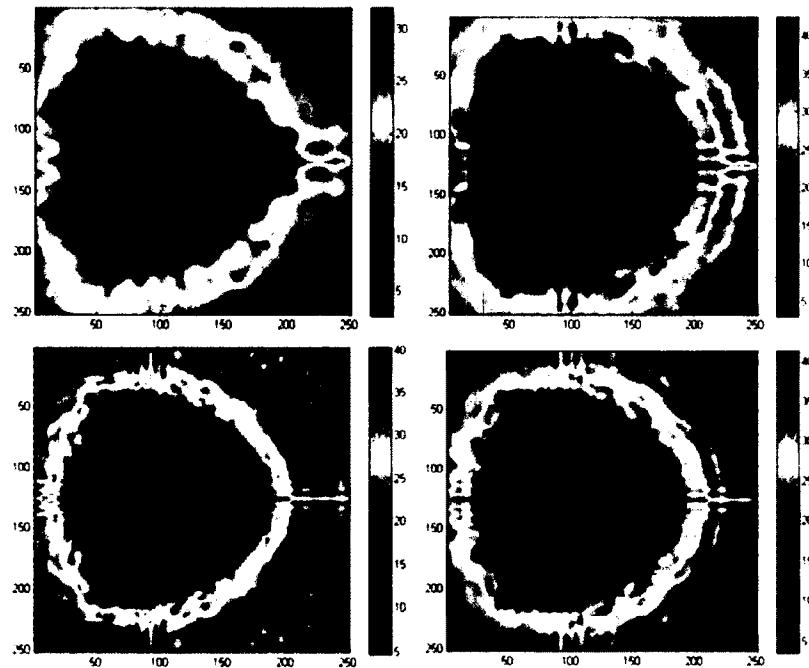


**Figure 4-3:** Signal space test: kite shape in four different frequencies.

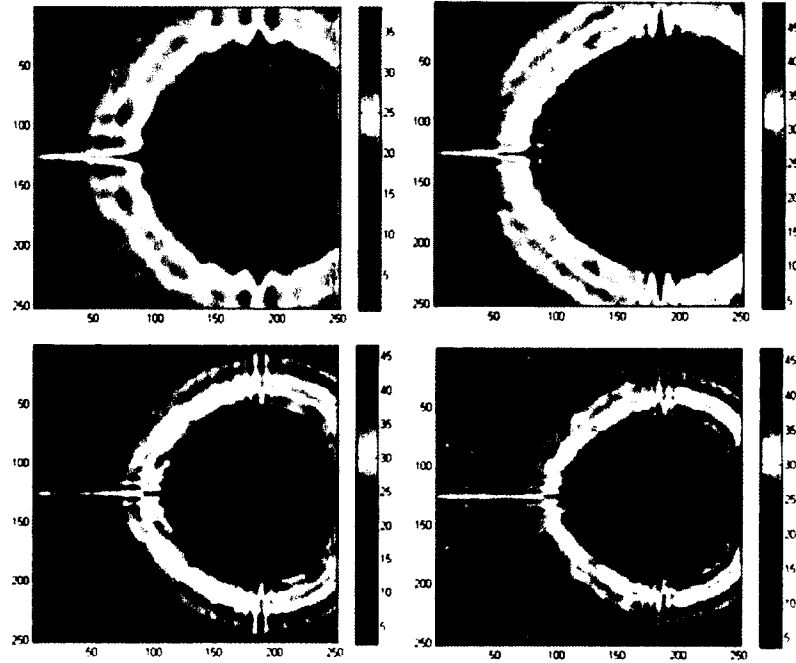


Figure 4-4: Signal space test: teardrop shape in four different frequencies.

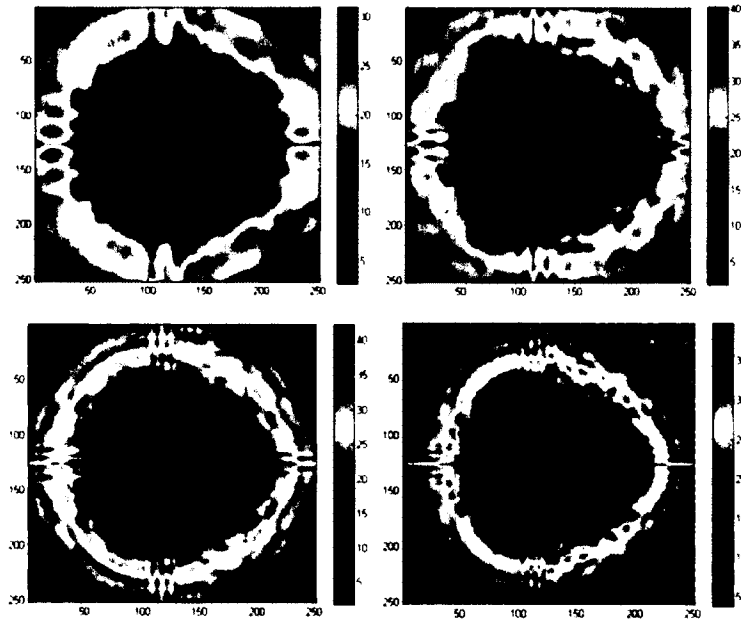
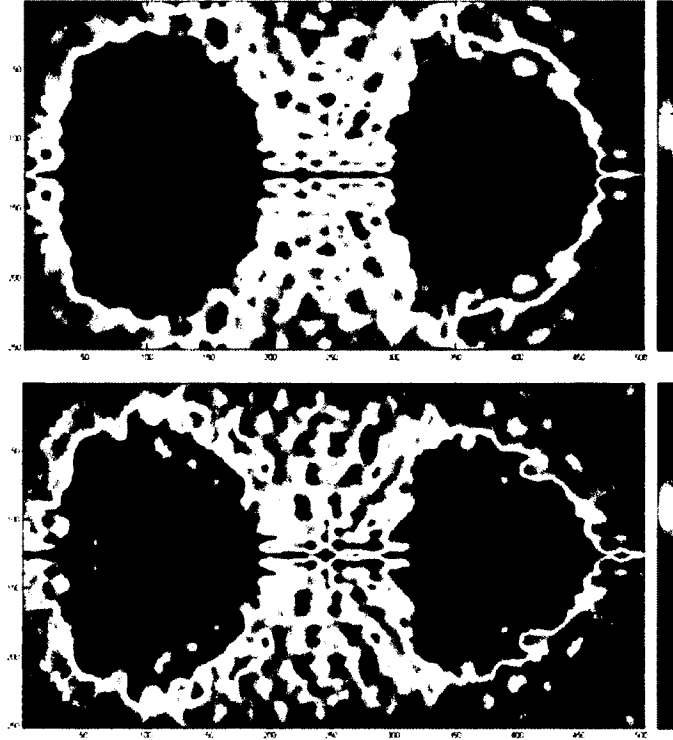


Figure 4-5: Signal space test: flower shape in four different frequencies.



**Figure 4-6:** Signal space test: two-objects-shape in two different frequencies.

### 4.3 Summary for the Signal Space Method

There are many possible reasons to cause the artificial lines, such as the error of computing the forward problem, and the creation of the response matrix. We could not use the signal space test to eliminate the artificial lines. However, we eliminate one possible reason to cause them. We do not solve the forward problem, but the artificial lines still come out.

## CHAPTER 5

### THE IMPROVED METHOD

In this chapter, we introduce the active contour method, and the level set data. We improved the imaging method by obtain the level set data and use them to recreate the shape of the targets.

#### 5.1 Active Contour Method

The active contour method [34] is based on the level set method, and segmentation of the Mumford-Shah functional and curve evolution. By using the active contour method, we can detect objects (edges) in given images. The main idea is to construct a cost functional, then minimize it to evolve a curve and finally stop at the boundary (edges) of the objects.

Steps are as follows:

1. In order to detect objects in a given image, we first evolve a curve  $C(s): [0, 1] \rightarrow \mathbb{R}^2$ , which is parameterized.
2. Let the given image  $u_0: \bar{\Omega} \rightarrow \mathbb{R}$ . Let  $\Omega$  be a bounded open subset of  $\mathbb{R}^2$ , and its boundary is  $\partial\Omega$ .
3. Around the object, we start with a curve (for example a box) to detect it. By minimizing an energy functional, the curve should move to the object and stop at the boundary.

Now we introduce the level set method [46] (see Eq. 5-1- Eq. 5-10)

$$C = \partial\omega = \{(x, y) \in \Omega: \phi(x, y) = 0\}, \quad \text{Eq. 5-1}$$

$$\text{inside}(C) = \omega = \{(x, y) \in \Omega: \phi(x, y) > 0\}, \quad \text{Eq. 5-2}$$

$$\text{outside}(C) = \Omega \setminus \omega = \{(x, y) \in \Omega: \phi(x, y) < 0\}, \quad \text{Eq. 5-3}$$

where  $\omega \subset \Omega$  is open and  $C = \partial\omega$ . We follow [47] to replace  $C$  by  $\phi$ .

By using the Heaviside function  $H$  and Dirac measure  $\delta_0$ , we define

$$H(z) = \begin{cases} 1, & \text{if } z \geq 0, \\ 0, & \text{if } z < 0, \end{cases} \quad \text{Eq. 5-4}$$

$$\delta_0 = \frac{d}{dz} H(z), \quad \text{Eq. 5-5}$$

and two constants  $c_1$  and  $c_2$  by function of  $\phi$  and  $H$

$$c_1(\phi) = \frac{\int_{\Omega} u_0(x, y) H(\phi(x, y)) dx dy}{\int_{\Omega} H(\phi(x, y)) dx dy}, \quad \text{Eq. 5-6}$$

$$\text{if } \int_{\Omega} H(\phi(x, y)) dx dy > 0,$$

$$c_2(\phi) = \frac{\int_{\Omega} u_0(x, y) (1 - H(\phi(x, y))) dx dy}{\int_{\Omega} (1 - H(\phi(x, y))) dx dy}, \quad \text{Eq. 5-7}$$

$$\text{if } \int_{\Omega} (1 - H(\phi(x, y))) dx dy > 0,$$

after we have  $c_1$ ,  $c_2$  and  $F_{\epsilon}$  where  $\epsilon \rightarrow 0$  [34], we define the equation for  $\phi$  with the

initial contour  $\phi(0, x, y) = \phi_0(x, y)$

$$\begin{aligned} \frac{\partial \phi}{\partial t} = \delta_{\epsilon}(\phi) \left[ \mu \operatorname{div} \left( \frac{\nabla \phi}{|\nabla \phi|} \right) - v - \lambda_1 (u_0 - c_1)^2 \right. \\ \left. + \lambda_2 (u_0 - c_2)^2 \right] = 0 \text{ in } (0, \infty), \end{aligned} \quad \text{Eq. 5-8}$$

$$\phi(0, x, y) = \phi_0(x, y) \quad \text{in } \Omega, \quad \text{Eq. 5-9}$$

$$\frac{\delta_\epsilon(\phi)}{|\nabla\phi|} \frac{\partial\phi}{\partial\vec{n}} = 0 \quad \text{on } \partial\Omega. \quad \text{Eq. 5-10}$$

We now try to derive **Eq. 5-10**. The energy functional  $F$  is defined as **Eq. 5-11**

$$\begin{aligned} F(c_1, c_2, C) &= \mu \cdot \text{Length}(C) + \nu \cdot \text{Area}(\text{inside}(C)) \\ &+ \lambda_1 \int_{\text{inside}(C)} |u_0(x, y) - c_1|^2 dx dy \\ &+ \lambda_2 \int_{\text{outside}(C)} |u_0(x, y) - c_2|^2 dx dy \\ &= \mu \int_{\Omega} \delta(\phi) |\nabla\phi| dx dy + \nu \int_{\Omega} H(\phi) dx dy \\ &+ \lambda_1 \int_{\Omega} |u_0 - c_1|^2 H(\phi) dx dy \\ &+ \lambda_2 \int_{\Omega} |u_0 - c_2|^2 (1 - H(\phi)) dx dy, \end{aligned} \quad \text{Eq. 5-11}$$

where  $\mu, \nu \geq 0$  and  $\lambda_1, \lambda_2 > 0$  are fixed parameters. We want to derive the Euler-

Lagrange equation and compute the Gateaux Derivative. We have  $\lim_{\epsilon \rightarrow 0} \frac{F(\phi + \epsilon\psi) - F(\phi)}{\epsilon}$

and set it equal to 0. Since  $H' = \delta$ , then the terms of **Eq. 5-11** corresponding to

$\int_{\Omega} \delta(\phi) (\nu + \lambda_1 |u_0 - c_1|^2 - \lambda_2 |u_0 - c_2|^2) \psi dx dy$ , we just need to work on the term

$\mu \int_{\Omega} \delta(\phi) |\nabla\phi| dx dy$ .

For simplicity of notation, we let  $G(\phi) = \int_{\Omega} \delta(\phi)|\nabla\phi|dxdy$ . Hence, we have

Eq. 5-12

$$\begin{aligned}
& \lim_{\epsilon \rightarrow 0} \frac{G(\phi + \epsilon\psi) - G(\phi)}{\epsilon} \\
&= \lim_{\epsilon \rightarrow 0} \frac{\int_{\Omega} (\delta(\phi + \epsilon\psi))|\nabla(\phi + \epsilon\psi)| - \delta(\phi)|\nabla\phi|dxdy}{\epsilon} \\
&= \lim_{\epsilon \rightarrow 0} \frac{\int_{\Omega} (\delta(\phi + \epsilon\psi))|\nabla(\phi + \epsilon\psi)| - \delta(\phi)|\nabla(\phi + \epsilon\psi)|dxdy}{\epsilon} \\
&+ \lim_{\epsilon \rightarrow 0} \frac{\int_{\Omega} (\delta(\phi)|\nabla(\phi + \epsilon\psi)| - \delta(\phi)|\nabla\phi|)dxdy}{\epsilon} \\
&= \int_{\Omega} \delta'(\phi)|\nabla\phi|\psi dxdy \\
&+ \int_{\Omega} \delta(\phi) \lim_{\epsilon \rightarrow 0} \frac{|\nabla(\phi + \epsilon\psi)| - |\nabla\phi|}{\epsilon} dxdy \\
&= \int_{\Omega} \delta'(\phi)|\nabla\phi|\psi dxdy \\
&+ \int_{\Omega} \delta(\phi) \lim_{\epsilon \rightarrow 0} \frac{2\epsilon\nabla\phi\nabla\psi + \epsilon^2\nabla\psi\nabla\psi}{\epsilon(|\nabla(\phi + \epsilon\psi)| + |\nabla\phi|)} dxdy \\
&= \int_{\Omega} \delta'(\phi)|\nabla\phi|\psi dxdy + \int_{\Omega} \delta(\phi) \lim_{\epsilon \rightarrow 0} \frac{2\epsilon\nabla\phi\nabla\psi}{\epsilon \cdot 2|\nabla\phi|} dxdy \\
&= \int_{\Omega} (\delta'(\phi)|\nabla\phi|\psi + \delta(\phi) \frac{\nabla\phi}{|\nabla\phi|} \nabla\psi) dxdy.
\end{aligned}$$

Eq. 5-12

Now we need to apply Green's Theorem (see Eq. 5-13 and Eq. 5-14)

$$\begin{aligned}
 & \int_{\Omega} \delta(\phi) \frac{\nabla\phi}{|\nabla\phi|} \nabla\psi dx dy \\
 &= \int_{\partial\Omega} \frac{\delta(\phi)}{|\nabla\phi|} \frac{\partial\phi}{\partial n} \psi ds \\
 & - \int_{\Omega} \nabla \cdot \left( \delta(\phi) \frac{\nabla\phi}{|\nabla\phi|} \right) \psi dx dy;
 \end{aligned} \tag{Eq. 5-13}$$

therefore,

$$\begin{aligned}
 & \lim_{\epsilon \rightarrow 0} \frac{G(\phi + \epsilon\psi) - G(\phi)}{\epsilon} \\
 &= \int_{\Omega} \delta'(\phi) |\nabla\phi| \psi - \nabla \cdot \left( \delta(\phi) \frac{\nabla\phi}{|\nabla\phi|} \right) \psi dx dy \\
 &+ \int_{\partial\Omega} \frac{\delta(\phi)}{|\nabla\phi|} \frac{\partial\phi}{\partial n} \psi ds \\
 &= \int_{\Omega} \delta'(\phi) |\nabla\phi| \psi - \delta'(\phi) \frac{\nabla\phi \cdot \nabla\phi}{|\nabla\phi|} \psi \\
 &- \delta(\phi) \nabla \cdot \left( \frac{\nabla\phi}{|\nabla\phi|} \right) \psi dx dy + \int_{\partial\Omega} \frac{\delta(\phi)}{|\nabla\phi|} \frac{\partial\phi}{\partial n} \psi ds \\
 &= - \int_{\Omega} \delta(\phi) \nabla \cdot \left( \frac{\nabla\phi}{|\nabla\phi|} \right) \psi dx dy \\
 &+ \int_{\partial\Omega} \frac{\delta(\phi)}{|\nabla\phi|} \frac{\partial\phi}{\partial n} \psi ds.
 \end{aligned} \tag{Eq. 5-14}$$

Finally, when we put the terms together, we have **Eq. 5-15**

$$\begin{aligned} & \lim_{\epsilon \rightarrow 0} \frac{F(\phi + \epsilon\psi) - F(\phi)}{\epsilon} \\ &= \int_{\Omega} \delta(\phi) [-\mu \nabla \cdot \left( \frac{\nabla \phi}{|\nabla \phi|} \right) + \nu + \lambda_1 |u_0 - c_1|^2 \\ & \quad - \lambda_2 |u_0 - c_2|^2] \psi dx dy + \int_{\partial\Omega} \frac{\delta(\phi)}{|\nabla \phi|} \frac{\partial \phi}{\partial n} \psi ds, \end{aligned} \quad \text{Eq. 5-15}$$

and both integrals above are set to 0.

Now we are introducing pseudo time (see **Eq. 5-16** and **Eq. 5-17**)

$$\begin{aligned} \frac{\partial \phi}{\partial t} &= \delta(\phi) \left[ \mu \nabla \cdot \left( \frac{\nabla \phi}{|\nabla \phi|} \right) - \nu - \lambda_1 |u_0 - c_1|^2 + \lambda_2 |u_0 - c_2|^2 \right] \\ &= 0, \end{aligned} \quad \text{Eq. 5-16}$$

and

$$\frac{\delta(\phi)}{|\nabla \phi|} \frac{\partial \phi}{\partial n} = 0 \quad \text{on } \partial\Omega. \quad \text{Eq. 5-17}$$

Then we use  $\frac{\partial F}{\partial c_1} = \frac{\partial F}{\partial c_2} = 0$  to get **Eq. 5-6** and **Eq. 5-7**.

## 5.2 Level-set Algorithm

The steps of the level-set algorithm [34] are as follows:

1. Use  $\phi^0$  to initialize  $\phi_0$ , where  $n = 0$ .
2. Use **Eq. 5-6** and **Eq. 5-7** to compute  $c_1(\phi^n)$  and  $c_2(\phi^n)$ .
3. In order to obtain  $\phi^{n+1}$ , we use **Eq. 5-8**, **Eq. 5-9** and **Eq. 5-10** to solve PDE in  $\phi$ .
4. If the solution is stationary, stop. If not,  $n + 1$  and repeat.

Using the finite differences equations, we implement Eq. 5-16 [48] and obtain Eq. 5-18.

$$\begin{aligned}
& \frac{\phi_{i,j}^{n+1} - \phi_{i,j}^n}{\Delta t} \\
& = \delta_h(\phi_{i,j}^n) \left[ \frac{\mu}{h^2} \Delta x \cdot \left( \frac{\Delta_+^x \phi_{i,j}^{n+1}}{\sqrt{\frac{(\Delta_+^x \phi_{i,j}^n)^2}{h^2} + \frac{(\phi_{i,j+1}^n - \phi_{i,j-1}^n)^2}{(2h)^2}}} \right) \right. \\
& \quad + \frac{\mu}{h^2} \Delta y \cdot \left( \frac{\Delta_+^y \phi_{i,j}^{n+1}}{\sqrt{\frac{(\phi_{i+1,j}^n - \phi_{i-1,j}^n)^2}{(2h)^2} + \frac{(\Delta_+^y \phi_{i,j}^n)^2}{h^2}}} \right) \\
& \quad - v - \lambda_1 (u_{0,i,j} - c_1(\phi^n))^2 \\
& \quad \left. + \lambda_2 (u_{0,i,j} - c_2(\phi^n))^2 \right] \tag{Eq. 5-18}
\end{aligned}$$

When we finish detecting the contours of the targets, the solution is stationary.

We obtain all the level-set data from the images. Then we need to find the data which is exactly located on the boundary of the targets.

### 5.3 Numerical Results

The kite-shape and flower-shape have no corners. The teardrop-shape and two-object-shape have just one corner. In order to make sure the active contour method is proper, we take the multiple corners plane-shape [41] as an example. Parameters for the plane-shape,  $k$  is set to be 4, 5, 6, 7, 8, ..., 12, and the number of transducers is 64.

The equations for each arc of the plane-shape are Eq. 5-19 - Eq. 5-27

$$y = -\frac{3}{8}t^2 + \frac{3}{8}, \quad \text{Eq. 5-19}$$

$$y = \frac{3}{8}t^2 - \frac{3}{8}, \quad \text{Eq. 5-20}$$

$$y = 6t^2 - 1, \quad \text{Eq. 5-21}$$

$$y = -6t^2 + 1, \quad \text{Eq. 5-22}$$

$$y = \frac{1}{3}, \quad \text{Eq. 5-23}$$

$$y = -\frac{1}{3}, \quad \text{Eq. 5-24}$$

$$x = -\frac{3}{2}, \quad \text{Eq. 5-25}$$

$$y = \frac{16}{3}\left(t + \frac{5}{4}\right)^2 - \frac{2}{3}, \quad \text{Eq. 5-26}$$

$$y = -\frac{16}{3}\left(t + \frac{5}{4}\right)^2 + \frac{2}{3}. \quad \text{Eq. 5-27}$$

In Section 3.4, we know that when we use the multi-tone method with multiple frequency, we can obtain better images of the unknown targets, which means we can obtain the images with less artificial lines compared with the images of the single frequency. However, there are still some artificial lines in the images, we need to know the exact shape of the targets. That is why we need to use the active contour method and the level-set algorithm. We will introduce the detail of the procedures.

In the numerical experiments, we first need to find the contour of the targets by using the active contour method, we use **Figure 3-7- Figure 3-10** as the given images and the box of each figure as the initial contours. We obtain the figures with contours on the boundary of the targets (See **Figure 5-1 - Figure 5-5**).

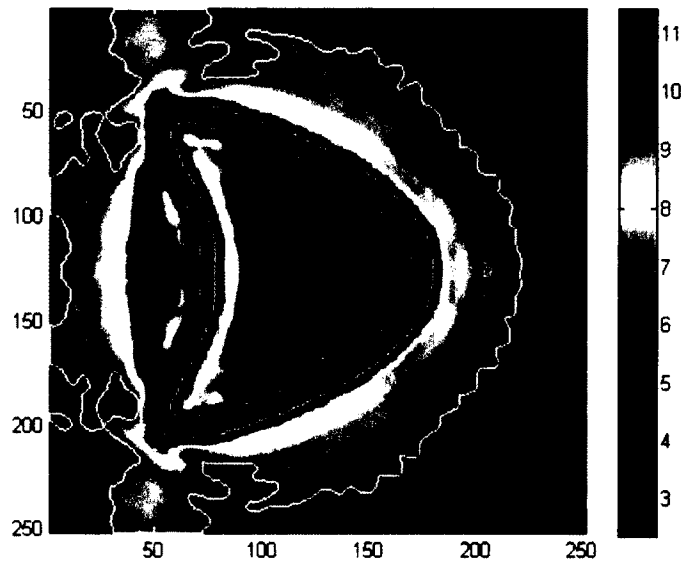


**Figure 5-1:** Contours of the kite shape.

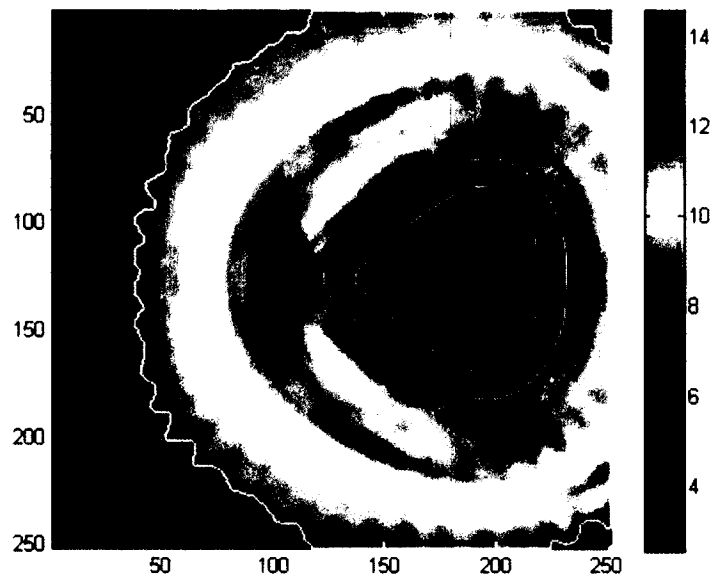


**Figure 5-2:** Contours of the teardrop shape.

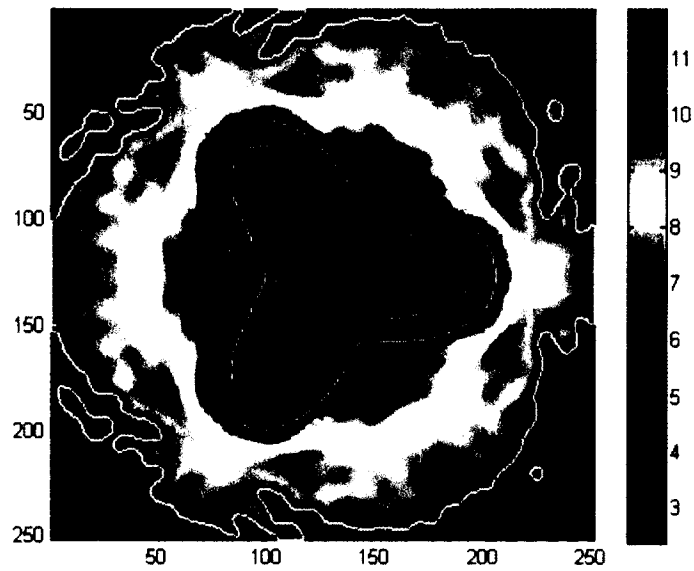


**Figure 5-3:** Contours of the flower shape.

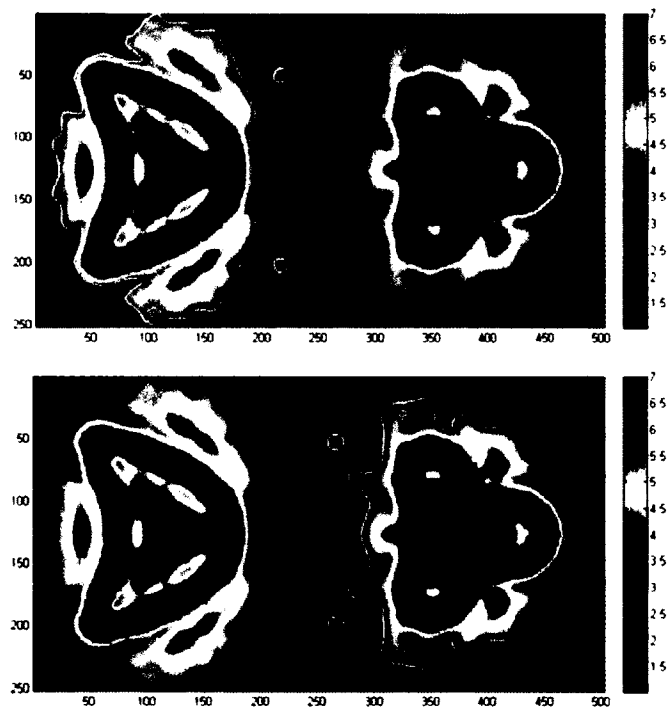


**Figure 5-4:** Contours of the two-object-shape: the figure on top is the contours of the left object; figure on the bottom is the contours of the right object.

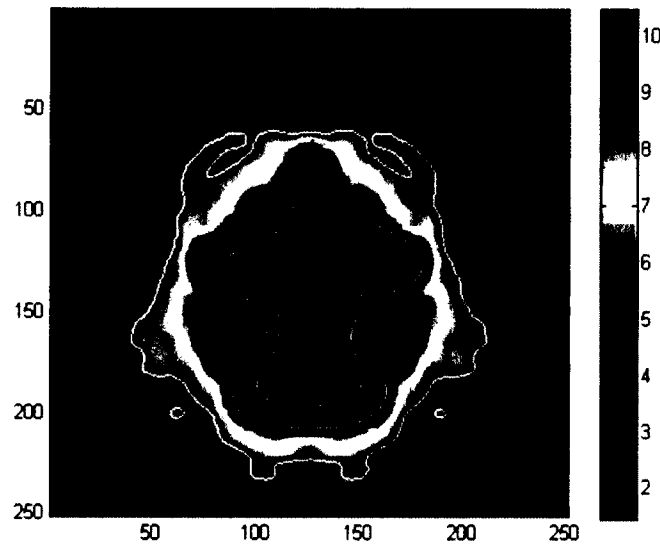


**Figure 5-5:** Contours of the plane shape.

In the two-object-case, by using the active contour method, we could not directly find both contours. We first fix the center-point in each target, then split the image, and find each contour at one time. After we have both contours, we combine both contours together and put the center-point of the contour back to the fixed center.

From **Figure 5-1 - Figure 5-5**, we observe there are some contours in the images. We need to distinguish what contours belong to the targets, and eliminate the rest of them. We know that the contours of the targets are close, but when we look for them from the level-set data, which forms the contours, we need to find the two lines which are close (see **Figure 5-6 - 5-10**).

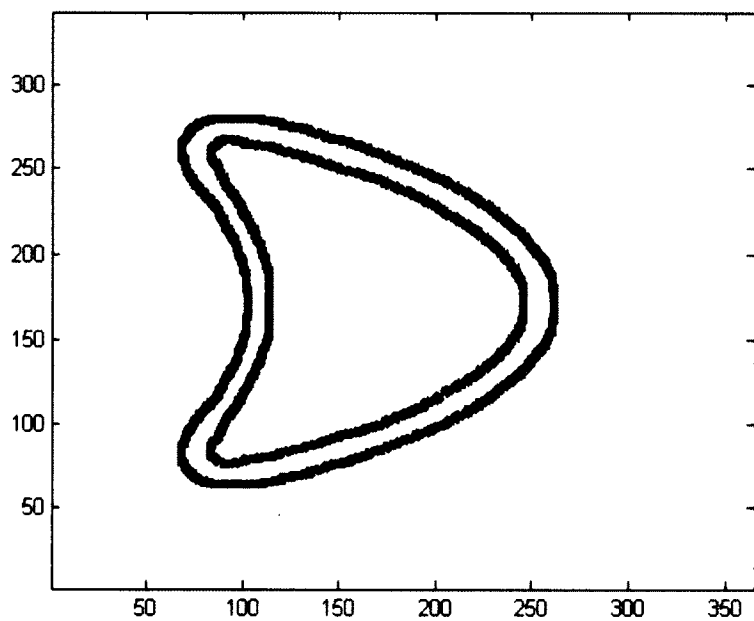


**Figure 5-6:** The level set lines of the kite shape.

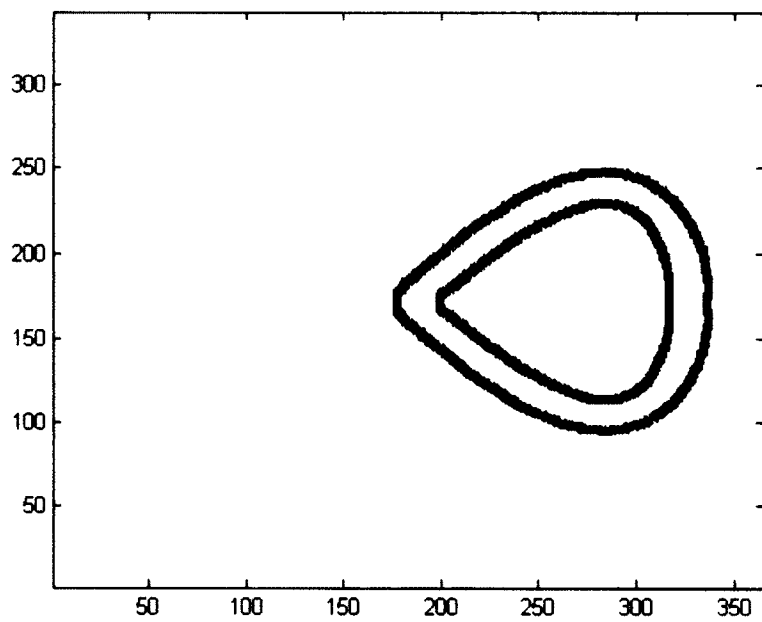


**Figure 5-7:** The level set lines of the teardrop shape.

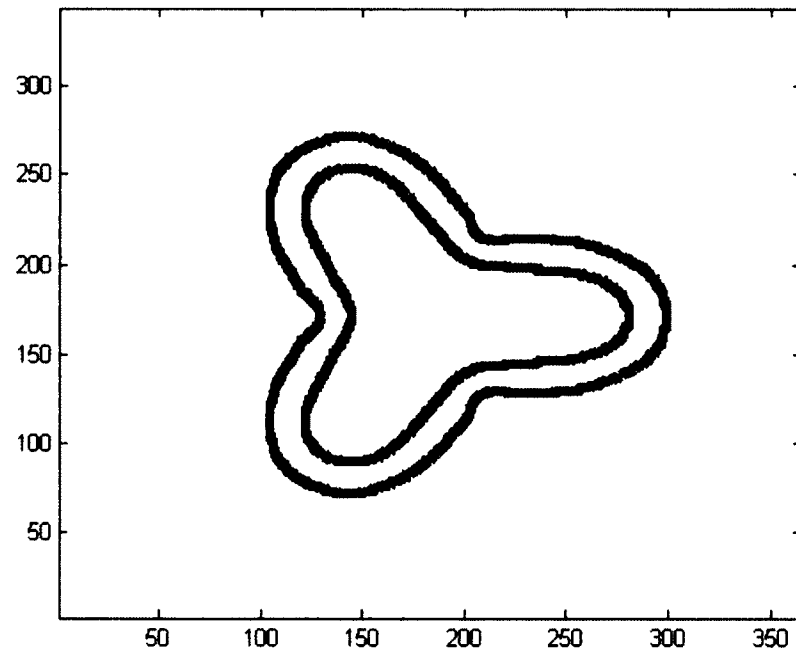


**Figure 5-8:** The level set lines of the flower shape.

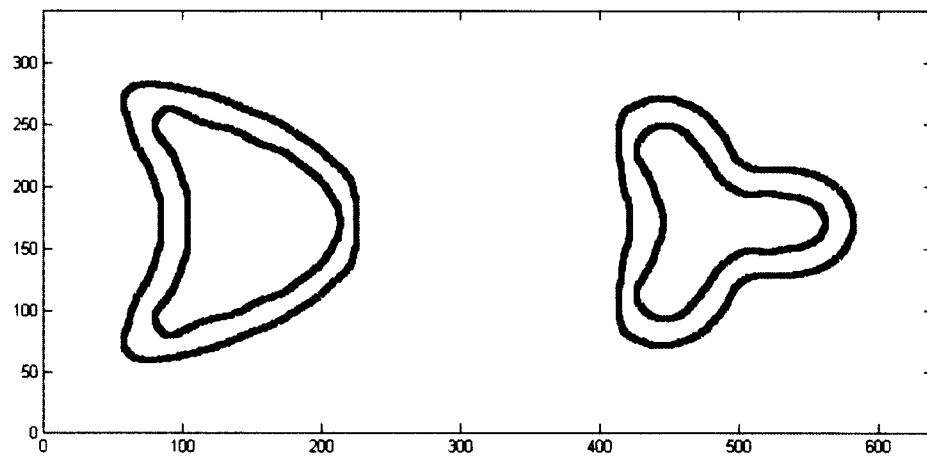


**Figure 5-9:** The level set lines of the two objects shape.

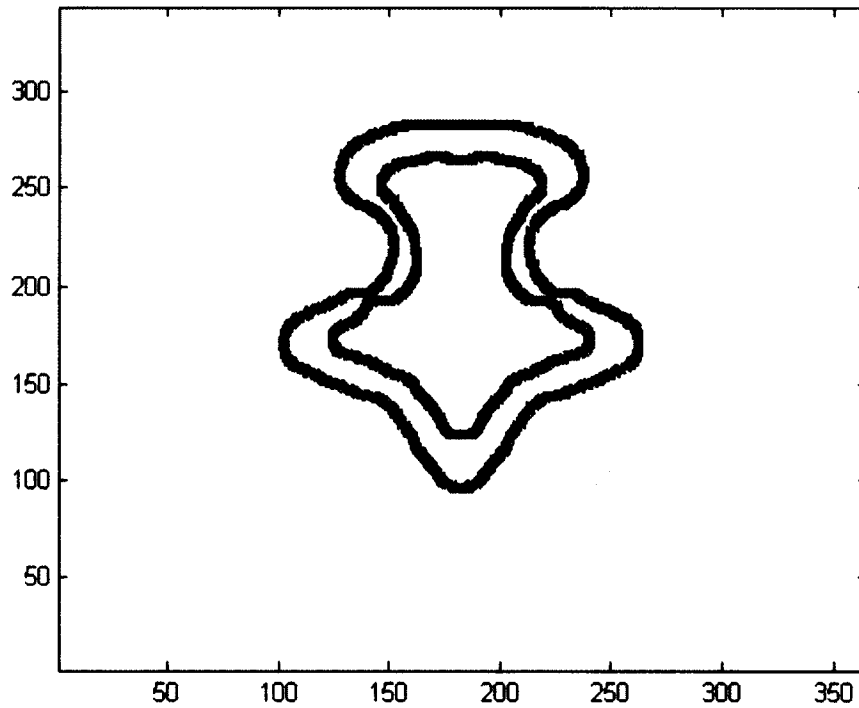


**Figure 5-10:** The level set lines of the plane shape.

We want to use the level set data to create figures to see if the MUSIC algorithm is robust and improve the MUSIC algorithm. So we collect level set data [36] from the kite-shape, flower-shape, teardrop-shape, two-object-shape and plane-shape by using the active contour method. For the star-like shape, we take the flower shape case as an example (see **Figure 5-11**).

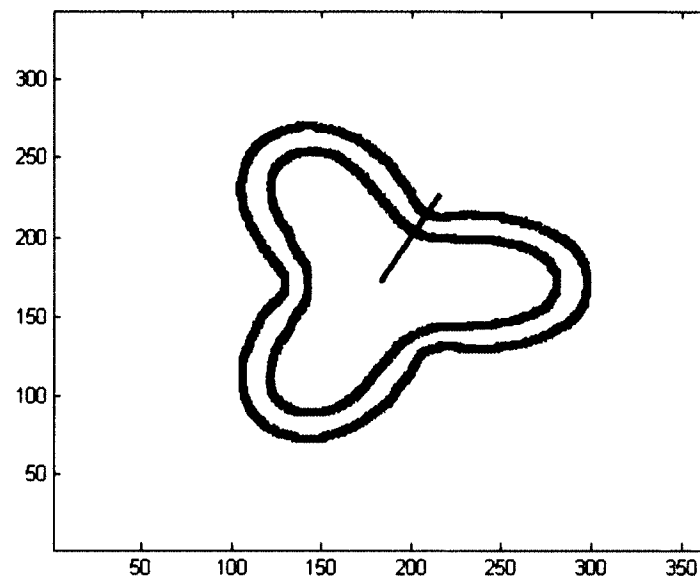


**Figure 5-11:** Obtain points for star-like shape.

Since the ACWE method can detect the edges, we can see that each target corresponds to two edges in the reconstruction combining the multiple frequency MUSIC algorithm and the multi-tone algorithm: one inside and one outside. The artificial lines have been suppressed and would not bother the ACWE method. We would expect the ACWE method to generate two level set curves, one inside and one outside the target. The reason is that for all the plots of imaging functions, for each target there is a sharp gradient curve (edge) outside and a sharp gradient curve (edge) inside. The ACWE method detects edges. The average of the two curves is expected to be a good result for shape reconstruction. Our next step is to propose a systematic way to do the averaging.

For the star-like shape (**Figure 5-11**), we first set a point in the middle of the figure, then make radials from the center point in different directions to make sure each direction meets exactly two points, one on each of the two level set curves. Then we can

collect the midpoints of such pairs, making an average shape of the two level set curves to compare with the original shape of the target(s).

For other kinds of shapes (see **Figure 5-12**), this method is not proper, because the intersection points may be more than two points. However, we know the level set data of the shapes. For the points which are from the interior, we find the points which are the shortest distance from each exterior point. For the points which are from the exterior, we find the points which are the shortest distance from each interior point. Finally, we have all the points we need, and we create the shapes by connecting the pairs of points and find the midpoint of each pair. The collection of the midpoints forms the average shape to be compared with the original shape of the target(s).

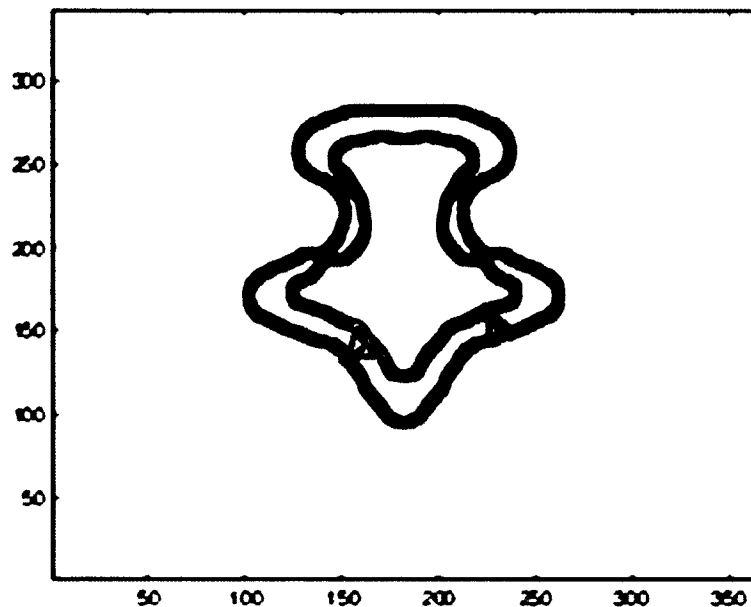


**Figure 5-12:** Obtain points for non-star-like shape.

We remap the level-set data to the figures of the original shape of the targets, and we obtain the coordinates of the level-set data (See **Figure 5-13 - Figure 5-17**).

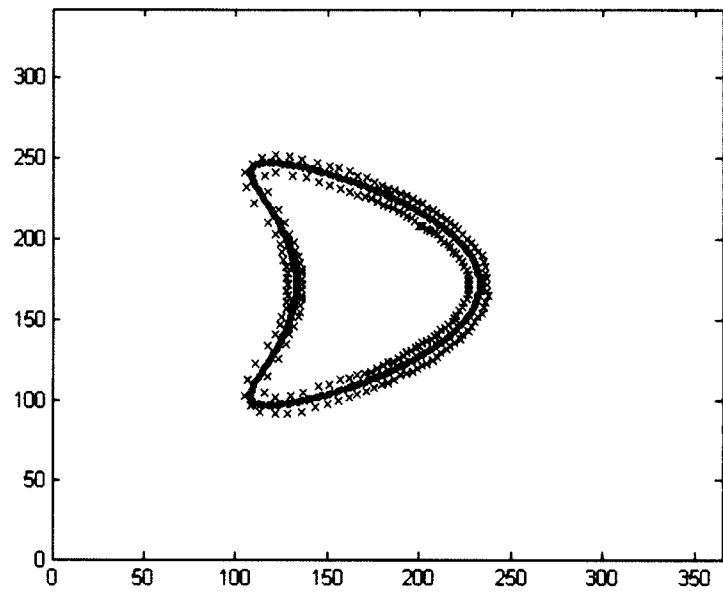


**Figure 5-13:** Compare the active contour method to the original shape of the kite.

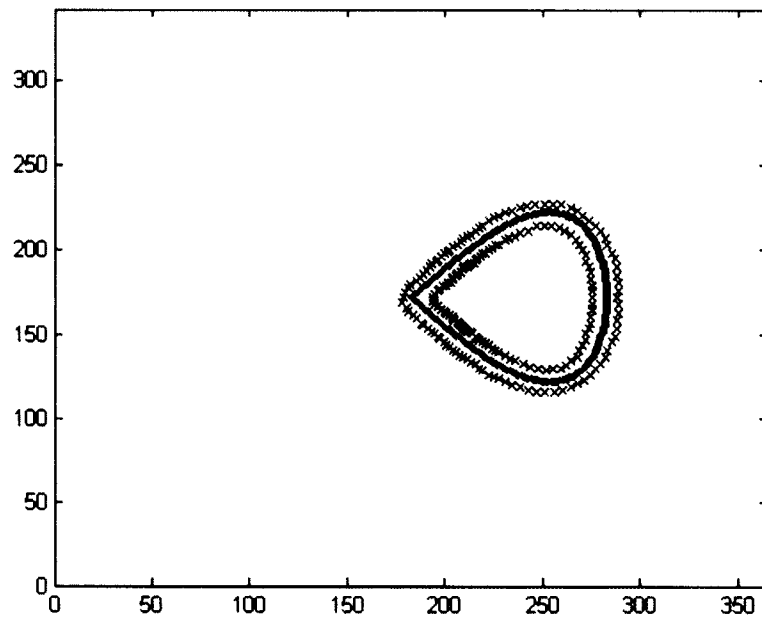


**Figure 5-14:** Compare the active contour method to the original shape of the teardrop.

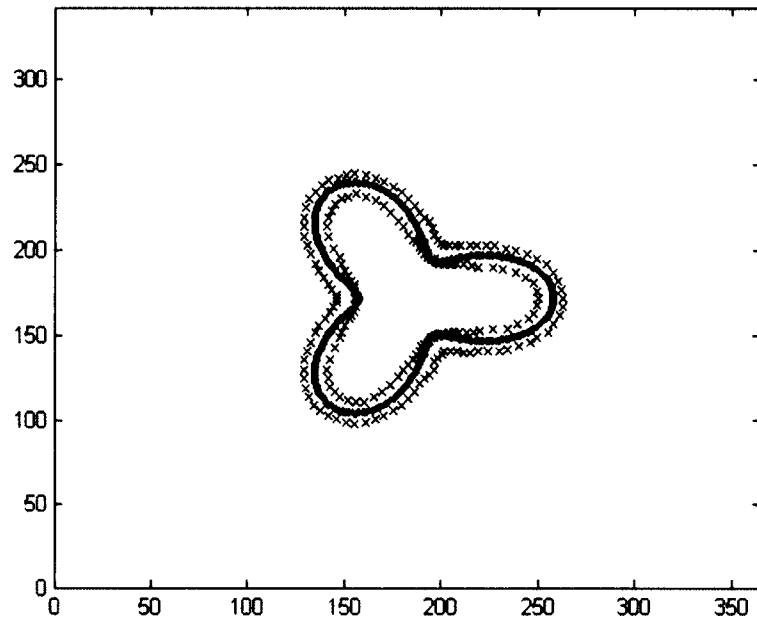


**Figure 5-15:** Compare the active contour method to the original shape of the flower.

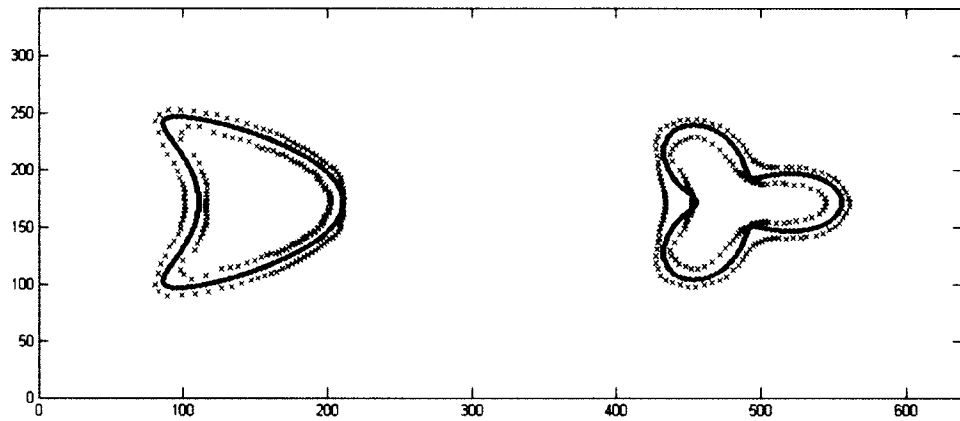


**Figure 5-16:** Compare the active contour method to the original shape of the two objects.

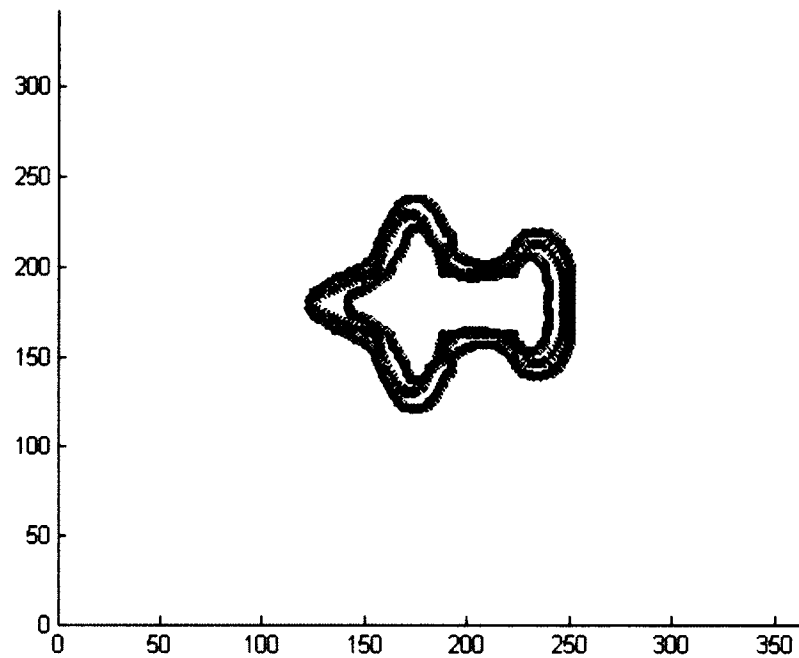


**Figure 5-17:** Compare the active contour method to the original shape of the plane.

Finally, we have all the points we need, and we create the shapes by connecting the pairs of points and find the midpoint of each pair. The collection of the midpoints is to be compared with the original shape of the targets (See **Figure 5-18 - Figure 5-22**).

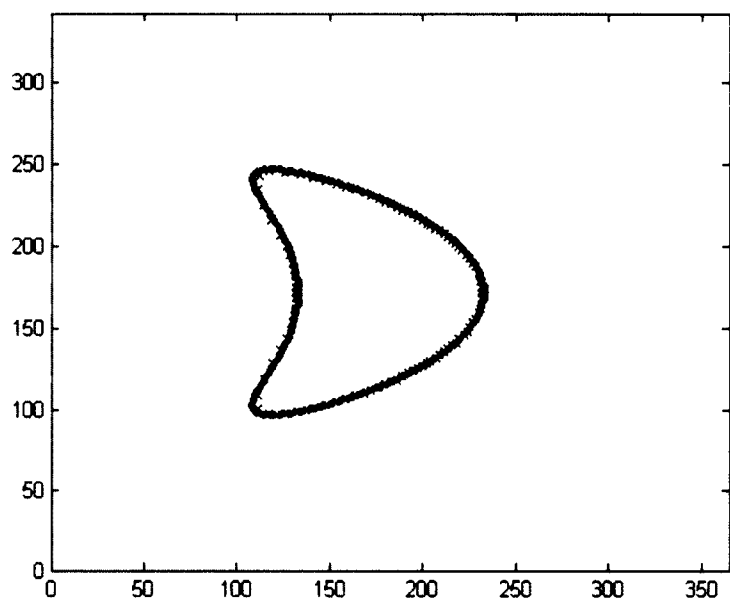


**Figure 5-18:** Compare the averaged active contour method to the original shape of the kite.

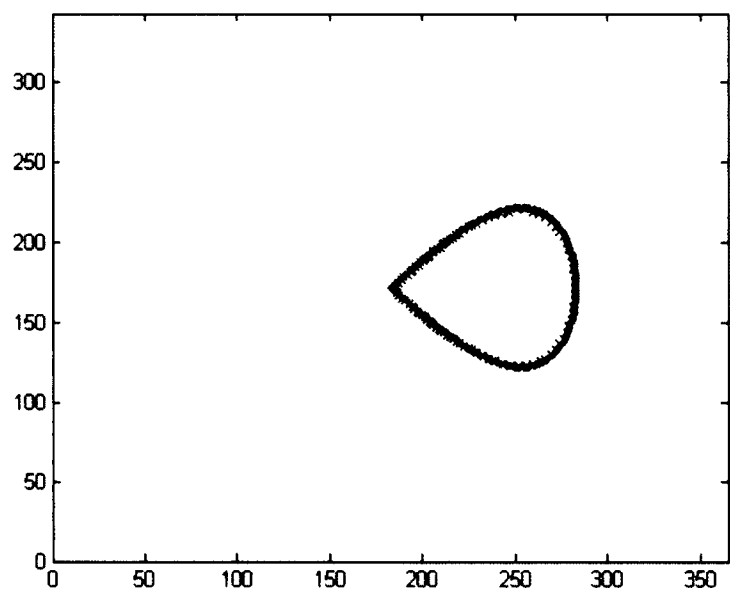


**Figure 5-19:** Compare the averaged active contour method to the original shape of the teardrop.

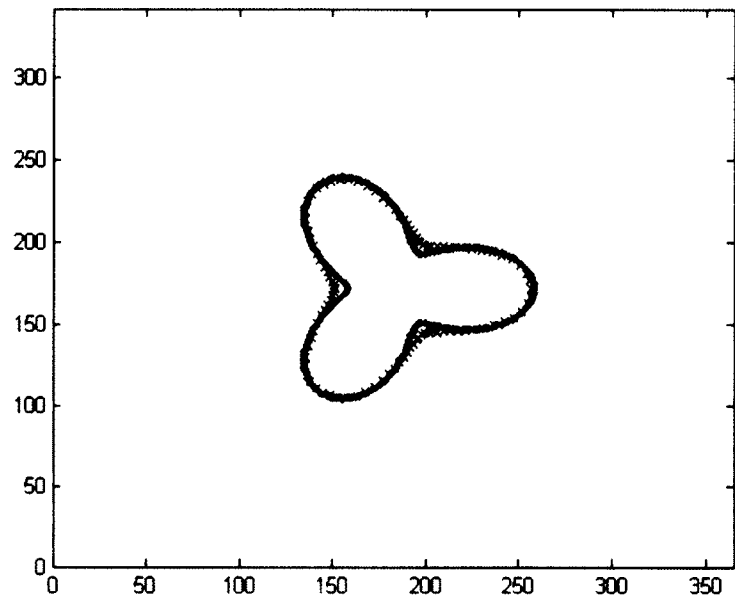


**Figure 5-20:** Compare the averaged active contour method to the original shape of the flower.

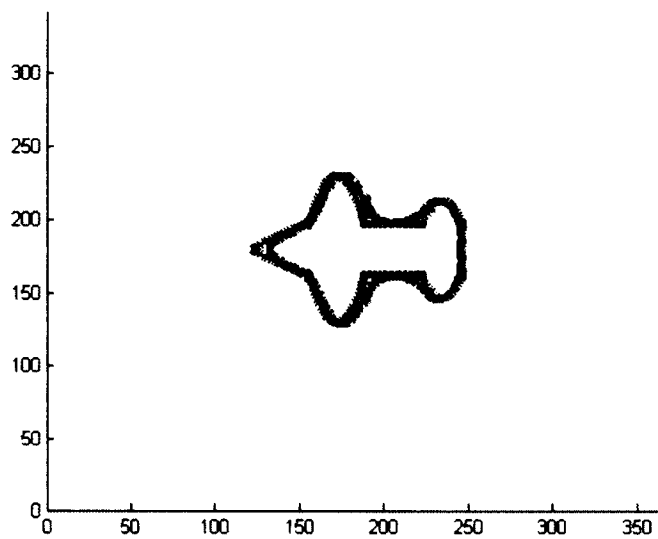


**Figure 5-21:** Compare the averaged active contour method to the original shape of the plane.

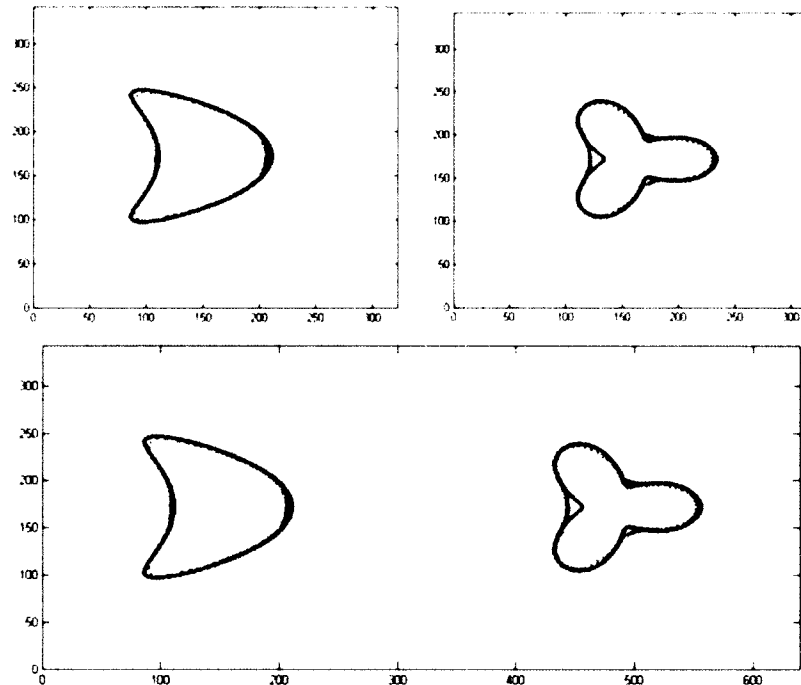


**Figure 5-22:** Compare the averaged active contour method to the original shape of the two objects.

In **Figure 5-13**, **Figure 5-14**, **Figure 5-15**, **Figure 5-16** and **Figure 5-17**, we post the figures that include level-set lines and original lines. The black and blue parts are the shape of the target which is created by level-set data, and the red part is the original shape of the target. In **Figure 5-18**, **Figure 5-19**, **Figure 5-20**, **Figure 5-21** and **Figure 5-22**, after taking the average of the level set data, we want to compare the average shape of the target to the original one. The red parts are the original shapes of the target, and the black parts are the shapes of the target after taking the average by the active contour method.

According to the numerical experiments above, we could see that if the target is smooth or has few corners, the shape of the target by the active contour method is very close to the original shape. The result of the target with multiple corners and more targets

in one plane is not good enough. However, the active contour method still improves the MUSIC algorithm.

#### 5.4 Dealing with the Noise

In real applications, there is always noise, such as the measurement noise. However, sometimes we cannot obtain the exact form of the background of Green's function because there may exist some inhomogeneity in the background medium. We need to assume a form of the measured field at the array under the Dirichlet boundary condition. Now we introduce the response matrix with measurement noise in the Dirichlet boundary condition [19], that is, the real and imaginary parts of  $P_{ij}$  are perturbed (see Eq. 5-28 - Eq. 5-30).

$$P_{ij} = P_{ij\_real} + i * P_{ij\_imag}, \quad \text{Eq. 5-28}$$

$$P_{ij\_real\_with\_noise} = P_{ij\_real} * (1 + s_{ij}), \quad \text{Eq. 5-29}$$

$$P_{ij\_imag\_with\_noise} = P_{ij\_imag} * (1 + t_{ij}), \quad \text{Eq. 5-30}$$

where  $s_{ij}$  and  $t_{ij}$  are uniformly distributed between  $-a\% \sim a\%$ . We choose  $a = 100$  here, which means we add 100% noise to the response matrix.

We want to show the comparison after we add noise the response matrix to see if the MUSIC algorithm and the active contour method are still accurate. We add 100% noise to the response matrix of the kite-shape, the teardrop-shape, the flower-shape, the two-object-shape, and the plane-shape. To be precise, the real and imaginary parts of each element of the response matrix are perturbed using a uniform distribution with 100% error. Parameters for adding noise are the same as in Section 5.3. We follow the procedures of the flow chat (see **Figure 1-2**) and obtain the numerical results with 100% noise. The red parts in **Figure 5-23**, **Figure 5-24**, **Figure 5-25**, **Figure 5-26**, and **Figure**

5-27 are the original shape of the target, and the black parts are the shape of the target after taking the average by the active contour method. The results show our method is robust with respect to noisy data. The robustness is due to the use of singular value decomposition. Mirsky [49] proved a singular value perturbation result that for a matrix  $A$  and a perturbation matrix  $E$  (see Eq. 5-31)

$$\text{Max}_i |\sigma_i(A + E) - \sigma_i(A)| \leq \|E\|_2, \quad \text{for } i = 1, 2, 3 \dots, m, \quad \text{Eq. 5-31}$$

where  $\sigma_i$  means the  $i$ th singular value. In other words, the maximum absolute error of the singular value perturbation cannot exceed the 2-norm of the perturbation matrix. This explains that singular values are robust. We used SVD in our imaging functions. We could understand our robust results as a consequence of the robustness of singular values, though the rigorous proof of the robustness of our result is an extremely challenging open problem.

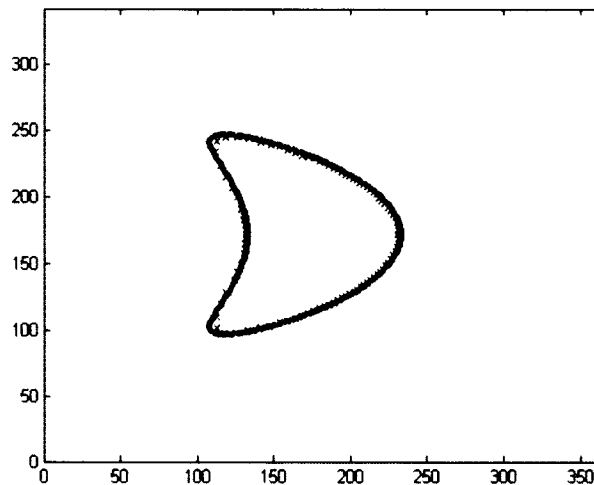


**Figure 5-23:** Compare the averaged active contour method to the original shape of the kite with 100% noise.

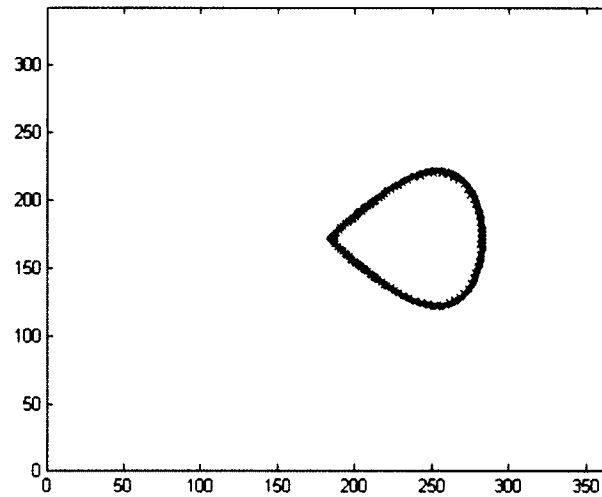


**Figure 5-24:** Compare the averaged active contour method to the original shape of the teardrop with 100% noise.

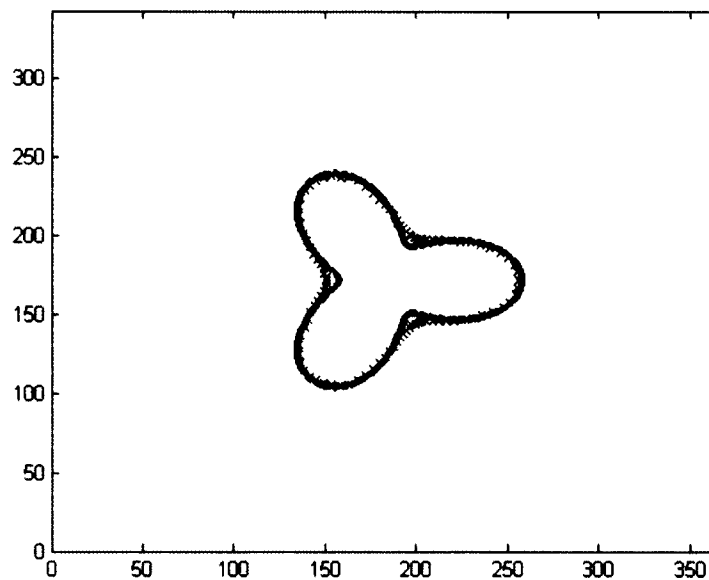


**Figure 5-25:** Compare the averaged active contour method to the original shape of the flower with 100% noise.

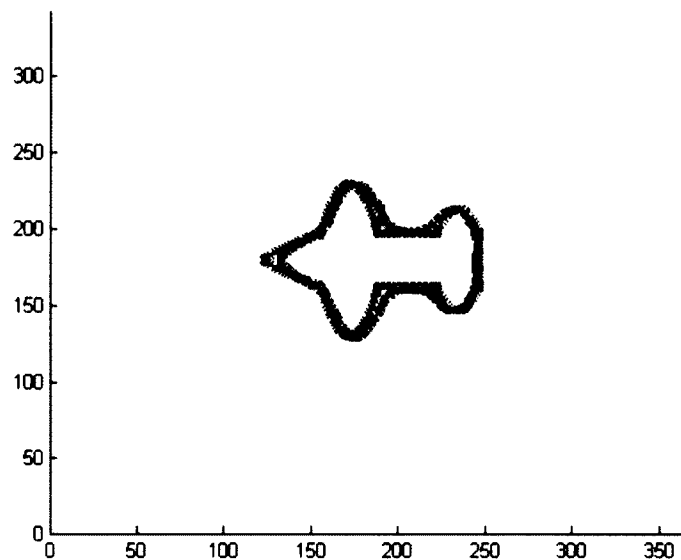


**Figure 5-26:** Compare the averaged active contour method to the original shape of the plane with 100% noise.

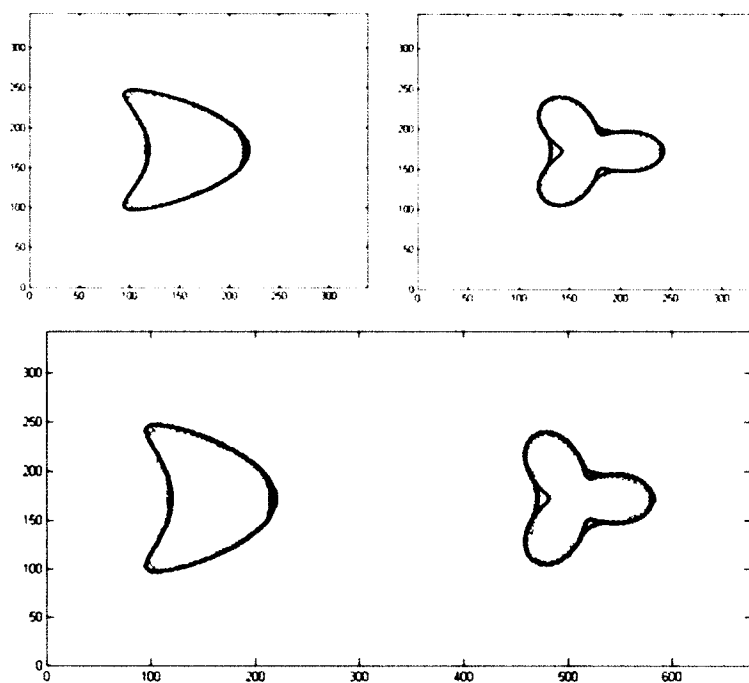


**Figure 5-27:** Compare the averaged active contour method to the original shape of the two-object with 100% noise.

From the **Figure 5-23 - Figure 5-27**, we can observe that, even when we add the 100% noise to the response matrix, the images of adding noise is still close to the non-noise images, which proves the robustness of the MUSIC algorithm.

## 5.5 Numerical Analysis

From the numerical results we obtained by using the active contour method, we observe that they are close to the original shape of the targets. We set a center point, then find a pair of points in each direction to calculate the error.

By observation, we find that the kite and teardrop cases have the best result, and the plane-shape case is not very close to the original shape of the target.

We calculate the distance between each pair of the points so we could calculate the error of the entire shape. This method (single linkage method) [50] to calculate the numerical error is much easier, compared to partial shape matching method based on the Smith-Waterman algorithm [51], IS-match (integral shape match) [52] and MCMC (Markov chain Monte Carlo) based algorithm [53]. All the methods in the references use quite advanced techniques while we simply compare the relative errors for different angles. Our cost is  $O(m)$ , where  $m$  is the number of angles. It is a simply way to quantitatively measure the error of a shape. Here, we show how we compute the 2-norm error and the  $\infty$ -norm error as **Eq. 5-32** and **Eq. 5-33**

$$2 - norm\ error = \frac{\sqrt{\sum d_i^2}}{D}, \quad \text{Eq. 5-32}$$

$$\infty - norm\ error = \frac{\max|d_i|}{D}, \quad \text{Eq. 5-33}$$

where  $d_i$  is the  $i$ th distance of two point in one direction, and  $D$ , which is called the diameter, is the longest distance of two points on the boundary of the targets.

The error analysis is shown in **Table 5-1** and **Table 5-2**.

**Table 5-1:** Numerical analysis for the cases without noise.

	$2 - norm\ error$	$\infty - norm\ error$
Kite shape case	1.06%	1.88%
Teardrop case	1.23%	2.34%
Flower case	0.86%	1.39%
Two objects case	3.65%	4.58%
Plane shape case	3.67%	5.0%

Then we post the numerical analysis for the cases with noise.

**Table 5-2:** Numerical analysis for the cases with 100% noise.

	$2 - norm\ error$	$\infty - norm\ error$
Kite shape case	1.05%	1.72%
Teardrop case	1.17%	1.74%
Flower case	0.86%	1.39%
Two objects case	3.7%	4.64%
Plane shape case	3.67%	5.0%

We simply explain how we do the numerical analysis. For the star-like shape case, we do the same when we find the level-set data to create the shape of the targets (see **Figure 5-12**). For the non-star-like shape case (see **Figure 5-28**), we divide the shape into parts, fix the center of each part, then make the radius in different directions to

meet two points: one belongs to the numerical results and the other one belongs to the original shape of the target.

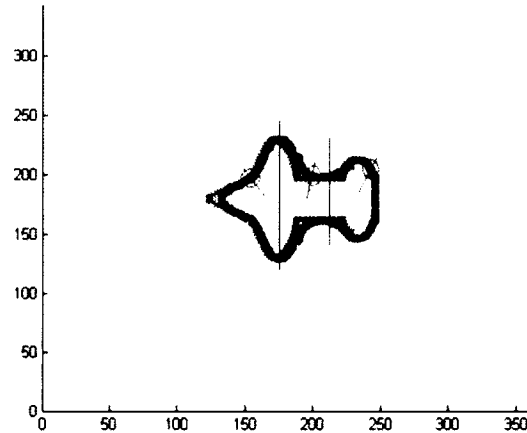


**Figure 5-28:** Method for doing numerical analysis for non-star-like shape.

### 5.6 Summary for the Active Contour Method

When we obtain the images of the unknown targets by using the MUSIC algorithm, it is hard to find the exact object because the artificial lines always come with the numerical results. After we use the active method, we could obtain better results, even from the multiple corners case and the multiple-object case. By the error analysis, we know that if the unknown targets are simple, the numerical results are very close to the original shape of the targets.

## CHAPTER 6

### CONCLUSIONS AND FUTURE WORK

#### 6.1 Conclusions

In this dissertation, we propose the signal space method to show we cannot avoid artificial lines for the MUSIC imaging function, even if we do not use the response matrix. However, we could reduce the effect from artificial lines by summing multiple frequencies from the MUSIC and the multi-tone methods, and get a better shape of the targets. In order to improve the imaging results, we apply the active contour method. After using this method, we could easily obtain the shape of the targets. It is clear that extensive numerical experiments demonstrate the effectiveness of our proposed method, even with the presence of 100% noise to the elements of the response matrix. The improved imaging method (see **Figure 1-2**), is accurate and robust, comparing to the direct imaging methods. We eliminate the artificial lines by applying the improved imaging method and obtain the numerical results which are very close to the original shape of the targets. Also, compared to the iterative method, the improved imaging method cost less because when we use the iterative method, it is needed to solve the forward solver in each iteration. Recall we have a flow chart **Figure 1-2**. The computational complexity of my overall algorithm including the forward problem is  $O(Nn^3)$ , where  $N$  is the number of transducers when we solve the forward problem. The

reason is as follows: for each incident wave angle, we need to solve the linear system, see **Eq. 2-41**, and the computational complexity of the system is  $O(n^3)$ . There are  $N$  angles (transducers) when we solve the forward problem. Further, it is the forward problem part that costs the most.

## 6.2 Future Work

In this dissertation, all the numerical results are in the Dirichlet boundary condition. There are two main reasons why we cannot apply the improved method to the case in the Neumann boundary condition. One is that when we solve the forward and inverse problem, it costs much more time compared to the case in the Dirichlet boundary condition. The other one is that we cannot obtain good numerical results from the corner case, flower-case and the two-object-case, even after we use the multi-tone method (See **Figure 6-1**, **Figure 6-2**, **Figure 6-3** and **Figure 6-4**), in which we apply the method in **Section 2.2**, and compare these four figures to **Figure 3-3**, **Figure 3-4**, **Figure 3-5** and **Figure 3-6**. By comparison, we find the numerical results with the Neumann boundary condition are not as good as the numerical results with the Dirichlet boundary condition because there are more artificial lines and the exact shape is disguised. Even with human's eyes the targets in these figures are harder to identify. Multiple frequency approach cannot help to clean most artificial lines. The ACWE is unable to capture the exact shape with so many artifacts, which means it is hard to apply the improved imaging method to the numerical results with the Neumann boundary condition.

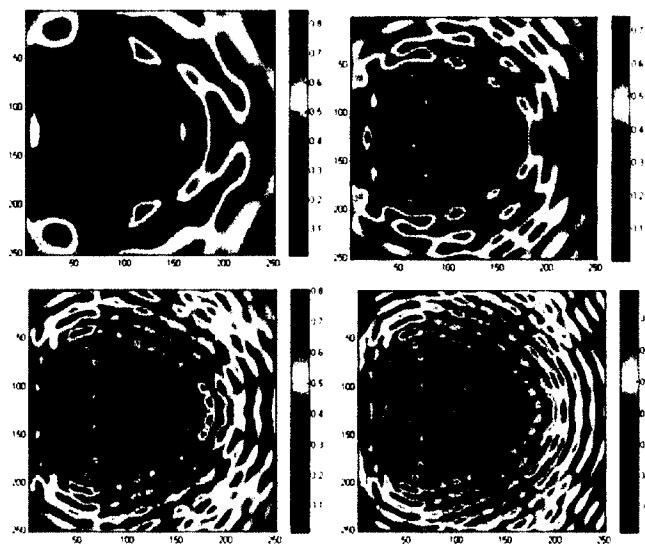


**Figure 6-1:** MUSIC: kite-shape in four different frequencies with the Neumann boundary condition.

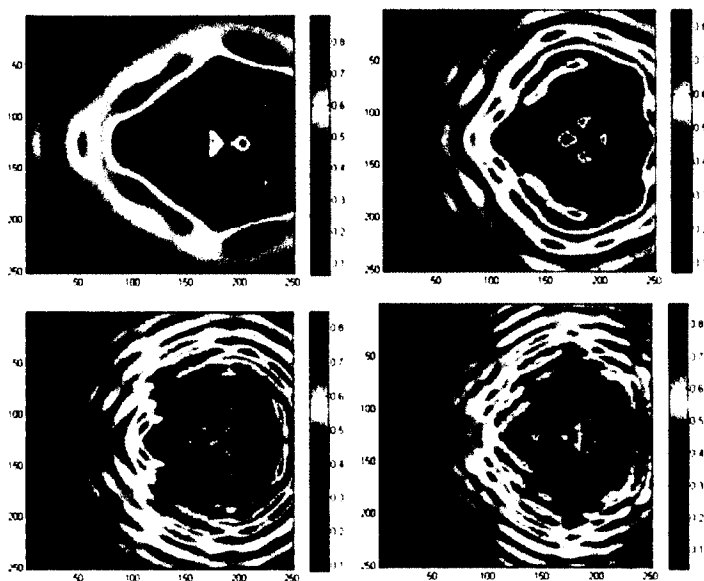


**Figure 6-2:** MUSIC: teardrop-shape in four different frequencies with the Neumann boundary condition.

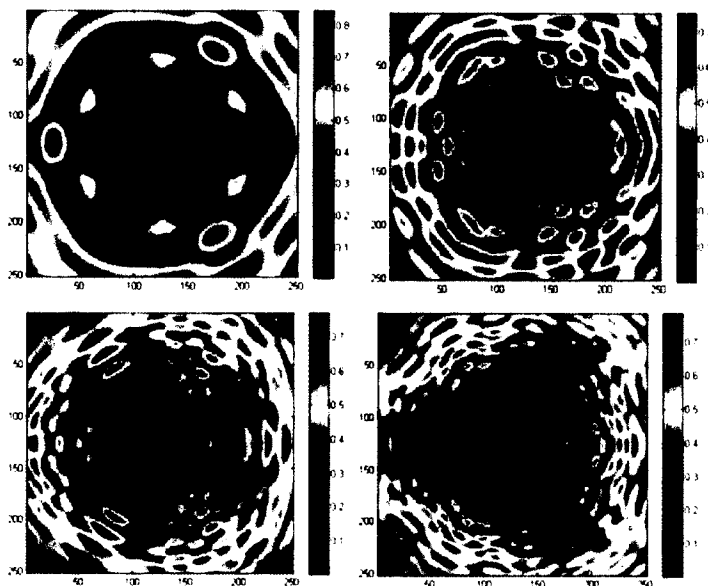


**Figure 6-3:** MUSIC: flower-shape in four different frequencies with the Neumann boundary condition.

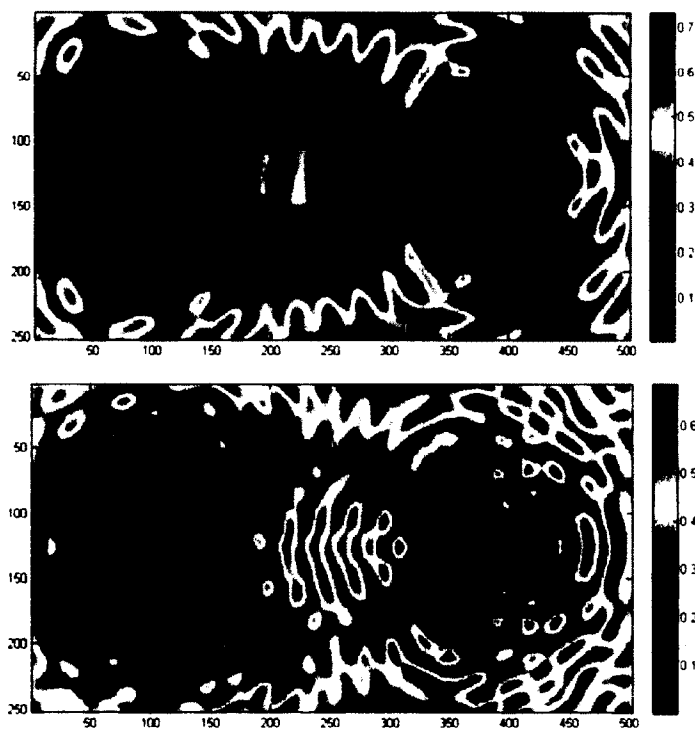


**Figure 6-4:** MUSIC: two-object-shape in two different frequencies with the Neumann boundary condition.

Our next purpose is to find a better algorithm to decrease the implementation time, and improve the direct imaging function to obtain better numerical results. After we have better results, we could apply the multi-tone and the active contour method to them, which are with the Neumann boundary condition.

## APPENDIX

### IMPORTANT FUNCTIONS AND LIBRARY

A. Forward problem for smooth case.m

```

syms y
x1_=cos(y)+0.65*cos(2*y)-0.65;
x2_=1.5*sin(y);
x1dp=diff(x1_);
x2dp=diff(x2_);
x1ddp=diff(x1_,2);
x2ddp=diff(x2_,2);
n=32;
C=0.57721566490153286060651209;
ntrs=64;

for p=1:1:2*n
    tp=pi*(p-1)/n ;
    x1(p)=subs(x1_, tp);
    x2(p)=subs(x2_, tp);
    x1d(p)=subs(x1dp, tp);
    x2d(p)=subs(x2dp,tp);
    x1dd(p)=subs(x1ddp, tp);
    x2dd(p)=subs(x2ddp,tp);
end
K=zeros(2*n,2*n);
for k=4:1:12
for tran1=1:1:ntrs

```

```

tran1
theta1=2*pi*tran1/ntrs;
d=[cos(theta1),sin(theta1)];
for t=1:1:2*n
for j=1:1:2*n
S=0;
for mm=1:1:n-1;
S=S+(1/mm)*cos((mm*pi*abs(t-j))/n);
end
R=(-2*pi/n)*S-(((1)^abs(t-j))*pi)/(n^2);
if t==j
c=abs(x1d(t)^2+x2d(t)^2);
l1(t,j)=0;
l2(t,j)=(1/(2*pi))*(x1d(t)*x2dd(t)-x2d(t)*x1dd(t))/c;
m1(t,j)=(-1/(2*pi))*besselj(0,k*abs(((x1(t)-x1(j))^2+(x2(t)-
x2(j))^2))^0.5)*abs(((x1d(j))^2+(x2d(j))^2)^0.5);
m2(t,j)=(1i/2-C/pi-
(log(k*abs((x1d(t)^2+x2d(t)^2)^0.5)/2))/pi)*abs((x1d(t)^2+x2d(t)^2)^0.5);
K(t,j)=R*(l1(t,j)+1i*k*m1(t,j))+(pi/n)*(l2(t,j)+1i*k*m2(t,j));
else
u=log(4*(sin((pi*(t-1)/n-pi*(j-1)/n)/2))^2);
l(t,j)=(1i*k/2)*(x2d(j)*(x1(j)-x1(t))-x1d(j)*(x2(j)-
x2(t)))*besselh(1,1,k*abs(((x1(t)-x1(j))^2+(x2(t)-x2(j))^2))^0.5)/abs(((x1(t)-
x1(j))^2+(x2(t)-x2(j))^2)^0.5);
l1(t,j)=(k/(2*pi))*(x2d(j)*(x1(t)-x1(j))-x1d(j)*(x2(t)-
x2(j)))*besselj(1,k*abs(((x1(t)-x1(j))^2+(x2(t)-x2(j))^2))^0.5)/abs(((x1(t)-
x1(j))^2+(x2(t)-x2(j))^2)^0.5);
l2(t,j)=l(t,j)-l1(t,j)*u;
m(t,j)=(1i/2)*besselh(0,1,k*abs(((x1(t)-x1(j))^2+(x2(t)-
x2(j))^2))^0.5)*abs(((x1d(j))^2+(x2d(j))^2)^0.5);

```

```

        m1(t,j)=(-1/(2*pi))*besselj(0,k*abs(((x1(t)-x1(j))^2+(x2(t)-
x2(j))^2))^0.5)*abs(((x1d(j))^2+(x2d(j))^2)^0.5);
        m2(t,j)=m(t,j)-m1(t,j)*u;
        K(t,j)=R*(l1(t,j)+1i*k*m1(t,j))+(pi/n)*(l2(t,j)+1i*k*m2(t,j));
    end
end
x=[x1(t), x2(t)];
g(t)=-2*exp(1i*k*dot(x,d));
end
A=(eye(2*n)-K)g.';
for t=1:1:2*n
miu1(t)=x2d(t)/sqrt(x1d(t)^2+x2d(t)^2);
miu2(t)=-x1d(t)/sqrt(x1d(t)^2+x2d(t)^2);
end
for tran2=1:1:ntrs
    theta2=2*pi*tran2/ntrs+pi;
    xhat=[cos(theta2),sin(theta2)];
sum=0;
for t=1:1:2*n
Z(t)=(k*(miu1(t)*xhat(1)+miu2(t)*xhat(2))+k)*exp(-
1i*k*(xhat(1)*x1(t)+xhat(2)*x2(t)))*A(t)*sqrt(x1d(t)^2+x2d(t)^2);
sum=sum+Z(t);
end
U(tran1,tran2,k-3)=exp(-1i*pi/4)/sqrt(8*pi*k)*pi/n*sum;
end
end
end

```

B. Forward problem for corner case.m

n=32;

P=8;

```

C=0.57721566490153286060651209;
ntrs=64;
syms y
x1_ =2*sin(y/2);
x2_ =-sin(y);
x3_ =(1/P-1/2)*(1-y/pi)^3+(y-pi)/P/pi+1/2;
x4_ =(2*pi*x3_^P)/(x3_^P+((1/P-1/2)*(-1+y/pi)^3+(-y+pi)/P/pi+1/2)^P);
x1dp=diff(x1_,y,1);
x2dp=diff(x2_,y,1);
x1ddp=diff(x1_,y,2);
x2ddp=diff(x2_,y,2);
wdp=diff(x4_,y,1);
for p=1:1:2*n
    s(p)=pi*(p-1)/n ;
vs(p)=(1/P-1/2)*(1-s(p)/pi)^3+(s(p)-pi)/P/pi+1/2;
ws(p)=(2*pi*vs(p)^P)/(vs(p)^P+((1/P-1/2)*(-1+s(p)/pi)^3+(-
s(p)+pi)/P/pi+1/2)^P);
x1(p)=subs(x1_, ws(p));
x2(p)=subs(x2_, ws(p));
x1d(p)=subs(x1dp, ws(p));
x2d(p)=subs(x2dp,ws(p));
x1dd(p)=subs(x1ddp, ws(p));
x2dd(p)=subs(x2ddp,ws(p));
wd(p)=subs(wdp,s(p));
end
K1=zeros(2*n,2*n);
for k=4:1:12
    yita=k;
for tran1=1:1:ntrs
    tran1
    theta1=2*pi*tran1/ntrs;

```

```

d=[cos(theta1),sin(theta1)];
for t=1:1:2*n
  for j=2:1:2*n
    S=0;
    for mm=1:1:n-1;
      S=S+(1/mm)*cos((mm*pi*abs(t-j))/n);
    end
    R=(-2*pi/n)*S-((-1)^abs(t-j))*pi/(n^2);
    if t==j
      c=abs(x1d(t)^2+x2d(t)^2);
      u=log(4*(sin((ws(t)-ws(j))/2)^2));
      l1(t,j)=0;
      l2(t,j)=(1/(2*pi))* (x1d(t)*x2dd(t)-x2d(t)*x1dd(t))/c;
      m1(t,j)=(-1/(2*pi))*besselj(0,k*abs(((x1(t)-x1(j))^2+(x2(t)-
x2(j))^2))^0.5)*abs(((x1d(j))^2+(x2d(j))^2)^0.5);
      m2(t,j)=(1i/2-C/pi-(log(k*abs(c^0.5)/2))/pi)*abs(c^0.5);
      H(t,j)=(x2d(t)*x1dd(t)-x1d(t)*x2dd(t))/pi/c;
      H(t,j)=H(t,j)/2;
      K1(t,j)=(R*(l1(t,j)+1i*yita*m1(t,j))+(pi/n)*((l2(t,j)+1i*yita*m2(t,j))+2*log(w
d(t))*(l1(t,j)+1i*yita*m1(t,j))))*wd(j);
    else
      u=log(4*(sin((ws(t)-ws(j))/2)^2));
      l(t,j)=(1i*k/2)*(x2d(j)*(x1(j)-x1(t))-x1d(j)*(x2(j)-
x2(t)))*besselh(1,1,k*abs(((x1(t)-x1(j))^2+(x2(t)-x2(j))^2))^0.5)/abs(((x1(t)-
x1(j))^2+(x2(t)-x2(j))^2)^0.5);
      l1(t,j)=(k/(2*pi))*(x2d(j)*(x1(t)-x1(j))-x1d(j)*(x2(t)-
x2(j)))*besselj(1,k*abs(((x1(t)-x1(j))^2+(x2(t)-x2(j))^2))^0.5)/abs(((x1(t)-
x1(j))^2+(x2(t)-x2(j))^2)^0.5);
      l2(t,j)=l(t,j)-l1(t,j)*u;
      m(t,j)=(1i/2)*besselh(0,1,k*abs(((x1(t)-x1(j))^2+(x2(t)-
x2(j))^2))^0.5)*abs(((x1d(j))^2+(x2d(j))^2)^0.5);

```

```

        m1(t,j)=(-1/(2*pi))*besselj(0,k*abs(((x1(t)-x1(j))^2+(x2(t)-
x2(j))^2))^0.5)*abs(((x1d(j))^2+(x2d(j))^2)^0.5);
        m2(t,j)=m(t,j)-m1(t,j)*u;
        H(t,j)=(x2d(j)*(x1(t)-x1(j))-x1d(j)*(x2(t)-x2(j)))/pi/((x1(t)-
x1(j))^2+(x2(t)-x2(j))^2);
        K1(t,j)=(R*(l1(t,j)+1i*k*m1(t,j))+(pi/n)*((l1(t,j)+1i*yita*m1(t,j))*u+l2(t,j)+1
i*yita*m2(t,j)-(l1(t,j)+1i*yita*m1(t,j))*log(4*(sin((s(t)-s(j))/2))^2)))*wd(j);
        end
        K1(t,j)=-K1(t,j);
end
    sum1=0;
    for nn=1:1:2*n-1
        sum1=sum1+pi/n*H(t,nn)*wd(1,nn);
    end
    T(t,1)=sum1;
    x=[x1(t), x2(t)];
    g(t)=-2*exp(1i*k*dot(x,d));
end
K2=zeros(2*n,2*n);
    K3=eye(2*n);
    K1=K3+K1;
    K1(:,1)=-1-T(:,1);
    K1(1,1)=-T(1,1);
    A=K1\g;
for t=1:1:2*n
    miu1(t)=x2d(t)/sqrt(x1d(t)^2+x2d(t)^2);
    miu2(t)=-x1d(t)/sqrt(x1d(t)^2+x2d(t)^2);
end
for tran2=1:1:ntrs
    theta2=2*pi*tran2/ntrs+pi;
    xhat=[cos(theta2),sin(theta2)];

```

```

sum=0;
    for t=1:1:2*n
Z(t)=((k*(miu1(t)*xhat(1)+miu2(t)*xhat(2))+k)*exp(-
1i*k*(xhat(1)*x1(t)+xhat(2)*x2(t)))*A(t)*sqrt(x1d(t)^2+x2d(t)^2))*wd(t);
sum=sum+Z(t);
    end
    UU(tran1,tran2,k-3)=exp(-1i*pi/4)/sqrt(8*pi*k)*pi/n*sum;
end
end
end
end

```

### C. Forward problem with NBC.m

```

n=32;
    ntrs=64;
    C=0.57721566490153286060651209;
syms y
    x1_=cos(y)+0.65*cos(2*y)-0.65;
x2_=1.5*sin(y);
    x1dp=diff(x1_,y,1);
x2dp=diff(x2_,y,1);
x1ddp=diff(x1_,y,2);
x2ddp=diff(x2_,y,2);
x1dddp=diff(x1_,y,3);
x2dddp=diff(x2_,y,3);
    for p=1:1:2*n
        tp=pi*(p-1)/n ;
        x1(p)=subs(x1_, tp);
        x2(p)=subs(x2_, tp);
x1d(p)=subs(x1dp, tp);
x2d(p)=subs(x2dp,tp);
x1dd(p)=subs(x1ddp, tp);

```

```

x2dd(p)=subs(x2ddp,tp);
x1ddd(p)=subs(x1dddp,tp);
x2ddd(p)=subs(x2dddp,tp);
end
for t=1:1:2*n
miu1(t)=x2d(t)/sqrt(x1d(t)^2+x2d(t)^2);
miu2(t)=-x1d(t)/sqrt(x1d(t)^2+x2d(t)^2);
end
K=zeros(2*n,2*n);
for k1=1:1:5
    k=k1/2;
    yita=k;
    for tran1=1:1:ntrs
        tran1
        theta1=2*pi*tran1/ntrs;
        dd=[cos(theta1),sin(theta1)];
    for t=1:1:2*n
        for j=1:1:2*n
            S=0;
            for m=1:1:n-1;
                S=S+(1/m)*cos((m*pi*abs(t-j))/n);
            end
            R=(-2*pi/n)*S-((-1)^abs(t-j))*pi/(n^2);
            if t==j
                a=sqrt(abs(x1d(t)^2+x2d(t)^2));
                b=x2d(t)*x1dd(t)-x1d(t)*x2dd(t);
                c=x1d(t)*x1d(j)+x2d(t)*x2d(j);
                n1(t,j)=-(k^2)*(a^2)/4/pi;
                n2(t,j)=(pi*1i-1-2*C-
2*log(k*a/2))*(k^2*a^2/4/pi)+1/12/pi+((x1d(t)*x1dd(t)+x2d(t)*x2dd(t))^2)/2

```

```

/pi/a^4-(x1dd(t)^2+x2dd(t)^2)/4/pi/a^2-
(x1d(t)*x1ddd(t)+x2d(t)*x2ddd(t))/6/pi/a^2;
    m1(t,j)=-1/(2*pi);
    m2(t,j)=1i/2-C/pi-(log(k*a/2))/pi;
    h1(t,j)=0;
    h2(t,j)=b/(2*pi*a);
    K(t,j)=-n/2+R*(k^2*m1(t,j)*c-n1(t,j)-
1i*yita*h1(t,j))+(pi/n)*(k^2*m2(t,j)*c-n2(t,j)-1i*yita*h2(t,j));
    else
        u=log(4*(sin((pi*(t-1)/n-pi*(j-1)/n)/2))^2);
        c=x1d(t)*x1d(j)+x2d(t)*x2d(j);
        l=(abs(x1d(j)^2+x2d(j)^2))^0.5;
        e=x2d(t)*x1(j)-x2d(t)*x1(t)-x1d(t)*x2(j)+x1d(t)*x2(t);
        d=k*abs(((x1(t)-x1(j))^2+(x2(t)-x2(j))^2))^0.5;
        nw=(x1d(t)*x1(t)-x1d(t)*x1(j)+x2d(t)*x2(t)-
x2d(t)*x2(j))*(x1d(j)*x1(t)-x1d(j)*x1(j)+x2d(j)*x2(t)-x2d(j)*x2(j))/((d/k)^2);
        M(t,j)=(1i/2)*besselh(0,1,d);
        m1(t,j)=(-1/(2*pi))*besselj(0,d);
        m2(t,j)=M(t,j)-m1(t,j)*u;
        N(t,j)=(1i*nw/2)*(k^2*besselh(0,1,d)-
2*k*besselh(1,1,d)/(d/k))+(1i*k*c*besselh(1,1,d)/(2*d/k))+1/(4*pi*(sin((
pi*(t-1)/n-pi*(j-1)/n)/2))^2);
        n1(t,j)=(-nw/(2*pi))*(k^2*besselj(0,d)-2*k*besselj(1,d)/(d/k))-
(k*c*besselj(1,d)/(2*pi*d/k));
        n2(t,j)=N(t,j)-n1(t,j)*u;
        h(t,j)=(1i*k/2)*e*(besselh(1,1,d)/(d/k))*1;
        h1(t,j)=(-k/(2*pi))*e*(besselj(1,d)/(d/k))*1;
        h2(t,j)=h(t,j)-h1(t,j)*u;
        if mod(abs(t-j),2)==0;
            T=0;
        else mod(abs(t-j),2);

```

```

        T=1/(2*n*(sin(abs(t-j)*pi/n/2))^2);
    end
    K1(t,j)= (k^2*m1(t,j)*c-n1(t,j)-1i*yita*h1(t,j));
    K2(t,j)=(k^2*m2(t,j)*c-n2(t,j)-1i*yita*h2(t,j));
    K(t,j)=T+R*K1(t,j)+(pi/n)*K2(t,j);
end
end
x=[x1(t), x2(t)];
f(t)=2*((abs(x1d(t)^2+x2d(t)^2))^0.5)*(-
(1i*k*dd(1)*exp(1i*k*dot(x,dd))*miu1(t)+1i*k*dd(2)*exp(1i*k*dot(x,dd))*
miu2(t));
K(t,t)=K(t,t)+1i*yita*sqrt(x1d(t)^2+x2d(t)^2);
end
A=K\f;
for tran2=1:1:ntrs
    theta2=2*pi*tran2/ntrs+pi;
    xhat=[cos(theta2),sin(theta2)];
    sum=0;
    for t=1:1:2*n
        Z(t)=(k*(miu1(t)*xhat(1)+miu2(t)*xhat(2))+k)*exp(-
        1i*k*(xhat(1)*x1(t)+xhat(2)*x2(t))*A(t)*sqrt(x1d(t)^2+x2d(t)^2);
        sum=sum+Z(t);
    end
    U(tran1,tran2,k^2)=exp(-1i*pi/4)/sqrt(8*pi*k)*pi/n*sum;
end
end
end
end

```

D. Inverse problem for kite case.m

```

x1_m=round(126+x1*50);
x2_m=round(126+x2*50);

```

```

for k1=1:1:5
    k=k1/2;
    UU=U(:, :, 2*k);
    [s,V,D]=svd(UU);
for ii=1:1:251
    ii
        for jj=1:1:251
            xii=(ii-126)/50;
            xjj=(jj-126)/50;
            xy=[xii,xjj];
for trand1=1:1:ntrs
    theta1=2*pi*trand1/ntrs+pi;
    dd=[cos(theta1),sin(theta1)];
    ghat(trand1)=exp(-1i*k*dot(dd,xy));
end
    ghat=ghat/norm(ghat);
    sum_=0;
    for r=1:1:round(2*k)
        sum_=sum_+abs(((dot(ghat,s(:,r))))^2);
    end
    I(ii,jj,2*k)=(1-sum_);
end
end
end

```

#### E. Signal space test for smooth case.m

```

[u1,s1,v1]=svd(C);
for ii=1:1:251
    ii
        for jj=1:1:251
            xii=(ii-126)/50;

```

```
xjj=(jj-126)/50;
xy_=[xii,xjj];
for trand1=1:1:ntrs
    theta1=2*pi*trand1/ntrs+pi;
    dd=[cos(theta1),sin(theta1)];
    ghat(trand1)=exp(-1i*k*dot(dd,xy_));
end
ss=0;
for j0=round(2*k+1):ntrs
    ss=ss+abs(dot(u1(:,j0),ghat.'));
end
ssave(ii,jj,k-3)=ss;
end
end
end
```

## BIBLIOGRAPHY

- [1] K. Chadan and P. C. Sabatier, *Inverse Problems in Quantum Scattering Theory*,  
Berlin: Springer-Verlag, 1989.
- [2] D. S. Jones, *Acoustic and Electromagnetic Waves*, Oxford: Clarendon Press, 1986.
- [3] P. D. Lax and R. S. Phillips, *Scattering Theory*, New York: Academic Press, 1967.
- [4] R. Leis, *Initial Boundary Value Problems in Mathematical Physics*, New York: John  
Wiley, 1986.
- [5] C. Muller, *Foundations of the Mathematical Theory of Electromagnetic Waves*,  
Berlin Heidelberg New York: Springer-Verlag, 1969.
- [6] R. G. Newton, *Scattering Theory of Waves and Particles*, Berlin Heidelberg New  
York: Springer-Verlag, 1982.
- [7] M. Reed, *Scattering Theory*, New York: Academic Press, 1979.
- [8] C. H. Wilcox, *Scattering Theory for the d'Alembert Equation in Exterior Domains*,  
Berlin Heidelberg New York: Springer-Verlag Lecture Notes in  
Mathematics 442, 1975.
- [9] D. Colton and R. Kress, *Inverse Acoustic and Electromagnetic Scattering Theory*,  
Berlin: Springer, 1998.

- [10] G. Bao, S. Hou and P. Li, "Imaging scattering by a continuation method with initial guesses from a direct imaging algorithm," *Journal of computational physics*, vol. 227, no. 1, pp. 755-762, 2007.
- [11] G. Bao and P. Li, "Inverse medium scattering for three-dimensional time harmonic Maxwell equations," *Inverse Problem*, no. 20, pp. L1-L7, 2004.
- [12] G. Bao and P. Li, "Inverse medium scattering problems for electromagnetic waves," *J. Appl. Math*, no. 65, pp. 2049-1066, 2005.
- [13] G. Bao and P. Li, "Inverse medium scattering for the Helmholtz equation at fixed frequency," *Inverse Problems*, no. 21, pp. 1621-1641, 2005.
- [14] G. Bao and P. Li, "Numerical solution of inverse scattering for near-field optics," *Optics Lett*, vol. 32, no. 11, pp. 1465-1467, 2007.
- [15] Y. Chen, "Inverse scattering via Heisenberg uncertainty principle," *Inverse Problems*, no. 13, pp. 253-282, 1997.
- [16] Y. Chen, "Inverse scattering via skin effect," *Inverse Problems*, no. 13, pp. 649-677, 1997.
- [17] S. Hou, K. Solna and H. Zhao, "Imaging of location and geometry for extended targets using the response matrix," *J. Comp. Phys*, vol. 199, no. 1, pp. 317-338, 2004.
- [18] D. Colton, J. Colye and P. Monk, "Recent developments in inverse acoustic scattering theory," *SIREV*, no. 42, pp. 369-414, 2000.
- [19] S. Hou, K. Solna and H. Zhao, "A direct imaging algorithm for extended targets," *Inverse Problems*, no. 22, pp. 1151-1178, 2006.

- [20] S. Hou, K. Solna and H. Zhao, "A direct imaging method for far field data," *Inverse Problems*, no. 23, pp. 1533-1546, 2007.
- [21] S. Hou, K. Huang, K. Solna and H. Zhao, "A Phase and Space Coherent Direct Imaging Algorithm," *J. Acoust. Soc. Am.*, no. 125, pp. 227-238, 2009.
- [22] X. Chen, "Application of signal-subspace and optimization methods in reconstructing extended scatterers," *Journal of the Optical Society of America*, vol. 26, pp. 1022-6, 2009.
- [23] A. J. Devaney, "Super-resolution processing of multi-static data using time-reversal and music," *J. Acoust. Soc. Am.*.
- [24] R. O. Schmidt, "Multiple emitter location and signal parameter estimation," *IEEE Trans. Antennas Propagation*, vol. 34, no. 3, pp. 276-280, 1986.
- [25] F. K. Gruber, E. A. Marengo and A. J. Devaney, "Time-reversal imaging with multiple signal classification considering multiple scattering between the targets," *J. Acoust. Soc. Am.*, no. 115, pp. 3042-3047, 2004.
- [26] E. Kerbrat, C. Prada and M. Fink, "Imaging in the presence of grain noise using the decomposition of the time reversal operator," *J. Acoust. Soc. Am.*, no. 113, pp. 1230-1240, 2003.
- [27] C. Prada and J. L. Thomas, "Experimental subwavelength localization of scatterers by decomposition of the time reversal operator interpreted as a covariance matrix," *J. Acoust. Soc. Am.*, no. 114, pp. 235-243, 2003.
- [28] F. Cakoni and D. Colton, *Qualitative Methods in Inverse Scattering Theory: An introduction*, Berlin: Springer, 2005.

- [29] D. Colton and A. Kirsch, "A simple method for solving inverse scattering problems in the resonance region," *Inverse Problems*, no. 12(4), pp. 383-93, 1996.
- [30] A. Kirsch, "Characterization of the shape of a scattering obstacle using the spectral data of the far field operator," *Inverse Problems*, no. 14(6), pp. 1489-1512, 1998.
- [31] A. Kirsch, "The music algorithm and the factorization method in inverse scattering theory for inhomogeneous media," *Inverse Problems*, vol. 18, pp. 1025-1040, 2002.
- [32] M. Cheney, "The linear sampling method and the music algorithm," *Inverse Problems*, no. 17, pp. 591-595, 2001.
- [33] H. Liu and J. Zou, "On Uniqueness in Inverse Acoustic and Electromagnetic Obstacle Scattering Problems," in *Journal of Physics: Conference Series*, Vol. 124. No. 1. IOP Publishing, 2008.
- [34] T. Chan and L. Vess, "Active contours without edges," *IEEE*, vol. 10, no. 2, 2001.
- [35] A. Anand, J. Owall and C. Turc, "Well-conditioned boundary integral equations for two-dimensional sound-hard scattering problems in domains with corners," *Journal of Integral Equations and Applications*, vol. 24, no. 3, pp. 321-358, 2012.
- [36] S. Ni, P. Wang, M. Paun and W. Dai, "Spotted cDNA microarray image segmentation using ACWE," *Romanian Journal of Information Science and Technology*, vol. 12, pp. 249-263, 2009.

- [37] D. Colton and R. Kress, *Integral equation methods in scattering theory*, New York: Wiley-Interscience Publication, 1983.
- [38] R. Kress, "A Nystrom method for boundary integral equations in domains with corners," *Numer. Math*, no. 58(2), pp. 145-161, 1990.
- [39] M. Costabel, "Boundary integral operators on Lipschitz domains: elementary results," *SIAM J. Math. Anal.*, no. 19(3), pp. 613-626, 1988.
- [40] W. McLean, *Strongly elliptic systems and boundary integral equations*, Cambridge: Cambridge University Press, 2000.
- [41] S. Hou, Y. Jiang and Y. Cheng, "Direct and Inverse Scattering Problems for Domains with Multiple Corners," *International Journal of Partial Differential Equations*, vol. 2015, no. Article ID 968529, 2015.
- [42] M. Holmes and A. a. I. C. Gray, "Fast SVD for large-scale matrices.," *Workshop on Efficient Machine Learning at NIPS*, vol. 58, 2007.
- [43] D. Colton, H. Haddar and P. Monk, "The linear sampling method for solving the electromagnetic inverse scattering problem," *SIAM Journal on Scientific Computing*, no. 24(3), pp. 719-731, 2003.
- [44] D. Colton, M. Piana and R. Potthast, "A simple method using Morozov's discrepancy principle for solving inverse scattering problems," *Inverse Problems*, vol. 13, no. 6, pp. 1477-1493, 1997.
- [45] J. C. Nédélec, *Acoustic and electromagnetic equations*, Springer Science & Business Media, 2001.

- [46] S. Osher and J. A. Sethian, "Fronts propagating with curvature-dependent speed: algorithms based on Hamilton-Jacobi formulations," *Journal of computational physics*, no. 79(1), pp. 12-49, 1988.
- [47] H. K. Zhao, T. Chan, B. Merriman and S. Osher, "A variational level set approach to multiphase motion," *Journal of computational physics*, no. 127(1), pp. 179-195, 1996.
- [48] G. Aubert and L. Vese, "A variational method in image recovery," *SIAM Journal on Numerical Analysis*, no. 34(5), pp. 1948-1979, 1997.
- [49] L. Mirsky, "Symmetric gauge functions and unitarily invariant norms," *The quarterly journal of mathematics*, vol. 11.1, pp. 50-59, 1960.
- [50] J. C. a. R. G. J. S. Gower, "Minimum Spanning Trees and Single Linkage Cluster Analysis," *Journal of the Royal Statistical Society*, vol. 18, no. 1, pp. 54-64, 1969.
- [51] L. Chen and R. a. T. M. Feris, "Efficient partial shape matching using smith-waterman algorithm," in *IEEE Computer Society Conference*, 2008.
- [52] M. Donoser and H. a. B. H. Riemenschneider, "Efficient partial shape matching of outer contours," in *Asian Conference on Computer Vision*, Springer Berlin Heidelberg, 2009.
- [53] Y. Cao, Z. Zhang, I. Czogiel and I. a. W. S. Dryden, "2d nonrigid partial shape matching using memc and contour subdivision.," in *Computer Vision and Pattern Recognition (CVPR)*, 2011.